PFC/RR-85-11

DOE/ET-51013-152
UC-20 f

SOFT X-RAY TOMOGRAPHY ON THE ALCATOR C TOKAMAK

JOSEPH FRANK CAMACHO

Plasma Fusion Center
Massachusetts Institute of Technology
Cambridge, MA 02139

JUNE 1985

This work was supported by the U.S. Department of Energy Contract No. DE-AC02-78ET51013. Reproduction, translation, publication, use and disposal, in whole or in part by or for the United States government is permitted.

SOFT X-RAY TOMOGRAPHY ON THE ALCATOR C TOKAMAK

by

JOSEPH FRANK CAMACHO
S.B., Massachusetts Institute of Technology, 1982

Submitted to the
Department of Electrical Engineering and Computer Science
in Partial Fulfillment of the Requirements
for the Degree of

MASTER OF SCIENCE

at the

MASSACHUSETTS INSTITUTE OF TECHNOLOGY

May 1985

Signature of Author J. Frank Camacho
Department of Electrical Engineering
and Computer Science
May 1985

Certified by Ronald R Parker
Professor Ronald R. Parker
Thesis Supervisor

Accepted by
Professor Arthur C. Smith
Chairman, Departmental Committee
on Graduate Students

SOFT X-RAY TOMOGRAPHY ON THE ALCATOR C TOKAMAK

by

JOSEPH FRANK CAMACHO

Submitted to the Department of Electrical Engineering and Computer Science
in May 1985 in Partial Fulfillment of the Requirements
for the Degree of Master of Science

ABSTRACT

A soft x-ray tomography experiment has been performed on the Alcator C tokamak. An 80-chord array of detectors consisting of miniature PIN photodiodes was used to obtain tomographic reconstructions of the soft x-ray emissivity function's poloidal cross-section. The detectors are located around the periphery of the plasma at one toroidal location (top and bottom ports) and are capable of yielding useful information over a wide range of plasma operating parameters and conditions. The reconstruction algorithm employed makes no assumptions whatsoever about plasma rotation, position, or symmetry. Its performance was tested, and it was found to work well and to be fairly insensitive to estimated levels of random and systematic errors in the data.

The reconstructions of the soft x-ray emissivity can be used to study plasma position and shape under equilibrium conditions (*i.e.*, Shafranov shift and non-circularity), MHD phenomena (*e.g.*, disruptions and sawtooth oscillations), impurity effects, and several other aspects of plasma behavior. Of particular interest is the MHD activity which takes place in pellet-fueled discharges. Under these conditions, the reconstructions appear to indicate the presence of the $m = 1$ magnetic island structure associated with sawtooth oscillations. The behavior of the emissivity enhancement factor in this type of discharge is also presented. In addition to this rotating instability which accompanies sawtooth oscillations, the occurrence of an unexplained instability not associated with sawteeth and not exhibiting rotation is observed in other pellet-fueled plasmas.

A study was done of what further information could be obtained by installing an additional array of detectors on a side port in order to have more views of the plasma. Recommendations for future work along these lines are given.

Thesis Supervisor: Dr. Ronald R. Parker

Titles: Professor of Electrical Engineering
Associate Director, MIT Plasma Fusion Center

TABLE OF CONTENTS

LIST OF FIGURES

LIST OF TABLES

ACKNOWLEDGEMENTS

This thesis was prepared at the MIT Plasma Fusion Center and the Francis Bitter National Magnet Laboratory, and was sponsored by the Department of Energy of the United States Government under contract number DE-AC02-78ET51013. I am grateful to the Department of Energy for providing financial and technical support.

The individuals of the Alcator Group comprise a very talented and hard-working team of scientists, graduate students, and technical support personnel. The Group's enterprise is very much a concerted effort, and many of its people have assisted me, at one point or another, during my work on this thesis. A few of those who have made notable contributions to it are acknowledged below.

I thank Professor Ronald R. Parker, leader of the Alcator Group, for suggesting the topic of this thesis and for supervising it, for providing me with financial and academic support during my time as a master's degree student, and for originally granting me the opportunity to begin work with the Alcator Group as an undergraduate student in the summer of 1980.

Special thanks are extended to Dr. Robert S. Granetz, who originally conceived of the idea for the experiment described in this thesis, did much of the theoretical and developmental work leading up to it, and collaborated closely with me during the entire course of this project. His guidance and assistance (especially in the area of computer programming and data acquisition), patience, good humor, and dedication are gratefully appreciated. I found working with him to be an enjoyable experience which has enhanced my graduate education considerably.

Mr. George Chihoski was very helpful in much of the vacuum hardward design and assembly. He made many important suggestions; I thank him for the time he invested in this work and for graciously sharing his expertise in mechanical design. I also thank Mr. William Nispel, of the MIT Laboratory for Nuclear Science machine shop, and his supervisor, Mr. Mario Aloisi. Mr. Nispel did all of the machining for this project; this work at times required a high degree of skill, and it was of very

high quality and almost always done promptly despite the difficulty and quantity involved.

I thank the members of the Alcator vacuum shop for their work in assembling the vacuum hardware and installing it on the tokamak; in particular, I acknowledge the work of Mr. Harold Shriber, who attempted to find the best way to seal the experiment's beryllium windows in a high vacuum, and that of Mr. John Heckman, who did much of the welding required and some of the leak-testing of the equipment. Mr. Edward Thibeault, of the Alcator machine shop, also did some of the welding work, and there was some electron beam welding work done by the Applied Energy Company of Stoneham, Massachusetts, operated by Mr. John Mengus. Most of these welding jobs were critically important to the success of the experiment, as a leak into the Alcator vacuum system would have prevented it from being conducted at all. The good work done in this respect is thankfully appreciated.

Mr. Thomas D. Shepard, a fellow graduate student, was most helpful in taking the photographs which appear in Fig. 9 and Fig. 10 of this thesis.

I thank Dr. Richard Petrasso for his interest in this project and especially for providing me with the results of computer calculations which greatly helped in the analysis of the soft x-ray emissivity enhancement factor presented in Sec. IV.3. Dr. Steven Wolfe also contributed to this portion of the work by supplying the required density profile information; Dr. Steven McCool and Mr. Camilo Gomez, a fellow graduate student, also helped by providing the temperature profile information needed for the analysis.

The technical support personnel of the Alcator operations crew (especially Mr. Frank Silva) deserve much credit for their dedicated daily efforts in reliably operating the tokamak and setting up the plasma discharges which provided the data for this experiment. I also thank Dr. Martin Greenwald and Mr. Jeffrey Parker, a fellow graduate student, for operating the pellet injector, which created the plasma conditions yielding the most interesting data of this study.

Chapter I

INTRODUCTION

I.1 Thermonuclear Fusion and Alcator

The effort to achieve controlled thermonuclear fusion has been an ongoing one in the study of plasma physics since the 1950's. The ultimate objective of this endeavor is to demonstrate the technical feasibility of utilizing the tremendous energy released by the nuclear fusion reaction to produce large-scale, commercially usable electrical power.

Thermonuclear fusion (or *nuclear fusion*) refers to the following process: The atoms in a gas are somehow fully ionized, thereby creating a *plasma*, or gas-like state of charged particles. The positively charged nuclei undergo binary collisions, and if they are given enough energy to overcome the Coulomb electrostatic repulsion force, they will join after colliding to form heavier nuclei. In this reaction some mass is converted into energy; this process is how the sun and other stars produce their heat, as they are comprised of gases under intense gravitational pressure. Because the fuel most likely to be used for nuclear fusion consists of isotopes of hydrogen (deuterium and tritium), which are readily extracted from water or artificially created, the fuel supply would be abundant and not subject to the control and monopolizing influence of a particular nation or bloc of nations. Furthermore, any fusion reactor would be inherently safer than a present-day nuclear fission reactor, as there is no possibility of a catastrophic event such as a "meltdown." It is anticipated that the problems associated with the nuclear radiation released by fusion would also be more manageable than those associated with the radiation emitted by fission, such as nuclear waste and the release of radioactive materials. Because of these advantages, controlled thermonuclear fusion holds much promise for becoming one ultimate long range solution to current energy problems of our society.

However, before this goal is achieved, much work remains to be done to demonstrate that fusion is technically and economically feasible. Plasma physics is a

complex subject, because the system of charged particles reacting to external and self-generated electromagnetic fields can be very tenuous and unstable, and it is difficult to describe with useful equations. Therefore, the behavior of a plasma is often hard to predict. Furthermore, one needs to develop the mechanisms by which the energy liberated in the fusion reactions can be converted to some useful form of heat which can then be used, for example, to make steam and drive a turbine. It is generally thought that it will be many years (perhaps several decades) before a fusion reactor capable of generating usable electrical power is constructed and operated successfully. Various experiments and studies are being conducted at laboratories and universities around the world to obtain a better understanding of the physics of fusion plasmas and to develop the engineering technologies that will be needed to implement a fusion reactor.

At the Massachusetts Institute of Technology, the Alcator ("**Alto Campo Torus**," or high field torus) program is one such experiment. The approach being taken in this project is that of magnetic confinement. An intense, pulsed magnetic field and an electric current driven through the plasma are used to confine the charged particles; the plasma is heated resistively (*ohmic heating*) by the current which passes through it in a toroidal (doughnut shaped) device which is generically known as a *tokamak* (from the Russian acronym for this kind of machine; the concept for it was originally developed by physicists in the USSR[1]). Fig. 1 shows the geometry of a tokamak device; Fig. 2 is an artist's rendition of the Alcator C tokamak, and Table 1 lists the main operating parameters of Alcator C.

In order for fusion to become viable as a source of energy (from a physics point of view), there are basically two parameters which must attain sufficiently large values in the presently envisioned reactors. The first of these is the plasma temperature T; for the deuterium-tritium reaction, which appears to be the first fusion reaction that will be attempted for a reactor, enormous temperatures ($T \sim 10^8$ °K, or about 10,000 electron volts in the units commonly used in plasma physics) are required.[2] These high temperatures make the cross-section for the reaction appreciable, so that enough fusion events take place to release a considerable amount of

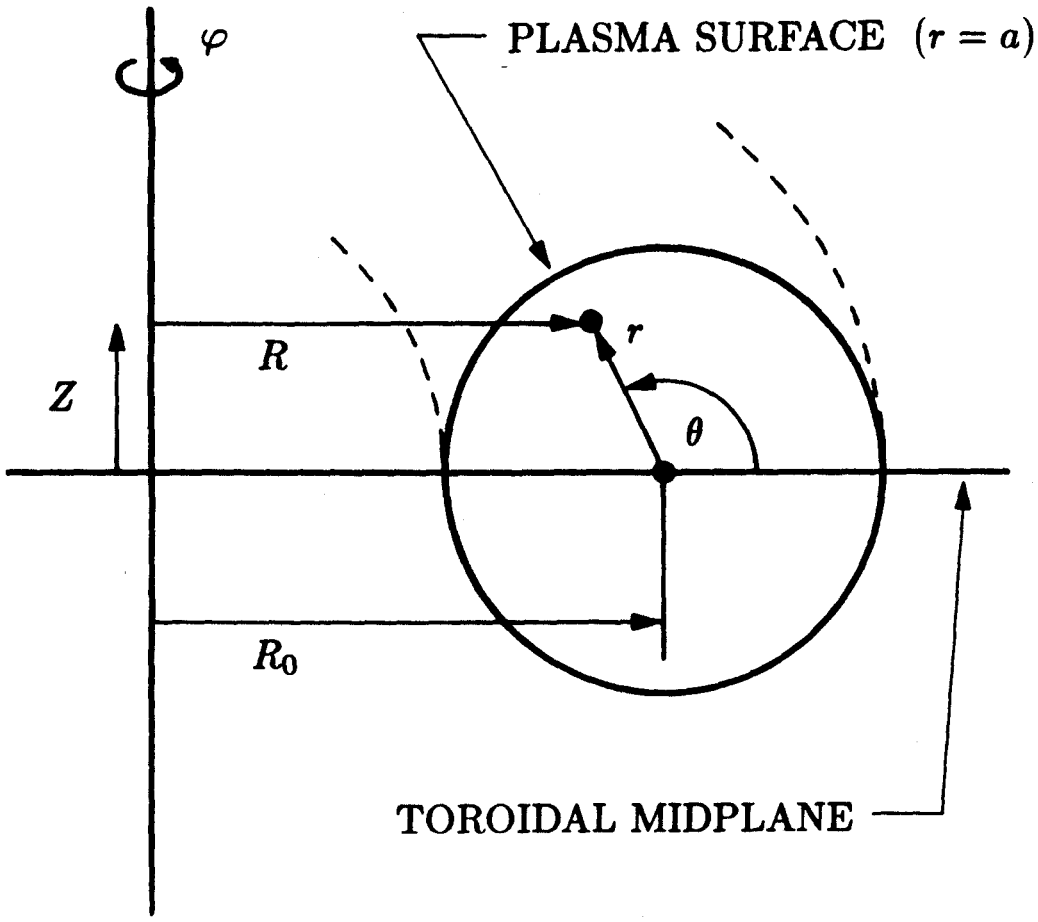

Figure 1 — The geometry of a tokamak device. The plasma is confined in the shape of a torus by magnetic fields. The (r,θ) plane (the cross-section of the torus) is the *poloidal plane*. The coordinate r is the *minor radius*, R is the *major radius*, θ is the *poloidal angle*, φ is the *toroidal angle*, and the Z-axis is along the vertical centerline. On Alcator C, a = 16.5 cm and R_0 = 64 cm.

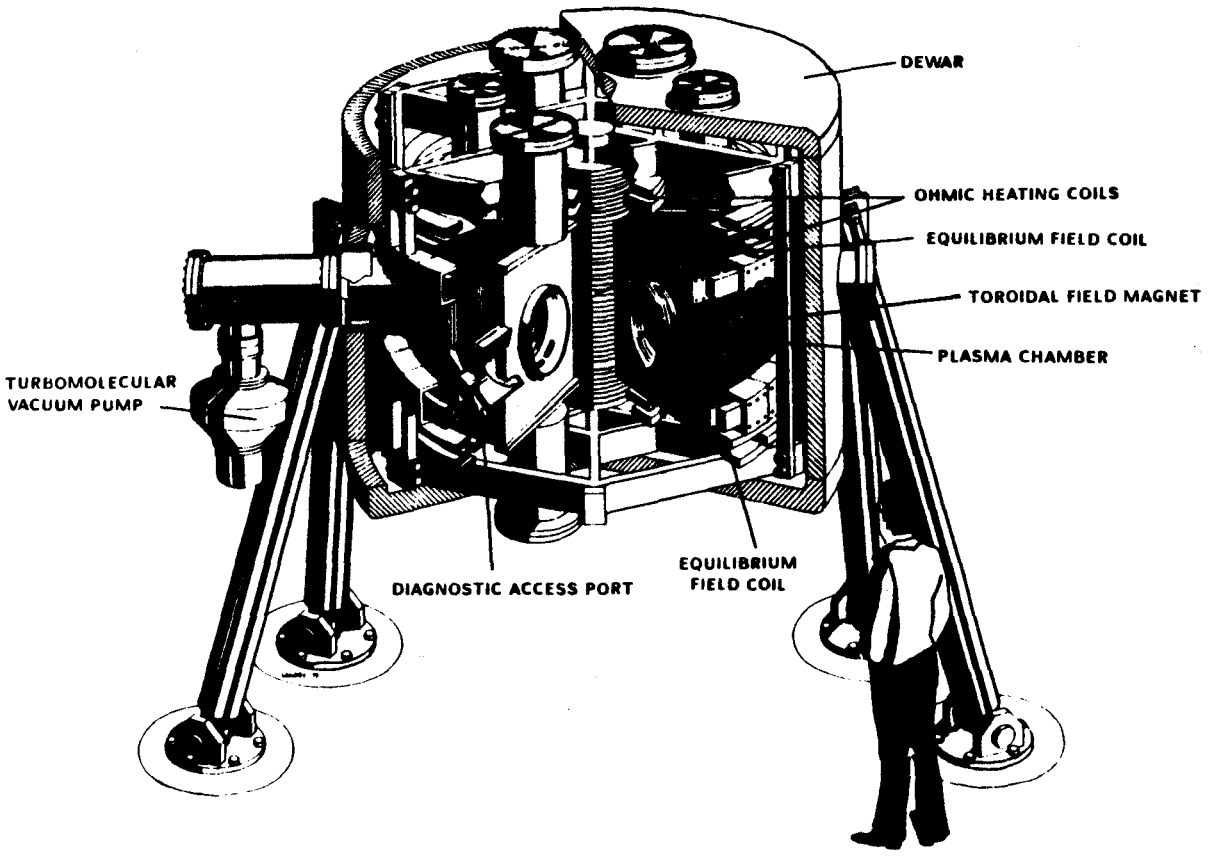

Figure 2 — The Alcator C tokamak (cut-away view).

energy. The other necessary condition is that the product of the plasma particle density, n, and the energy confinement time, τ_E, must exceed a certain critical value at which the power released by the fusion reactions equals that which is expended to confine the plasma and heat it so that enough fusion reactions take place (this is the so-called "breakeven point"). This parameter is known as the ***Lawson criterion***, and it is $n\tau_E \approx 6 \times 10^{13}$ cm^{-3}-s for a deuterium-tritium reaction.[3] With the use of a hydrogen pellet injector, Alcator C has had densities and confinement times large enough to reach $n\tau_E \approx 6\text{–}8 \times 10^{13}$ cm^{-3}-s, thereby meeting or exceeding the Lawson criterion.[4]

Table 1

Alcator C Parameters

Major Radius	$R_0 = 64$ cm
Minor Radius	$a = 16.5$ cm
Toroidal Magnetic Field	$B_\varphi \leq 12$ T
Plasma Current	$I_p \leq 800$ kA
Plasma Density	$n \leq 2 \times 10^{15}$ cm^{-3}
Electron Temperature	$T_e \leq 3$ keV
Ion Temperature	$T_i \leq 1.5$ keV
Energy Confinement Time	$\tau_E \leq 50$ ms
Lawson Product	$n\tau_E \leq 6\text{–}8 \times 10^{13}$ cm^{-3}-s
Ohmic Heating Input Power	$P_{OH} \leq 1.5$ MW
Duration of Plasma Discharge	$\tau_{plasma} = 300\text{–}600$ ms

I.2 Motivation for and Objectives of a Tomography Experiment

The very nature of plasmas (especially fusion plasmas) often makes the measurement of their basic parameters and properties quite a challenge to the researcher, who must devote a considerable amount of time and energy to the task of accumulating experimental observations and developing the techniques and equipment for collecting data. Plasma physics provides a wealth of phenomena to be studied, and the need to further the understanding of still poorly explained results which have a direct bearing on fusion's propects for success has motivated a tremendous amount of work in the area of diagnostics for magnetically confined plasmas.[5]

Measuring the intensity of soft x-ray emission from plasmas has been an important means of studying and understanding various plasma characteristics. One of the first uses of a soft x-ray emission diagnostic on a tokamak took place on the ST device at the Princeton Plasma Physics Laboratory, in which internal disruptions (the so-called "sawtooth" oscillation) and $m = 1$ magnetohydrodynamic (MHD) oscillations were observed using silicon surface-barrier diodes.[6] Subsequent work on other machines has led to this becoming a standard tokamak diagnostic[7] which can be used for various purposes, as has been done on the Alcator machines at MIT.[8,9]

Soft x-ray emission from tokamak plasmas arises from a variety of sources. This radiation is dependent on various plasma parameters, such as density and temperature, and one can thus infer information about them by observing the soft x-ray emission. This information can then be analyzed and related to properties such as plasma position, shape, impurity distribution, and MHD instability phenomena. It is therefore desirable to have as much knowledge of the soft x-ray *emissivity* (power emitted per unit volume of plasma) as possible. One way to acquire this information is by measuring the emission in a poloidal cross-section of the tokamak plasma. If these measurements are suitably performed, one can reconstruct the two-dimensional soft x-ray emissivity function in the given cross-section. This task can be accomplished with the use of *tomography*, which is a non-invasive imaging method in which multiple views of an object's x-ray emission or absorption along

chords through a cross-section are taken. If a sufficiently large and properly arranged number of views is available, the object's spatial emission or absorption distribution can be recovered. Various techniques and mathematical algorithms for reconstruction tomography have been developed; in particular, absorption tomography has found widespread use in medicine, in which Computer Assisted Tomography devices (CAT scanners) measure how much of an x-ray source's energy is transmitted through a certain portion of a patient's anatomy in order to obtain reconstructed images of the patient's internal structure.[10]

In plasma physics, several researchers[11-16] have attempted to use the principles of tomography to gain information about the soft x-ray emissivity. It has been suggested[17] that an x-ray tomography diagnostic would be helpful in the study of, among other things, MHD activity in Alcator C and how such activity might be related to various other aspects of plasma behavior (e.g., disruptions and density thresholds for MHD activity). Subsequent investigation[18] demonstrated that such a diagnostic would be feasible on Alcator C.

The purpose of this thesis, therefore, was to design, build, and implement such a diagnostic and to analyze the data collected from it. This thesis report is organized as follows: Chapter II presents some of the important theoretical aspects of the problem, such as the nature and source of soft x-rays in a tokamak plasma and the various mathematical methods which can be used to perform tomographic reconstructions. Chapter III describes the details of the experimental apparatus, and in Chapter IV the most interesting experimental results obtained in this study are presented. These include computer simulations which test the performance of the tomography algorithm used, reconstructions of an emissivity under equilibrium conditions, and data from discharges that involved pellet injection, which triggered large-scale MHD behavior. Finally, a conclusion summarizing the work conducted and suggesting possible future research is given. This chapter includes a section with the results of a brief study done to determined how much more information could be obtained from an expanded array of detectors on Alcator C.

Chapter II

THEORETICAL ASPECTS OF THE EXPERIMENT

II.1 Soft X-Ray Radiation from a Plasma

The topic of radiation processes from a plasma can be quite complex due to the rich variety of phenomena which can occur when one has a collection of ionized particles immersed in applied and self-generated electromagnetic fields and undergoing various kinds of accelerations and excitations. Most of the radiated power from a typical Alcator C plasma is in the ultraviolet and "soft" (*i.e.*, low energy) x-ray portion of the electromagnetic spectrum; given the physical constraints involved and the purposes of this thesis as detailed in the previous chapter, the focus here is on those radiation mechanisms which give rise to emission in the soft x-ray region of the spectrum (roughly about 0.2 to 20 keV, or 0.6 to 60 Å). After having described the nature of these mechanisms, the information which one can obtain from this radiation will be discussed.

II.1.1 *Mechanisms of Interest*

There are three processes which contribute to the soft x-ray emission from an Alcator C plasma: continuous radiation from unbound accelerated charges, continuous radiation from free electrons which are then captured by ions and go into a bound state, and discrete radiation from bound state electronic transitions within atoms which are not fully ionized. These are referred to as *bremsstrahlung* radiation, *recombination* radiation, and *excitation* (or *line*) radiation, respectively. All of these forms of radiation can be very helpful in diagnosing a plasma.

Consider first the contribution due to bremsstrahlung. Suppose one has a plasma composed of an arbitrary mixture of atomic species which are all completely ionized, and that recombination radiation can be neglected. The radiation losses will then be due to bremsstrahlung as a result of the deflection of charged particles by the Coulomb electrostatic fields of the other charged particles. Unless the temperature

of the plasma is very high ($T > 50$ keV, at which point relativistic effects need to be taken into account), almost all such radiation arises from electron-ion interactions. The positively charged nucleus remains relatively stationary (due to its much larger mass, it will not be significantly accelerated by electrons), and the electron passes by it and is accelerated by the field of the ion. Because the electron is unbound before and after such an encounter with an ion, these transitions are often described as "free-free."

Quantum mechanics must be used in order to compute rigorously the electron-ion bremsstrahlung. However, from the classical expression for the rate at which energy is radiated by an accelerated point charge, it is possible to obtain an expression for the power emitted which is of the correct functional form but differs only by a numerical multiplicative factor from the result obtained in the more accurate but much more complicated quantum mechanical calculation. This numerical factor is on the order of unity. For present purposes, therefore, it will suffice to use the classical model.

If one considers a single point particle of charge q, whose velocity is such that $v/c \ll 1$, and it undergoes an acceleration of magnitude a, then the power radiated by it is given by[19] (in MKS units)

$$P = \frac{1}{4\pi\epsilon_0}\frac{2q^2a^2}{3c^3}. \tag{1}$$

In the plasma, let there be an electron moving past an ion of charge Z_ie (Z_i is the atomic number of the ion and e is the charge of a proton) at some speed v and impact parameter b. The ion is assumed to be infinitely massive. From the Coulomb force between the two charges, the magnitude of the electron's acceleration is

$$a \approx \frac{Z_ie^2}{4\pi\epsilon_0 m_e b^2}. \tag{2}$$

Substituting this expression into Eqn. 1 gives

$$P \approx \frac{1}{(4\pi\epsilon_0)^3}\frac{2Z_i^2e^6}{3m_e^2c^3b^4}. \tag{3}$$

The total bremsstrahlung power density radiated by the electrons colliding with ions of the given species at all impact parameters is then given by[20]

$$P_b = \frac{1}{(4\pi\epsilon_0)^3}\frac{2e^6 n_e n_i Z_i^2}{3m_e^2 c^3}\int_{b_{min}}^{b_{max}}\frac{db}{b^4}(2\pi b)\frac{2b}{v} \tag{4}$$

where n_e and n_i are the electron and ion particle densities, respectively.

There is virtually no interaction between ions and electrons at distances beyond the Debye length, so that distance should be the value of b_{max}. In order to facilitate the evaulation of the integral, however, one can let $b_{max} \rightarrow \infty$ without introducing a significant numerical error. However, one cannot let $b_{min} \rightarrow 0$, as the integral diverges in this limit; b_{min}, the distance of closest approach between the electrons and ions, can be obtained from the Heisenberg Uncertainty Principle, $\Delta x \Delta p \geq \hbar/2$. Setting $\Delta p = m_e v$ and $\Delta x = b_{min}$, and using the estimate $\Delta x \Delta p \approx \hbar$, yields

$$b_{min} \approx \frac{\hbar}{m_e v}. \tag{5}$$

If the electron velocity distribution is Maxwellian, then

$$\tfrac{1}{2}m_e v_{te}^2 = \tfrac{3}{2}T_e \tag{6}$$

where T_e is the kinetic temperature of the electrons (in units of energy), and $v_{te}^2 \equiv \overline{v^2}$ is the square of the thermal speed of the electrons (the average of v^2 over the distribution). Substituting v_{te} for v in Eqn. 5 gives

$$b_{min} \approx \frac{\hbar}{3m_e T_e^{1/2}} \tag{7}$$

so that upon evaluating the integral in Eqn. 4 one obtains

$$P_b \approx \frac{8\pi e^6 n_e n_i Z_i^2 T_e^{1/2}}{\sqrt{3}\,(4\pi\epsilon_0)^3\, m_e^{3/2} c^3 \hbar}. \tag{8}$$

For a mixture of ion species, the quantity $n_i Z_i^2$ should be replaced by $\sum_s n_s Z_s^2$, where $\sum_s$ denotes a sum over all species. Defining

$$Z_{eff} \equiv \frac{\sum_s n_s Z_s^2}{n_e} \tag{9}$$

as the effective atomic number of the plasma, one obtains

$$P_b \approx \frac{8\pi e^6 n_e^2 Z_{eff} T_e^{1/2}}{\sqrt{3}\,(4\pi\epsilon_0)^3\, m_e^{3/2} c^3 \hbar}\,. \tag{10}$$

The more precise quantum mechanical treatment yields[20]

$$P_b = g_{ff} \frac{32\pi\sqrt{2\pi}\, e^6 n_e^2 Z_{eff} T_e^{1/2}}{3\sqrt{3}\,(4\pi\epsilon_0)^3\, m_e^{3/2} c^3 h} \tag{11}$$

where g_{ff} is the so-called free-free Gaunt factor which describes the quantum mechanical correction. At high temperatures, $g_{ff} \to 2\sqrt{3}/\pi$; upon substituting in all the numerical values for the physical constants and converting the units of n_e from m^{-3} to cm^{-3} and T_e from joules to keV, one has

$$P_b \approx (5.33 \times 10^{-31}) Z_{eff}\, n_e^2\, T_e^{1/2} \quad \text{watts-cm}^{-3}\,. \tag{12}$$

This is the bremsstrahlung power radiated per unit volume from the plasma. The preceding derivation gave the bremsstrahlung emission over all frequencies. In order to obtain the spectral distribution of this emitted power, one needs the classical expression for the rate of bremsstrahlung emission per unit volume per unit frequency in the frequency range from ν to $\nu + d\nu$. This is given by a Boltzmann energy distribution, and is[20]

$$dP_\nu = g_{ff} \frac{32\pi\sqrt{2\pi}\, e^6 n_e^2 Z_{eff}}{3\sqrt{3}\,(4\pi\epsilon_0)^3\, m_e^{3/2} c^3}\, T_e^{-1/2} \exp\left(-h\nu/T_e\right) d\nu\,. \tag{13}$$

Upon integrating Eqn. 13 over all frequencies, one recovers the expression in Eqn. 11. By using the relationship $c = \lambda\nu$, one can also obtain the rate of energy emission per unit volume per unit wavelength in the interval from λ to $\lambda + d\lambda$:

$$\begin{aligned} dP_\lambda &= g_{ff} \frac{32\pi\sqrt{2\pi}\, e^6 n_e^2 Z_{eff}}{3\sqrt{3}\,(4\pi\epsilon_0)^3\, m_e^{3/2} c^2}\, T_e^{-1/2}\, \lambda^{-2} \exp\left(-hc/\lambda T_e\right) d\lambda \\ &= (6.01 \times 10^{-30}) g_{ff}\, Z_{eff}\, n_e^2\, T_e^{-1/2}\, \lambda^{-2} \exp\left(-12.4/\lambda T_e\right) d\lambda \quad \text{watts-cm}^{-3} \end{aligned} \tag{14}$$

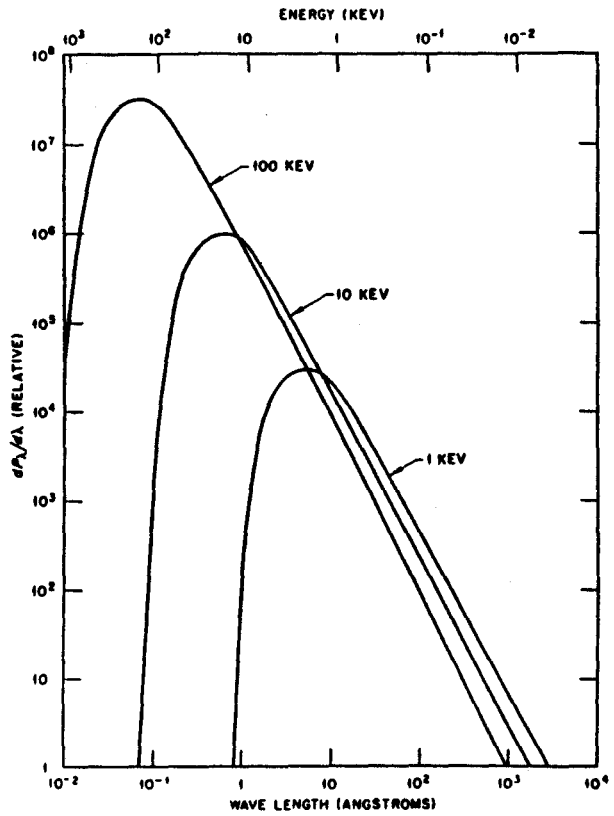

Figure 3 — Bremsstrahlung power spectral distribution at kinetic temperatures of 1, 10, and 100 keV (from Ref. 20). The maximum occurs at $\lambda = 6.2/T_e$ Å. To the left of the maximum the emission is dominated by the exponential term and decreases rapidly with decreasing wavelength. To the right of the maximum the dependence goes as λ^{-2}, so the emission falls off more slowly with increasing wavelength.

where T_e is in keV and λ is in angstroms. A graph of this power distribution at three different values of T_e is shown in Fig. 3.

Fig. 3 shows that at the temperatures of interest in Alcator C ($T_e \sim 1$ keV), a considerable portion of the emitted power lies in the soft x-ray region of the energy spectrum (about 0.2 to 20 keV), so that it is indeed an energy range worth observing.

For a purely hydrogenic plasma ($Z_{eff} = 1$), one finds that there is some amount of recombination radiation because of the distribution of energies involved. In this

mechanism, the free proton of the hydrogen nucleus captures a free electron, resulting in the emission of radiation due to the electron's transition to lower energy level and the formation of a neutral hydrogen atom. However, it can be shown that, except at low temperatures, the contribution from it is negligibly small compared to that of hydrogenic bremsstrahlung.[21] Furthermore, one need not consider the contribution from excitation radiation, because the ionization potential of hydrogen is only 13.6 eV, and hence this radiation does not fall into the soft x-ray portion of the spectrum (it is in the visible and ultraviolet).

One therefore needs to examine the role of non-hydrogenic impurity species in the plasma. As can be seen in Eqn. 8, the Z_i^2 dependence of P_b can cause significant radiated energy losses from the plasma which can lead to a premature termination of the discharge. It is thus very important to maintain the concentration of impurities to a minimum. Moreover, at typical Alcator C temperatures, one finds that species with sufficiently high atomic number are not fully ionized and therefore undergo free-bound or bound-bound transitions which can contribute significantly to the energy loss. The presence of such impurities leads to recombination and excitation radiation.

These two mechanisms are more difficult to describe analytically than bremsstrahlung, and for the purposes of this thesis it will suffice to describe them in a more qualitative way. In recombination radiation, a partially ionized atom captures a free electron; this transition from a free to bound state is what causes the emission of a photon. The contribution to recombination radiation from higher Z_i impurities (such as silicon, for example) can be comparable or considerably larger, in fact, than the contribution that they make to the bremsstrahlung radiation.[21] The presence of impurity atoms may thus add substantially to and even dominate the emission due to hydrogenic bremsstrahlung. This emission also depends on temperature and density, which determine the extent to which the impurities are ionized and how likely they are to capture free electrons. It will thus vary according to how the impurities are spatially distributed in the plasma. The spectrum of this emssion is

in the form of a continuum down to the energy level at which the captured electron reaches its final state.

Substantial radiation losses can also occur due to excitation radiation from impurities, most of which originate from the materials comprising the chamber in which the plasma is situated. Excitation radiation comes about when the absorption of energy in an atom causes the formation of an electronically excited state; the excited energy is subsequently emitted when the electron goes to a lower energy level. This radiation has a discrete spectrum (hence the name "line" radiation), with the frequency of the emitted photons being determined by the difference in the energy levels which the electron transits. As with bremsstrahlung and recombination radiation, this mechanism is temperature and density dependent, as those parameters determine the ionization states of the impurities. Again, therefore, line radiation will vary according to the spatial distribution of the impurities.

II.1.2 *Information Contained in the Soft X-Ray Emission*

What interesting plasma characteristics can one relate to the temperature, density, and impurity dependence of the three soft x-ray emission mechanisms outlined above? In general, it is not a trivial problem to determine immediately which specific emission mechanism is responsible for a given feature in the emissivity. Nevertheless, there are some interesting pieces of information which can be inferred from a reconstruction of the emissivity's poloidal cross-section. These data tend to fall into two broad categories: MHD equilibrium and stability, and impurity distribution.

A relationship between MHD equilibrium and stability and the soft x-ray emission can be established if one considers only the contribution from hydrogenic bremsstrahlung radiation and assumes that recombination and line radiation are not significant. In equilibrium, the magnetic field in an axisymmetric toroidal system (e.g., a tokamak) is such that most of the field lines continue indefinitely around the volume of the torus, ergodically covering a set of simply nested toroidal surfaces. These are called *magnetic surfaces* (see Fig. 4). In the elementary MHD

theory of such a system, it can be shown that the sum of the electron and ion kinetic pressures, $p = (n_e T_e + n_i T_i)$, is a ***surface quantity***, meaning that the pressure is constant on a given magnetic surface.[22] The limiting magnetic surface, which approaches a single magnetic line where the pressure is a maximum (for a centrally peaked pressure profile), is called the *magnetic axis*. Magnetic surfaces are also known as *flux surfaces*, as they are surfaces of constant toroidal and poloidal magnetic flux. There are also toroidal magnetic surfaces in which the field lines, rather than being ergodic, close upon themselves after a finite number of transits the long way around the torus. These are known as *rational surfaces*; they are nested in between the ergodically covered magnetic surfaces, in much the same way that the rational numbers are interspersed among the irrational numbers.

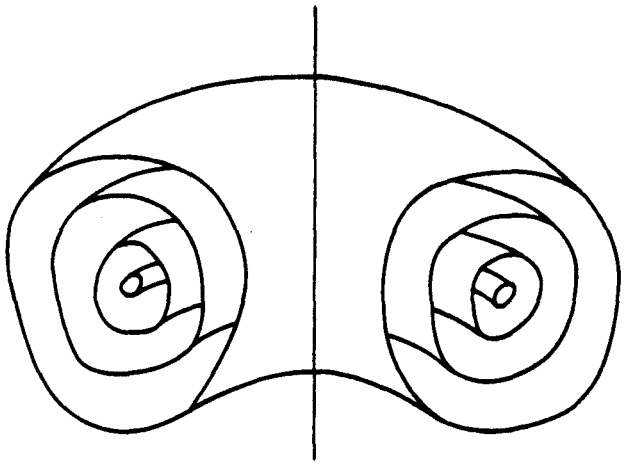

Figure 4 — Magnetic surfaces in a well-confined toroidal equilibrium. These are also the surfaces of constant kinetic pressure (from Ref. 23).

The thermal conductivity parallel to the magnetic field lines is much greater than the conductivity perpendicular to the field lines, even when neoclassical transport effects are taken into account.[23] Thus, temperature equilibrates very rapidly

along the magnetic field in a toroidal geometry (assuming that there are no anomalous heat transport mechanisms). If $n_e \approx n_i$ (as is the case in most plasmas), then $p \approx n_e(T_e + T_i)$, and both T_e and T_i should each be essentially constant on a given toroidal magnetic surface, because the field lines along which the temperature equilibrates are on those surfaces. It thus follows that, if each temperature is constant on a magnetic surface, the density n_e must also be constant on that surface, because pressure is a surface quantity. If $Z_{eff} = 1$ is taken, then all the soft x-ray radiated power density is proportional to $n_e^2 T_e^{1/2}$ (see Eqn. 12), provided one ignores recombination radiation from hydrogen; this assumption is a good one across most of the discharge in an Alcator C plasma, in which the values of T_e are high enough to make hydrogen recombination radiation negligibly small compared to that of bremsstrahlung.[21] Therefore, if n_e and T_e are both constant on a flux surface, the bremsstrahlung power emitted by the particles on that flux surface will also be constant there. Thus, in principle, when $Z_{eff} = 1$, the surfaces of constant soft x-ray emission should be the same nested toroidal surfaces which are associated with the magnetic field topology.

A poloidal cross-section of the emissivity function which displays the contours of constant emissivity should thus also reflect the structure of the surfaces of constant poloidal magnetic flux, and hence reveal information about the nature of the MHD equilibrium of the plasma. It should be noted, however, that it is not possible to associate each value of the observed emissivity with a unique value of the poloidal flux function, ψ. All that can be inferred in this case is that, on a given flux surface, there should be one and only one value of the emissivity. Different values of ψ may yield the same emissvity values, depending on the distribution of density, temperature, and impurities.

The structure of the MHD equilibrium is directly related to features such as plasma position, shape, and motion. For example, in a straight circular cylinder, the magnetic surfaces would all be concentric circles. The effect of bending such a cylinder into a torus is that, to first order, there is a small outward shift of the centers of the circular flux surfaces (known as the *Shafranov shift*).[23] The contours

of constant soft x-ray emissivity should thus show what the Shafranov shift is, which for typical Alcator C parameters should be about one centimeter. The shape of the flux surfaces as revealed by the contours of constant emissivity should also provide information about the degree to which the plasma is non-circular and thus deviates from the analytically predicted equilibrium. If there is any bulk plasma motion, that should lead to motion of the flux surfaces and hence motion of the emissivity contours.

When time-dependent MHD phenomena are investigated, one is led to the study of instabilities. These will lead to some alteration of the magnetic surfaces, and the manner in which the surfaces change or deform is indicative of the nature of the instability. Instabilities can also cause perturbations in density and temperature which thereby perturb the emissivity because it depends strongly on these parameters. Thus, the occurrence of MHD instabilities in the plasma should be reflected in the contours of constant emissivity. Of particular interest in Alcator C are the *resistive tearing modes.* These are non-ideal modes which come about due to the small but finite electrical resistivity of the plasma, which at the temperatures of interest has such a low resistivity that it can usually be taken to be a perfect conductor (the ideal MHD model). The name "tearing mode" comes from the fact that, in order to reduce the total energy of the system, the perturbed currents which arise from the finite resistivity will cause the field lines and flux surfaces to "tear" or "break up" and form *magnetic islands*, which are filaments of plasma with their own set of nested flux surfaces surrounding their own local magnetic axes. This perturbation leads to flux contours which are no longer simply nested toroidal surfaces around a single magnetic axis. Each island twists helically around the torus, following the closed field line that forms its magnetic axis. The whole structure of the island closes upon itself after going the long way around the torus a rational number of times.

A perturbation is called a *resonant mode* if its helicity matches that of the equilibrium field lines at a radius r_s where $q(r_s) = m/n$ (in a tokamak, $q(r) \approx rB_\varphi / R_0 B_\theta$ and is a measure of the helicity of the equilibrium field lines). The indices m and

n are referred to as the *poloidal* and *toroidal mode numbers*, respectively. For given values of m and n, the perturbed current will be exactly paralled to the equilibrium field lines at the resonant radius r_s. When added to the equilibrium fields, the magnetic fields caused by the perturbed currents lead to the formation of magnetic islands centered at the resonant surfaces (see Fig. 5). If energy considerations require that the mode grow in time in order to bring the system to a lower energy state, one has a tearing mode instability.

The effect of magnetic islands on the plasma should be important. For example, it is believed that the $m = 1/n = 1$ resistive kink mode, a special case of a tearing mode, causes the sawtooth oscillations observed in the soft x-rays emitted by tokamak plasmas.[22,24] These are small internal disruptions which are relatively minor in that they do not seem to have a very deleterious effect on global plasma stability and confinement, since they occur around the $q = 1$ surface, which is usually well within the plasma core. However, they can be dangerous if they play a role in a more extensive disruptive instability or become too large.

Higher order instabilities may have more harmful effects on the plasma. Energy transport should increase in the presence of magnetic islands because, as explained above, regions of the plasma connected by magnetic field lines (and hence on the same flux surface) are essentially "shorted together" as far as temperature and density are concerned. In equilibrium, thermal energy flowing radially out of the plasma has to traverse the field lines, and therefore it must proceed on a relatively slow collisional time scale, as opposed to the very rapid thermal equilibration time scale of energy transport parallel to the field lines. However, once magnetic islands are present, energy flow is effectively shunted across the width of the islands, because the inner edge and outer edge of the islands are on the same flux surface. This enhancement of cross-field energy transport should lead to a decrease in the energy confinement time, which is certainly not a desirable effect. If the islands become very large, or if the instability never saturates, the situation can become even worse in terms of global plasma confinement. Even if the islands did saturate at some fixed width after initially growing in size, those existing at different radii could

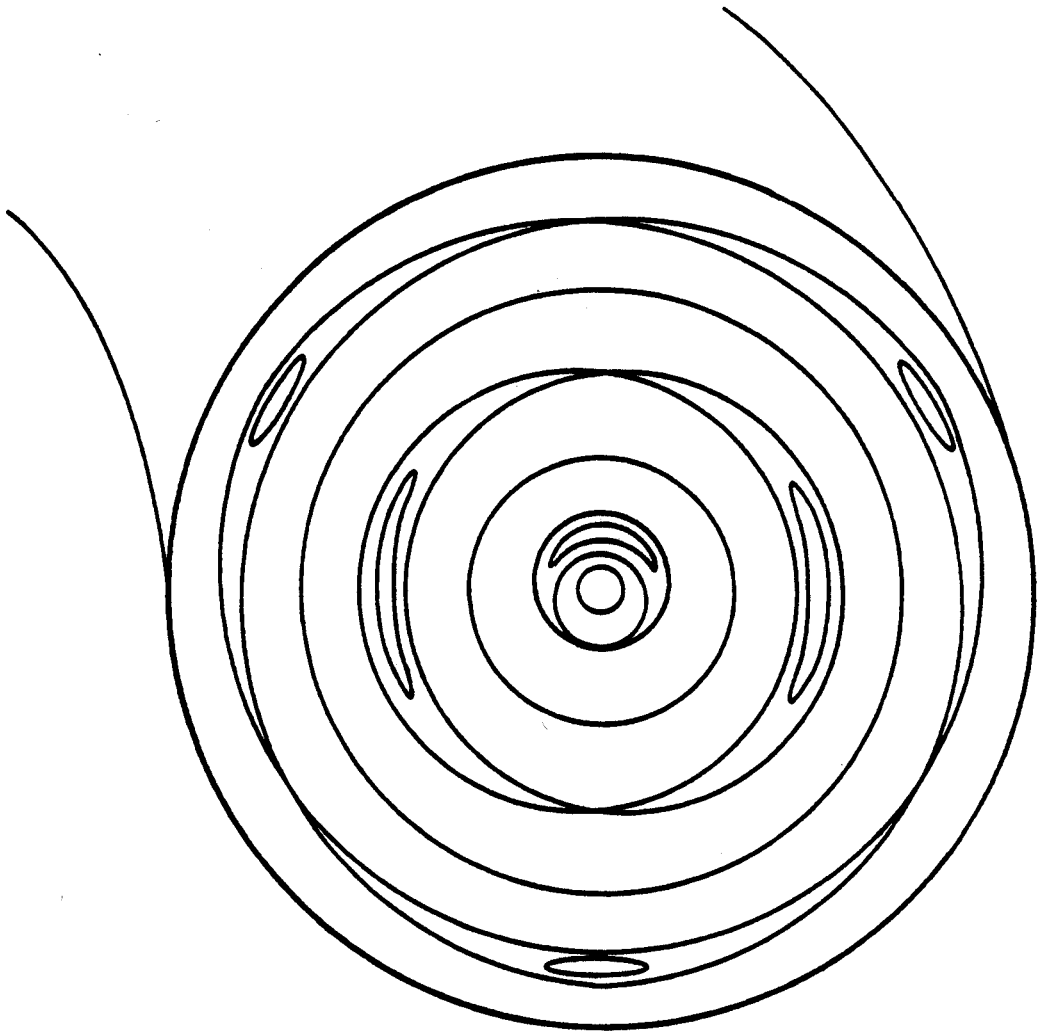

Figure 5 — Flux surface contours in a poloidal cross-section showing $m = 1$, 2, and 3 magnetic islands (from Ref. 17). The islands are brought about by the perturbed currents of the resonant modes which are allowed in the resistive MHD model. These islands also twist around in the toroidal direction; this variation is represented by the toroidal mode number n.

overlap and effectively cover the entire plasma cross-section, leading to a total loss of confinement of the plasma volume. Ideas along these lines have been proposed[25] as mechanisms to explain the so-called major disruption, which is a sudden and violent termination of the plasma discharge brought about by a large scale MHD instability. Knowledge of the soft x-ray emissivity may thus improve one's understanding of these instability phenomena because it can provide a picture of the magnetic surface behavior as a function of time.

Recall that the foregoing discussion has been conducted under the assumption that $Z_{eff} = 1$ and that recombination and line radiation are neglibible relative to bremsstrahlung. If these assumptions are relaxed, then clearly the relationship established above between the soft x-ray emissivity and MHD phenomena will not be as easy to unfold from the data present in a tomographic reconstruction. One can still ignore recombination radiation from hydrogen, as it is only near the edge of the plasma that the temperatures are low enough to make it comparable with bremsstrahlung, and the primary interest is in the hot, central region of the plasma. However, the introduction of even a small concentration of impurities can significantly alter the details of the emissivity.

Impurities in the plasma can emit soft x-rays via bremsstrahlung, recombination, and line radiation. Without some form of energy filtering, it is impossible to distinguish between them, as the detectors used in this experiment respond to total integrated power over the spectrum to which they are sensitive. Impurities in the plasma can radiate copiously under some circumstances, however, so their presence, whether it manifests itself via bremsstrahlung, recombination, or line radiation, can be observed. A tomographic reconstruction of the emissivity would therefore contain information regarding the extent to which impurities are present in the plasma and how they are distributed in the poloidal cross-section.

One way to quantify the degree to which impurities contribute to the overall emissivity is to compare the measured emissivity values with those which one would obtain if all the radiation were due only to hydrogenic bremsstrahlung and recombination, the absolute minimum which a hydrogen plasma would radiate at

a given density and temperature. As explained above, hydrogen recombination radiation can be neglected for the most part because it is only worth considering at low temperatures. The local emissivity values arising from this purely hydrogenic emission can therefore be calculated by using the readily measured density and temperature profiles and substituting them into Eqn. 12. The local ratio of the measured emissivity to the calculated hydrogenic emissivity of the given plasma is know as the *enhancement factor*. It is a measure of the extent to which radiation from impurities contribute to the soft x-ray emission from the plasma.

By examining the spatial variation of the emissivity enhancement factor, one can develop an idea of the impurity distribution across the poloidal cross-section of the plasma. The temporal behavior of the enhancement factor can be of particular interest if it is observed with MHD activity and if one attempts to determine the correlation which might exist between it and instability phenomena. All this information can then perhaps lead one to a greater understanding of the role that impurities play in an Alcator C plasma.

II.2 Tomographic Reconstruction

Various mathematical methods have been developed to perform tomographic reconstructions of objects which emit or absorb x-rays. This section presents an overview of the principles and techniques which can yield a tomographic reconstruction of the cross-section of a radiating object's emissivity (the same ideas apply for absorption tomography). For the purposes of this discussion, the schemes for obtaining reconstructions are grouped into two basic categories: finite element methods and analytic methods. There also exist algorithms which combine both finite element and analytic techniques, such as the Filtered Back-Projection algorithm.[10] They are optimal for a large number of regularly arranged views; such a set-up is not feasible on Alcator C, so these algorithms will not be discussed.

II.2.1 *Finite Element Methods*

Suppose that one has an object with an emitting cross-section which is of arbitrary shape, and that it is divided into N finite elements or *pixels* (from the words "picture elements"). These pixels can be of arbitrary shape and varying size. Situated around the exterior of this planar region, let there be M detectors which measure the power of the radiation incident upon them. The field of view of each detector is determined by the solid angle defined by known apertures and/or collimators. In order for these methods to work accurately, the dimensions of the pixels must be such that the actual emissivity is essentially constant over the area of the pixel. This constraint requires that one take into account the scale lengths of the various plasma parameters which influence the emissivity (in particular, the density and temperature). Furthermore, the radiation from each pixel is assumed to be isotropic.

With these assumptions in mind, one can proceed to calculate how much of the power emitted from each pixel contributes to the total signal on a given detector. The signal S (in watts) on the m^{th} detector can be expressed as a linear combination

of the emissivities $\mathcal{E}$ (in watts-cm^{-3}) of each pixel, with each one being appropriately weighted:

$$S_m = W_{m,1}\mathcal{E}_1 + W_{m,2}\mathcal{E}_2 + \cdots + W_{M,N}\mathcal{E}_N$$

or

$$S_m = \sum_{n=1}^{N} W_{m,n}\mathcal{E}_n \tag{15}$$

where $1 \leq m \leq M$, $1 \leq n \leq N$, M is the number of detectors, and N is the number of pixels, so there are M equations in N unknowns. The coefficients $W_{m,n}$ are the weighting factors which indicate what fraction of the total power radiated from each pixel is actually incident on the given detector. Fig. 6 shows the viewing geometry under consideration. One can see that many of the $W_{m,n}$ coefficients can be zero for a given detector m, because there are pixels which are not in the field of view of the detector. Thus, the power emitted from them is not "seen" by the detector in question.

For a fixed viewing geometry, the weighting coefficients can be pre-calculated and depend only on the parameters of the geometry. This calculation can be done by a simulation in which one assumes a unit emissivity distribution for the pixels and then computes what the signals on each detector should be. Given the known weighting coefficients and the experimentally measured signals, one must then extract the emissivity information contained in Eqn. 15. This problem can be cast into a linear algebra formulation. One can think of $W_{m,n}$ as comprising an $M \times N$ matrix, S_m as comprising a column vector with M elements, and $\mathcal{E}_n$ as comprising a column vector with N elements. Hence,

$$\begin{pmatrix} S_1 \\ S_2 \\ \vdots \\ S_M \end{pmatrix} = \begin{pmatrix} W_{1,1} & W_{1.2} & \cdots & W_{1,N} \\ W_{2,1} & W_{2,2} & \cdots & W_{2,N} \\ \vdots & \vdots & \ddots & \vdots \\ W_{M,1} & W_{M.2} & \cdots & W_{M.N} \end{pmatrix} \begin{pmatrix} \mathcal{E}_1 \\ \mathcal{E}_2 \\ \vdots \\ \mathcal{E}_N \end{pmatrix}$$

or, more compactly,

$$\mathbf{S} = \mathbf{W} \cdot \boldsymbol{\mathcal{E}}\,. \tag{16}$$

This equation must be solved for $\boldsymbol{\mathcal{E}}$, which contains the unknown emissivities.

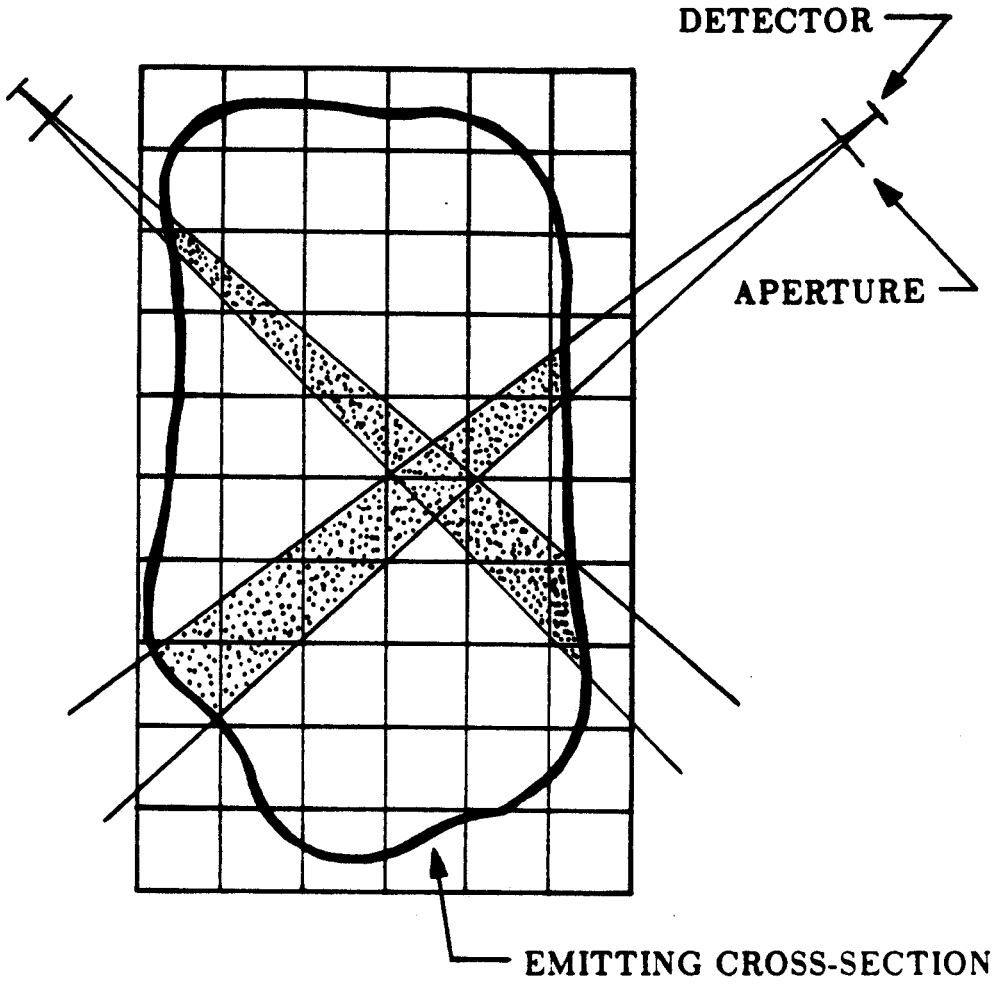

Figure 6 — Pixel viewing geometry. The emitting cross-section can be of arbitrary shape, and the pixels (drawn here as squares) can be of arbitrary shape and varying size. The shaded regions indicate what portion of each pixel is "seen" by each detector.

For the case in which $M = N$ (equal number of detectors and pixels), there is exactly one solution for the pixel emissivities, as $\mathbf{W}$ becomes a square matrix which can be inverted provided that it is not singular. If $M < N$ (fewer detectors that pixels), then the problem is underdetermined and there are an infinite number of solutions. One can impose constraints on the problem, however, by making certain assumptions regarding the emissivity (*e.g.*, symmetry in some dimension or about some axis, "smoothing" equations, or "maximum entropy" equations) which may make it possible to arrive at some solution. However, depending on the assumptions which one makes about $\boldsymbol{\mathcal{E}}$, one is not necessarily assured that the solution obtained is a faithful reproduction of the actual emissivity function. The third possible case, in which $M > N$ (more detectors than pixels) has an overdetermined system with no exact solution. However, as will be shown, it is the most interesting and desirable one with which to work.

There are several ways to solve for $\boldsymbol{\mathcal{E}}$ in the case for which the number of equations (known detector signals) exceeds the number of unknowns (pixel emissivities). Iteration schemes have been developed in which an initial solution is assumed or guessed at, and then it is adjusted iteratively until a solution which matches the observed data to within some specified error is obtained. Iterative reconstruction algorithms are classified according to the sequence in which corrections are made and incorporated during an iteration, as this choice has a significant bearing on the performance of the algorithm. Several variations have been proposed and are described in the literature; they are referred to by their acronyms, such as ILST[26] (Iterative Least Squares Technique), SIRT[27] (Simultaneous Iterative Reconstruction Technique), and ART[28] (Algebraic Reconstruction Technique). The drawback of these reconstruction techniques is that the solution obtained is not necessarily unique (it may depend on the initial guess), nor does there appear to be any guarantee that the solution will converge to some final value as the number of iterations is increased.

Another approach is made possible by the advent of fast, modern computers. It is possible to solve Eqn. 16 in a reasonable amount of time by directly inverting the matrix **W**. In other words,

$$\boldsymbol{\mathcal{E}} = \mathbf{W}^{-1} \cdot \mathbf{S}. \tag{17}$$

This is similar to the case in which $M = N$, where $\mathbf{W}^{-1}$ is unique and well-defined provided that its determinant is non-zero. The problem with the exact solution is that, in practice, noise will be present in the measured signals, which can greatly alter the solution or make it impossible to find one because the system is so close to being underdetermined. With an overdetermined system, the equations are inconsistent and there exists no exact solution. However, it can be shown that in this case there is an "optimal" solution which minimizes the least squares error arising from the difference between the observed data and the solution. Of all the inverses of **W** which are possible in this situation, there is one in particular, denoted by $\mathbf{W}^{+}$ and known as the *pseudo-inverse* or *generalized inverse*, which yields the solution in the least squares sense.[29] The details of how this inverse is calculated will not be given here; it suffices to state that it can be uniquely determined and that there are commercial software packages readily available which provide routines for evaluating the pseudo-inverse of an $M \times N$ rectangular matrix.

The attractive feature of this method over the iterative reconstruction algorithms is that it does provide a particular solution to the problem which is well-defined and does not require one to make assumptions or initial guesses about the emissivity (except for the assumptions mentioned at the beginning of this section). Furthermore, the most attractive feature is that **W** need be inverted only once, because it depends on the detector and pixel geometry, which is presumed to be fixed. Once this operation is performed, the inverse can be stored in computer memory or on a computer disk file. Given a set of measured detector signals, the least squares fit solution for $\boldsymbol{\mathcal{E}}$ is found simply by one straightforward matrix multiplication, which is easy to program.

It is preferable to have the system substantially overdetermined; *i.e.*, to have M be greater than N by a large margin. The reason for this is that there will always be unavoidable random noise in the system, and hence the more equations (data) one has, the less sensitive the reconstruction will be to that noise. The situation is analogous to fitting a line to a large set of data points as opposed to fitting a line to only two data points. In the first case, one has a much more accurate determination of the line even though the line does not pass through all the points. The fit is not terribly sensitive to a small amount of random noise in the data. In the second case, however, only a slight change in one of the data points due to the introduction of noise can significantly affect the equation of the line. Studies have been done in which the Alcator C plasma cross-section was divided into about 100 square pixels, each 3 cm on a side;[18] what the overdetermination requirement translates into is that, for such a 100-pixel cross-section, one needs roughly 150 to 200 detectors placed around the periphery of the plasma in order to obtain reliable reconstructions using the matrix inversion method. Placing such a large number of detectors may not be feasible on a machine such as Alcator C, however, given the tight confines of its port space, which is mandated by the structure of the toroidal field magnet. Furthermore, the presence of other diagnostics and experiments on the machine may make it very difficult or impossible to mount such an array of detectors on the tokamak.

The finite element matrix inversion approach is thus conceptually simple and easy to implement on a computer, with the algorithm for it working extremely fast. It can handle odd geometric configurations, accomodating pixels of arbitrary shape and varying size (as long as they do not violate the requirement that each pixel's actual emissivity be approximately constant). Detectors need not be arranged in any specific way, such as in parallel arrays or having "fan-like" chords of view. Also, for a system which is sufficiently overdetermined, one need not make any *a priori* assumptions about the nature of the emissivity in order to obtain a reasonable solution.

As for disadvantages, one is that finite element techniques may be wasteful in the sense that the pixels can support arbitrarily complex emissivity patterns when only a simple one is enough to describe the soft x-ray emission. This problem may become particularly apparent when dealing with tokamak plasmas, which, for the most part, are thought to have emissivity cross-sections that contain only very low order Fourier harmonics (the plasma equilibrium is basically cylindrically symmetric except for a slight outward shift of its center). One thus needs only fairly simple patterns in order to describe the emissivity well. Secondly, as mentioned above, having a sufficiently overdetermined system may not be practical or feasible given the space contraints on Alcator C. Finally, it is still not possible to be ***completely*** assured that accurate reconstructions of the emissivity can be obtained, even for the case in which 150 to 200 detectors are viewing a 100-pixel plasma, until some other issues which need to be considered are investigated. Understanding this point requires some further analysis, and the reasons for it will be made clear in the following section.

II.2.2 *Analytic Methods*

The analytic methods which have been developed for tomographic reconstruction usually use one or two dimensional Fourier transforms. These techniques are based on having views of the emitting or absorbing region which are along chords through that region. The signal on each detector is thus the line integral of the emissivity or absorption function along its chord of view. These measurements are often referred to as *ray sums* or *ray projections.*[10]

Assume that one has an emitting plasma of arbitrary cross-section. The plasma must be of finite spatial extent, so that beyond some radius from a specified origin there is no soft x-ray emission. A circle, whose radius is normalized to unity, is imagined to enclose the emitting cross-section. Detectors are located around the periphery of the circle, with each one viewing the plasma along a chord defined by

its aperture and/or collimators. For the case of a tokamak, this viewing geometry is pictured in Fig. 7.

The chords are denoted by $L(p,\phi)$, because each one can be uniquely identified by its *impact parameter* or *radius* p (the perpendicular distance from the origin to the chord) and its *impact angle* ϕ (the angle the chord makes with the x-axis). Therefore, each detector's measurement is also uniquely specified by its viewing geometry. If the emissivity at each point (r,θ) along a chord $L(p,\phi)$ is $\mathcal{E}(r,\theta)$ (in watts-cm^{-3}), then the contribution of each point toward the total detected signal, measured in units of brightness, is given by $\mathcal{E}(r,\theta)dL$, where dL is the infinitesimal directed line element along the chord. Adding up all these infinitesimal contributions along the chord gives the total ray sum f corresponding to the particular p and ϕ:

$$f(p,\phi) = \int_{L(p,\phi)} \mathcal{E}(r,\theta)dL\,. \tag{18}$$

This expression holds true as long as the plasma is optically thin in the soft x-ray spectral region, which is the case for Alcator C.

However, because the dimensions of the emitting region are normalized to unity, one must write $dL = r_0 ds$, where ds is now a dimensionless line element and r_0 is the normalization radius of the unit circle. One then defines an *emissivity density function*, denoted by $g(r,\theta) \equiv r_0\mathcal{E}(r,\theta)$. Thus.

$$f(p,\phi) = \int_{L(p,\phi)} g(r,\theta)ds\,. \tag{19}$$

A complete set of these ray sums at a given angle ϕ is called a *projection* or a *profile*.[10]

As will be seen, the actual experiment has apertures which establish each detector's field of view, and the line chords become solid angles because of the finite size of the apertures. The measured quantity $f(p,\phi)$ is called the *brightness* and has units of watts/cm^2/steradian. Eqn. 19 can still be used, however, to describe correctly the detector signals if the width subtended by each solid angle "chord" remains small compared to the scale length of the emissivity's spatial variation as

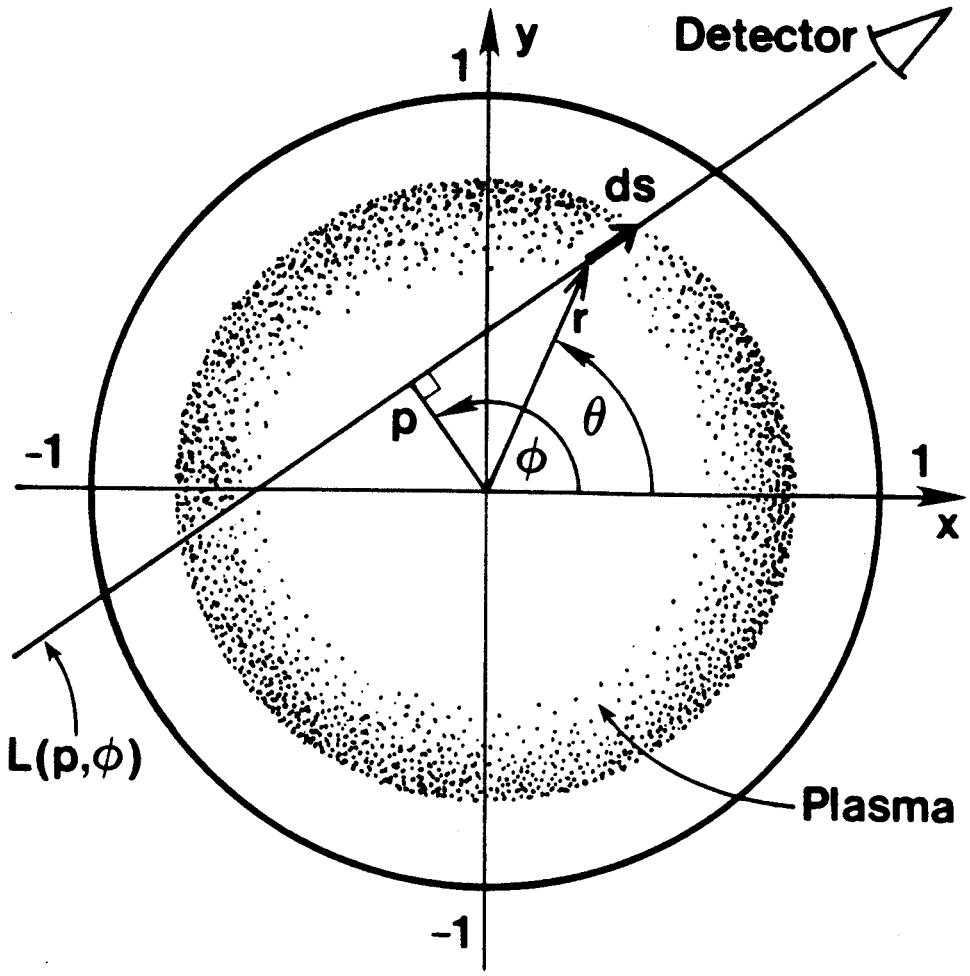

Figure 7 — Chordal viewing geometry. Note that the plasma *need not* be centered at the origin nor circular in cross-section for the purposes of the experiment.

one goes across the chord. In other words, the emissivity must not vary significantly over the width of the detector's field of view in the poloidal plane. This requirement imposes a limit on the size of the aperture in the poloidal direction, as that determines the extent of the chord's width in the cross-section. The emissivity is assumed to be uniform in the toroidal direction (over the extent to which it is viewed), so the width of the aperture in that direction need not be so strictly constrained. One can thus still approximate the measured quantity as a line integral along a chord which passes through the center of the solid angle defined by the aperture (see Fig. 8). However, as will be discussed in the next chapter, one does need to establish a relationship between what is actually measured (a detector signal in watts) and the brightness (in watts/cm^2/steradian). This relationship takes into account the effects of finite chord width and of chords which are not perpendicular to the plane of their detectors (*i.e.*, finite angle of incidence). Once these effects are incorporated into the calculations (it amounts to a constant geometrical factor for a given detector), the line integral formulation put forth here can still be used.

For the moment, the problem at hand is to invert Eqn. 19 in order to determine what $g(r,\theta)$ is. One can see that Eqn. 19 is a transformation from (r,θ) space into (p,ϕ) space, as the values of $f(p,\phi)$ are determined uniquely by the values of $g(r,\theta)$ along a given chord $L(p,\phi)$. The domain of f in the (p,ϕ) plane is the same as the domain of g in the (r,θ) plane—a circle of unit radius. Clearly, one needs an adequate sampling of (p,ϕ) space in order to have enough information to reconstruct the emissivity. For example, a detector configuration consisting of only a few arrays of parallel chords cannot reconstruct a complicated emissivity; the brightness $f(p,\phi)$ is sampled at many values of p but only at a few values of ϕ, so one lacks angular information. Consequently, only the lowest order Fourier harmonics in poloidal angle ($\cos m\theta$, $\sin m\theta$) could be resolved when reconstructing $\mathcal{E}(r,\theta)$. Similarly, one might have many chords covering a wide range of ϕ values, but if they all pass through the origin, for example, where $p = 0$, then information about the radial variation of $\mathcal{E}(r,\theta)$ is lacking. The necessity of having a sufficient sampling of (r,θ) or (p,ϕ) space exists for any tomographic reconstruction method,

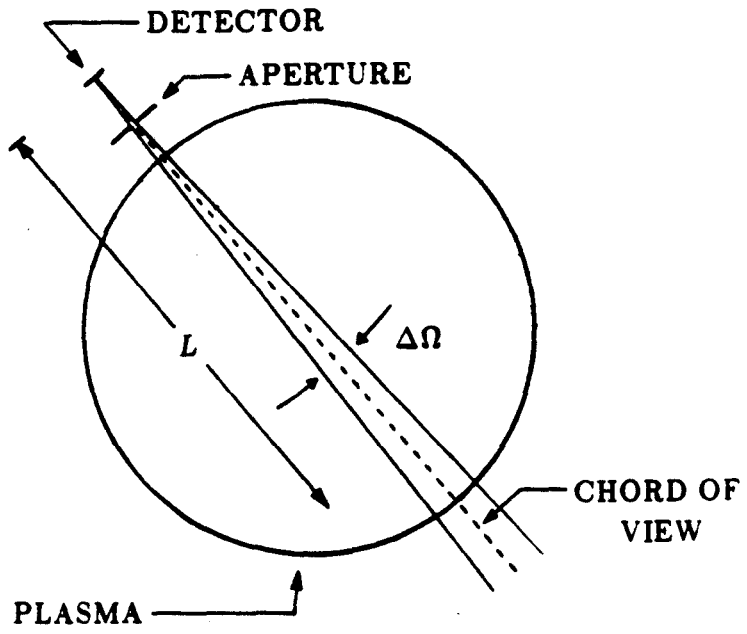

Figure 8 — Solid angle viewing geometry when finite aperture size is taken into account. If the width subtended in the poloidal plane by the solid angle $\Delta\Omega$ (shown here in a 2-D cross-section) is not too big compared to the distance over which $\mathcal{E}(r,\theta)$ varies, then one can describe the detector signal as a line integral of $\mathcal{E}(r,\theta)$ along the chord shown without incurring much of an error. Furthermore, at each point on the chord, the increase in the subtended area as one goes further along the chord is exactly cancelled out by the $1/L^2$ dependence of the radiation observed from each point.

and it explains why, as alluded to in the previous section, the pixel method does not necessarily yield believable reconstructions even when the system is considerably overdetermined. One must also have an arrangement of chordal views which will measure brightnesses at many values of both p *and* ϕ. Ideally, one would like to have chords which are equally spaced in both p and ϕ.

Assuming that one has detector measurements which adequately cover (p,ϕ) space, one can now proceed to solve for $g(r,\theta)$. The problem is two-dimensional, and Fourier analysis can be used to separate the coordinate dependencies and relate the Fourier coefficients of $g(r,\theta)$ to those of $f(p,\phi)$. In principle, all analytic reconstruction methods are equivalent, but the various forms of solution lead to significant differences in their implementation. One such method,[26] for example,

begins with the density function g expressed in rectangular coordinates. It is written as a two-dimensional Fourier integral in terms of the spatial frequencies k_x and k_y:

$$g(x,y) = \int_{-\infty}^{\infty}\int_{-\infty}^{\infty} dk_x\, dk_y\, G(k_x,k_y)\, \exp\left[2\pi i(k_x x + k_y y)\right] \tag{20}$$

where

$$G(k_x,k_y) = \int_{-\infty}^{\infty}\int_{-\infty}^{\infty} dx\, dy\, g(x,y)\, \exp\left[-2\pi i(k_x x + k_y y)\right]. \tag{21}$$

By appropriately rotating the (x,y) coordinate system of Fig. 7, one can write

$$G(k_x,k_y) = \int_{-\infty}^{\infty} dp \underbrace{\int_{-\infty}^{\infty} ds\, g(x,y)}_{f(p,\phi)}\, \exp(-2\pi i k p) \tag{22}$$

where $k^2 = k_x^2 + k_y^2$. The integral with respect to s is taken along the chord $L(p,\phi)$. It is therefore just the integral in Eqn. 19 for $f(p,\phi)$. Thus,

$$G(k_x,k_y) = \int_{-\infty}^{\infty} dp\, f(p,\phi)\, \exp(-2\pi i k p) = F(k,\phi) \tag{23}$$

where $F(k,\phi)$ is the Fourier transform in k of $f(p,\phi)$.

Eqn. 23 states that each Fourier coefficient of $g(x,y)$ is equal to the corresponding Fourier coefficient of the projection taken at the same angle as the Fourier wave. By measuring $f(p,\phi)$ and computing its transform in k, one has the Fourier coefficients of $g(x,y)$ and can thus reconstruct the emissivity by numerically integrating Eqn. 20. This procedure can be implemented on a computer using a Fast Fourier Transform (FFT) routine. The only assumption required is that the spatial resolution of the reconstructed emissivity be bandlimited to some maximum spatial frequency. However, in this experiment, this type of solution in not practical because there are not enough projections available due to the space constraints of Alcator C. The data, which are on a (r,θ) grid, would have to be mapped onto a rectangular coordinate system, and the large number of interpolative calculations which that entails renders this method prohibitively time-consuming.

Another approach involves the use of Fourier series expansions to decompose the two-dimensional problem into two one-dimensional problems, whose equations

can then be solved in order to obtain the desired result. A method which uses this tactic is the one developed by Cormack.[30,31] One begins by expressing both the density function and the brightness as Fourier series in cosines and sines:

$$g(r,\theta) = \sum_{m=0}^{\infty} \left[g_m^c(r) \cos m\theta + g_m^s(r) \sin m\theta \right] \tag{24}$$

and

$$f(p,\phi) = \sum_{m=0}^{\infty} \left[f_m^c(p) \cos m\phi + f_m^s(p) \sin m\phi \right] \tag{25}$$

where the superscripts c and s denote the Fourier cosine and sine coefficients, respectively. These coefficients are given by

$$g_m^{c,s}(r) = \frac{1}{2\pi} \int_0^{2\pi} g(r,\theta)(\cos m\theta,\, \sin m\theta)\, d\theta \tag{26}$$

and

$$f_m^{c,s}(p) = \frac{1}{2\pi} \int_0^{2\pi} f(p,\phi)(\cos m\phi,\, \sin m\phi)\, d\phi\,. \tag{27}$$

These expansions assume that $g(r,\theta)$, and thus $f(p,\phi)$, are well-behaved functions. Upon substituting the expressions for $g(r,\theta)$ and $f(p,\phi)$ into Eqn. 19, and using the fact that $s = \sqrt{r^2 - p^2}$ and $\theta - \phi = \cos^{-1}(p/r)$ (refer back to Fig. 7), one obtains

$$f_m^{c,s}(p) = 2 \int_p^1 \frac{r\, g_m^{c,s}(r)\, T_m(p/r)}{(r^2 - p^2)^{1/2}}\, dr \tag{28}$$

where $T_m(x) \equiv \cos(m \cos^{-1} x)$ is the m^{th} Tschebycheff polynomial of the first kind.

One now wishes to invert Eqn. 28 in order to obtain the Fourier coefficients $g_m^{c,s}(r)$. Cormack[30] showed that the solution to this problem is

$$g_m^{c,s}(r) = -\frac{1}{\pi} \frac{d}{dr} \int_r^1 \frac{r f_m^{c,s}(p)\, T_m(p/r)}{p(p^2 - r^2)^{1/2}}\, dp\,. \tag{29}$$

Note that if $m = 0$, $T_m(p/r) = 1$. It can be shown that in this case Eqn. 29 reduces to the familiar Abel inversion. Cormack[30] showed that $g_m^{c,s}(r)$ determines $f_m^{c,s}(p)$ in Eqn. 28 uniquely, and that the inversion formula in Eqn. 29 determines $g_m^{c,s}(r)$ uniquely.

A reconstruction based on direct numerical implementation of Eqn. 29 can be obtained. However, because it involves differentiation, such a solution can be very sensitive to noise present in the actual data. Nevertheless, it is possible to circumvent this problem by expanding $f_m^{c,s}(p)$ in some suitable series of functions which are complete in the interval $(0,1)$. Of all the possible sets of such expansions, Cormack[31] found a special one which leads to particularly simple expansions for the Fourier coefficients. For a given brightness measurement, let

$$f_m(p) = \frac{2}{m+2l+1} \sin\left[(m+2l+1)\cos^{-1} p\right] \tag{30}$$

where m and l are non-negative integers and $0 \leq p < 1$, and insert this expression into Eqn. 29. The result obtained after evaluating the integral is a relatively simple function which can be expressed analytically. One finds that $g_m(r) = R_{ml}(r)$, where $R_{ml}(r)$ is called a Zernicke polynomial and is defined by

$$R_{ml}(r) \equiv \sum_{s=0}^{l} \frac{(-1)^s (m+2l-s)!\, r^{m+2l-2s}}{s!\,(m+l-s)!\,(l-s)!} . \tag{31}$$

The different values of l which can be used in Eqn. 30 yield polynomials of different order. They are polynomials of degree $m+2l$ in r with r^m as the lowest power of r. These polynomials were originally developed by Zernicke[32] in connection with diffraction and are described in some detail by Born and Wolf.[33] They are orthogonal and form a complete set over the unit circle, so they can be used as basis functions for expanding any function within that domain. The problem is linear, so for a general set of measurements $f_m^{c,s}(p)$, an expansion of the form

$$f_m^{c,s}(p) = 2 \sum_{l=0}^{\infty} a_{ml}^{c,s} \sin\left[(m+2l+1)\cos^{-1} p\right] \tag{32}$$

will yield

$$g_m^{c,s}(r) = \sum_{l=0}^{\infty} (m+2l+1) a_{ml}^{c,s} R_{ml}(r) \tag{33}$$

where $a_{ml}^{c,s}$ are the (complex) expansion coefficients for $f_m^{c,s}(p)$ and $g_m^{c,s}(r)$.

The complete density function, $g(r,\theta)$, can thus be obtained from the sum in Eqn. 24; the emissivity $\mathcal{E}(r,\theta)$ is then found by multiplying this result by the

normalization radius r_0. The elegance of this approach is that it bypasses the numerical differentiation which one would have to perform in Eqn. 29 and yields a solution which is relatively insensitive to random noise in the numerical data or to detector positioning errors. It is because of this feature, the relative simplicity of the solution, and the practical constraints of the experiment, that Cormack's reconstruction method was chosen for this application.

In the actual experiment, $f(p,\phi)$ is measured at only a finite number of points in (p,ϕ) space. It might therefore be somewhat difficult to find $f_m^{c,s}(p)$ via Eqn. 27. Moreover, if the data are not regularly spaced on a grid in (p,ϕ) space, it is not possible to treat the angular harmonics and radial harmonics separately, unless one does a two-dimensional interpolation onto a two-dimensional grid. This interpolation is very time-consuming and usually yields unsatisfactory fits as well. In this situation, therefore, one needs to perform a full two-dimensional fit to the available data in order to determine the $a_{ml}^{c,s}$ coefficients. It is possible to show how this fit can be accomplished by using the assumed form of $f_m^{c,s}(p)$ from Eqn. 32 and substituting it into Eqn. 25. The result is

$$f(p,\phi) = 2\sum_{m=0}^{\infty}\sum_{l=0}^{\infty}(a_{ml}^{c}\cos m\phi + a_{ml}^{s}\sin m\phi)\,\sin\left[(m-2l+1)\cos^{-1}p\right]. \qquad (34)$$

Thus, one can obtain the $a_{ml}^{c,s}$ coefficients by performing a least squares fit to the $f(p,\phi)$ data points which are measured. Let there be N detectors in the system, and thus N distinct points in (p,ϕ) space for which one has a value of f. At each such point (p_n,ϕ_n), where $1 \le n \le N$, one has, from the previous equation,

$$f(p_n,\phi_n) = 2\sum_{m=0}^{\infty}\sum_{l=0}^{\infty}(a_{ml}^{c}\cos m\phi_n + a_{ml}^{s}\sin m\phi_n)\,\sin\left[(m+2l+1)\cos^{-1}p_n\right]. \qquad (35)$$

The quantities on the right hand side of this equation which depend on p_n and ϕ_n can be evaluated at each available (p,ϕ) point, so the only quantities which remain unknown are the $a_{ml}^{c,s}$ coefficients. Of course, it is not possible to take both sums to infinite values of m and l when numerically evaluating them, so one must truncate the sums at some maximum values of m and l. This truncation will determine the

degree to which angular and radial variations (represented by m and l, respectively) in the emissivity can be resolved. As long as one terminates the sums at values of m and l which keep the number of the unknown coefficients less than the number of known brightnesses, one can arrive at a least squares fit solution (this problem is similar to the one encountered in the pixel method, in which the pseudo-inverse was introduced in order to arrive at a least squares fit solution for the overdetermined system). If the maximum value of m is M, and that of l is L, then it can be easily shown that the sum for each $f(p_n, \phi_n)$ contains $(2M + 1)(L + 1)$ terms. There are thus N equations in $(2M + 1)(L + 1)$ unknowns. Therefore, by using some appropriate fitting algorithm, one can arrive at a solution for the $a_{ml}^{c,s}$ coefficients in the least squares sense, if the number of detectors exceeds the number of unknowns. Such is the case with this experiment, in which there are eighty detectors making brightness measurements of the plasma soft x-ray emission and low order harmonics ($m = 0, 1$ and $l = 0, 1, \ldots, 6$) are used to obtain the fit to the observed data.

It is worth pointing out that even if one has a limited number of views (as is the case in many actual plasma tomography experiments), it is still possible to obtain reconstructions using analytic solutions by making certain assumptions which effectively increase the number of available measurements. For instance, in some experiments,[11,13,14] it is assumed that the oscillations typically observed in soft x-ray signals are due to perturbations in the emissivity which rotate in the poloidal or toroidal direction. If one takes this rotation of the plasma fluid to be rigid, if the rotation frequency ω is constant in time and can be determined (either from the magnetic fluctuation signals arising from MHD oscillations or from the soft x-ray signals themselves), if the center of rotation can be ascertained (from the profile of the signals), and if the amplitude of the oscillation remains essentially constant during one period, then signals from one detector array at different times are equivalent to signals along chords at different angles. This situation is equivalent to having several "virtual" detector arrays around a stationary plasma, separated by a distance equal to that covered by the rotating plasma in one data sampling period (data acquisition is usually done by digitization at some fixed rate). The

angle ϕ is calculated from the expression $\phi = \omega t + \phi_0$, where ϕ_0 is the angle of the chord $L(p, \phi)$ at $t = 0$.

Clearly, however, assumptions about rotation will build into the emissivity certain features which might actually not be present; furthermore, there is no assurance that the plasma's rotation can always be taken to be rigid and uniform. In particular, if the rotation frequency varies with time, the location of the virtual detectors effectively changes, and hence the viewing geometry becomes time-dependent, which greatly complicates the problem. Non-uniform rotation requires more views of the plasma; the amplitudes and phases of the harmonics must be determined from an actual Fourier analysis of the mode structure viewed from as many directions as necessary so as to avoid aliasing.[11] Such a large number of views is generally not obtainable on tokamaks, so one must assume that only low order harmonics are present. For these and other reasons, therefore, it would be preferable not to have to resort to any assumptions about rotation.

There are other simplifying assumptions which one can make when there is an insufficient number of views to yield useful reconstructions. For example, these could involve postulating a specific functional form for the emissivity which has adjustable parameters.[16] One must then find the values of the free parameters which best reproduce the observed signals. In situations in which the number of views is very limited, only simple functional forms with one or two adjustable parameters can be assumed.

Because of the limitations inherent in the those reconstruction algorithms which require certain assumptions about the plasma emissivity to be made, one would like to have enough views, adequately distributed in (p, ϕ) space, to yield reasonably good reconstructions using the technique based on Cormack's solution described above. As will be demonstrated, the eighty views used in this experiment are enough to meet this objective, provided that only low order m and l harmonics are included in the reconstruction.

Chapter III

EXPERIMENTAL APPARATUS

III.1 Detector System

Designing an experimental apparatus with enough detectors to yield useful data for tomography on Alcator C is complicated by the fact that there is very limited viewing access to the plasma. Among tokamaks, the problem of having good views of and easy access to the plasma is particularly acute in Alcator C because of its compact Bitter magnet structure. The ports consist of stainless steel flanges which have very narrow slots leading into the vacuum chamber from the top, side, and bottom (see Fig. 2). Because of the stringent space constraints involved, it is necessary to find a detector system other than the silicon surface-barrier diodes which are typically used in other soft x-ray plasma diagnostics. Their fairly large size does not enable one to have the required number of views. Furthermore, the cost of many surface-barrier diodes would make this experiment prohibitively expensive. Fortunately, compact arrays of relatively inexpensive miniature PIN (p-intrinsic-n) planar-diffused silicon photodiodes are readily available commercially. They are intended to be used for visible light measurements, but they have been shown to work well as soft x-ray detectors and for the purposes of tomography.[34,35] Their small size and low cost not only allow for the placement of many detectors, but also for greater proximity of the detectors to the plasma, which leads to larger signals and thus an improved signal-to-noise ratio.

An assembly of eighty such detectors was placed on Alcator C. Forty of these viewed the plasma from the top, and forty from the bottom, at one toroidal location (the port designated as "C" port, one of six on the machine). Views from the side of the tokamak would have also been desirable, but the presence of a waveguide array for the lower hybrid RF heating and current drive experiments made that impossible. Other ports were not available, either because their dimensions are incompatible with the design of the apparatus, or because they were occupied by

other experiments. There is space available for more detectors on the top and bottom, but they were not installed because of a shortage of the required data acquisition and storage equipment.

The detector system is composed of individual arrays of photodiodes which are all situated at the same radius (approximately 22 cm) from the center of the vacuum vessel (the minor radius of the plasma in these experiments is the nominal 16.5 cm). A detector array consists of eight individual photodiodes on a common silicon substrate (a "chip"). Each detector has a 1.5 mm $\times$ 2.8 mm active area and a total silicon thickness of about 0.3 mm. The entire chip is soldered by the manufacturer onto a small printed circuit board with leads attached to each detector and a ground plane (see Fig. 9). The circuit board's sides are trimmed off so that it will fit in the required space; its final dimensions are about 6.4 mm $\times$ 19 mm. The chip of detectors is then mounted on a block of G-10 material (made of fiberglass and epoxy) which is designed to position each chip in the proper location and orientation for its designated view (see Fig. 10). The center conductor of a miniature coaxial cable is soldered to each detector lead, with the ground lead (the shield of each cable) common to all eight and eventually common to all forty detectors from a single port once they are connected their respective amplifiers. Aluminum tubes (outer diameter of $\frac{3}{8}$ in) are screwed into each G-10 block which carry the coaxial cables out to the entrance of the port at the top or bottom of the machine (approximately 1 m away from the edge of the vacuum vessel).

The viewing geometry of each detector is defined by an appropriately positioned aperture. The components of each array of eight detectors are placed inside a stainless steel tube. At the end of the tube there is a rectangular aperture to provide the desired view (the tubes are also part of the required vacuum system, which will be discussed in more detail in the next section). There is no significant transmission of soft x-ray radiation through the stainless steel, so the aperture serves to define each detector's field of view for a given chip of eight detectors. However, because the detectors are quite responsive to visible light (recall that they were originally manufactured to be visible light sensors), the aperture must

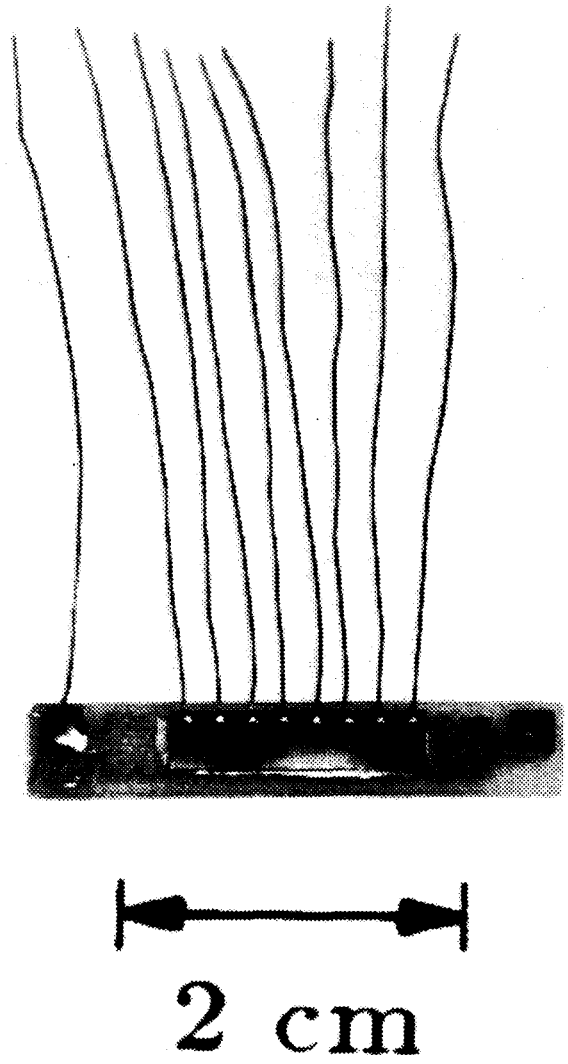

Figure 9 — PIN photodiode chip. There are eight detectors on the chip. The lead on the left is soldered to the ground plane on which the chip is mounted; it serves as a common connection onto which the appropriate bias voltage for all eight photodiodes can be applied.

Figure 10 — Detectors mounted on a G-10 block. A miniature coaxial cable is soldered to each detector lead. A strain relief is located just before the coaxial cables go into the block (it is clamped down by two nylon screws). Also visible beyond the block is the aluminum tube which takes the cables to the entrance of the port.

have the property that it does not let visible light from the plasma pass through while still remaining reasonably transparent to soft x-rays in the spectral region of interest. A very thin piece of beryllium has such properties, so an opening is machined at the end of each tube, where a 50 μm thick piece of beryllium is sealed onto the aperture. The dimensions of the beryllium aperture are 2 mm $\times$ 3 mm. Its thickness is determined by the requirements of the vacuum system and by the need to have the aperture allow soft x-rays to pass through it without too much attenuation, a factor which depends strongly on the beryllium's thickness. The area of the beryllium "window" is large enough to insure that the soft x-ray flux passing through it provides a good-sized signal on each detector; however, they are not so large that the view through the aperture has a solid angle which subtends too large a section of the plasma and, as discussed in Sec. II.2.2, would thereby invalidate the assumptions required to treat the problem as a line integral of the emissivity along a chord (*i.e.*, the aperture is no longer approximately a "pinhole"). The 2 mm dimension of the aperture in the poloidal direction yields a solid viewing angle which subtends about 2 cm in the poloidal plane near the center of the plasma. This figure is somewhat less than the scale lengths of the equilibrium density and temperature in Alcator C. It should thus be possible to satisfy the requirement that the emissivity not vary much over the distance subtended by each detector's solid viewing angle, as the density and temperature are the two parameters which most strongly affect the local emissivity values.

With each detector's view thus established, the photodiode arrays can be placed at their designated positions inside the tokamak to observe the plasma. The top and bottom ports both have three slots. In the central slot is placed a group of three separate detector chips (each with its own aperture) for a total of twenty-four detectors; the inner and outer slots have one detector chip each (and each has its own aperture) for the remaining sixteen detectors which comprise the 40-detector array that goes on the top or bottom port. The machine is symmetric about the

toroidal midplane, and so are the top and bottom arrangements of detectors. A diagram of the detector viewing design is shown in Fig. 11.

An important issue, as discussed in Sec. II.2.2, is whether or not the specified detector configuration provides an adequate coverage of (p, ϕ) space. One can plot points on a (p, ϕ) coordinate system that represent which chords $L(p, \phi)$ have signals measured along them (see Fig. 12). The extent to which these points fill up such a graph is a measure of how good one's coverage of (p, ϕ) space is. Because of the restrictions mentioned above which exist regarding the availability of space in Alcator C, the coverage is not optimal. The detectors are not equally spaced in p and ϕ, and they leave some regions of (p, ϕ) space completely unsampled. Nevertheless, as will be shown, the designed arrangement of eighty detectors does provide for satisfactory reconstructions of actual emissivity functions, as long as one is interested only in emissivities for which the poloidal and radial mode numbers are suitably restricted (how these restrictions are determined will be discussed later). Reconstructions with higher order harmonics would be meaningless, as the data obtained with the present configuration simply does not contain the necessary information.

One must also establish, for a given viewing geometry, the relationship between the signal in watts which is actually measured by a detector, and the brightness in watts/cm^2/steradian which is required for the reconstruction algorithm (this point was mentioned briefly in Sec. II.2.2). It is not immediately apparent that there does exist a direct relationship which allows one to express the measured quantity in terms of the line integral formulation of the tomographic reconstruction problem developed in Sec. II.2.2. In order to derive the required relationship, one must use the actual detector, aperture, and solid angle viewing geometry. Fig. 13 shows the geometry in question for a single chip of eight detectors and its associated aperture. Consider what the contribution to the total signal in watts on one detector is from a small radiating volume element δV_Ω in the volume enclosed by the solid angle through which the detector views the plasma. Assume that the emissivity $\mathcal{E}(r, \theta)$ does not vary much over the volume elements δV_Ω, and that the poloidal and toroidal angles covered by the solid angle are small (*i.e.*, $\delta\theta \ll 1$ and $\delta\varphi \ll 1$). One can then

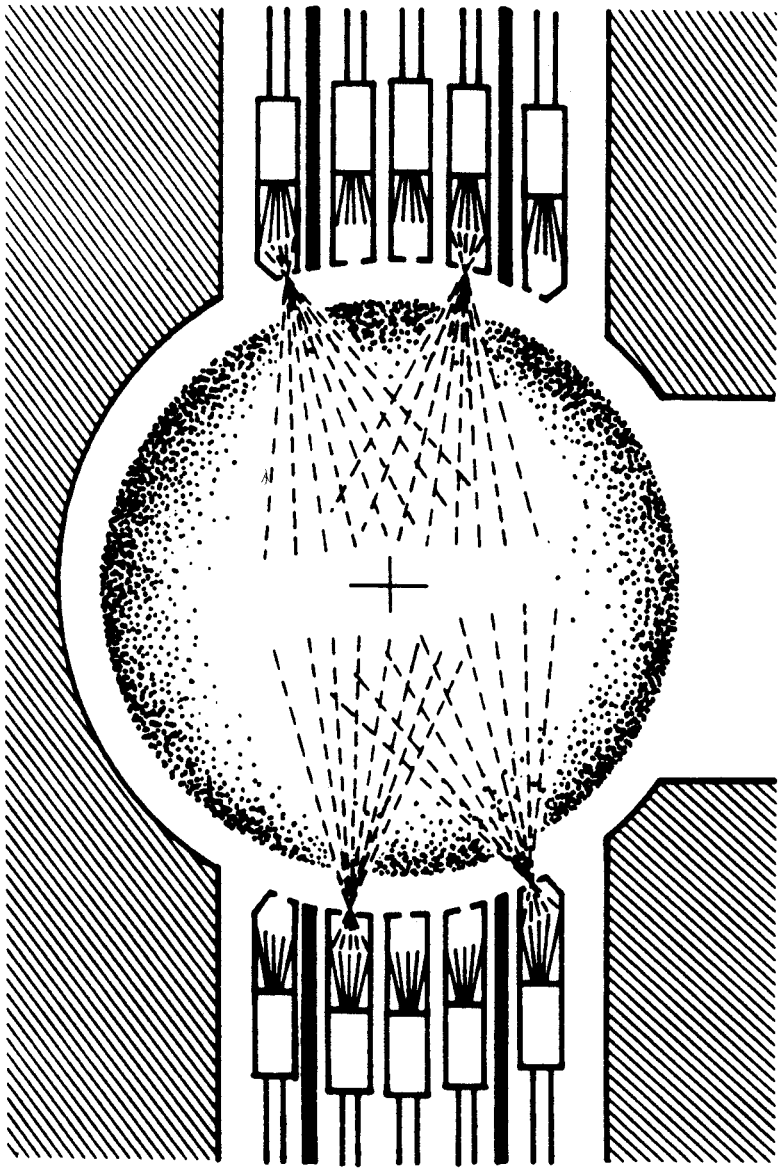

Figure 11 — Arrangement of detectors on Alcator C. Each set of eight detectors views through its respective aperture with the beryllium window, thus establishing "fan-like" chordal views such as the ones shown. The detectors are numbered 1–80, starting at the lower inside of the vacuum vessel and proceeding counter-clockwise from there.

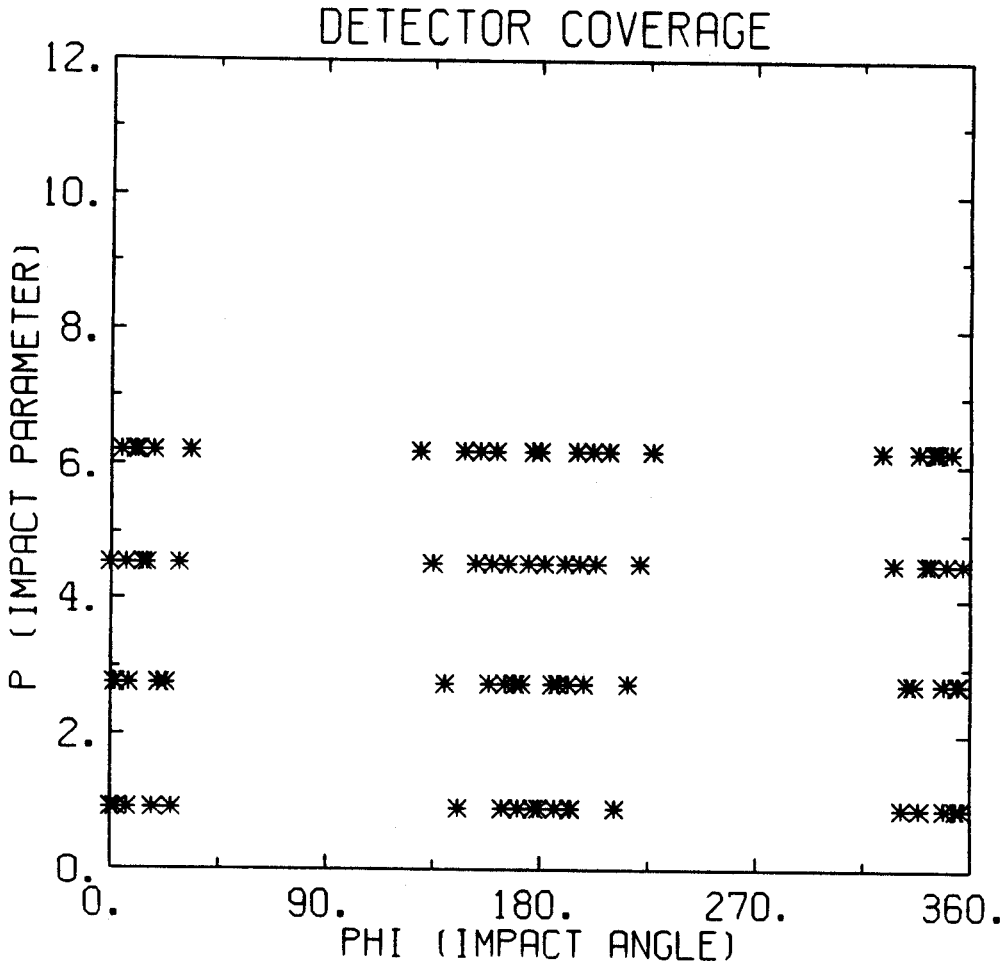

Figure 12 — Detector coverage of (p, ϕ) space for the viewing configuration of Fig. 11. Each point indicates the impact parameter and angle of each of the eighty viewing chords in the system.

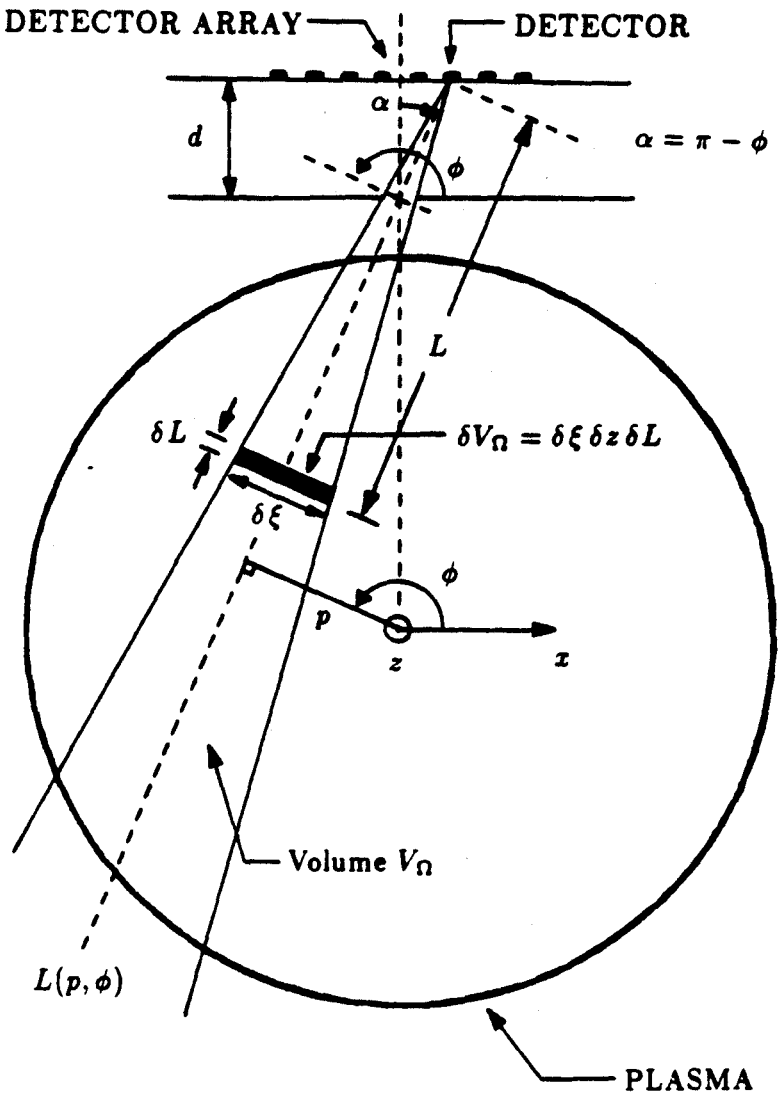

Figure 13 — Detector viewing geometry. The drawing is not to scale. The plane of the detectors has been oriented parallel to the x-axis for convenience only; any other orientation can be treated in the same way as described here.

treat the volume elements essentially as point sources. The detectors are treated as points of area A_d (they are small enough relative to other relevant dimensions that it is alright to think of them as points; one could divide the actual area of each detector into smaller elements or "chunks" and treat each one of those as a point in order to make a better approximation, but such an effort is not justified here). If the power from the volume element δV_Ω is being radiated isotropically, then the contribution from it to the power incident on one detector is given by

$$\delta P_i = \mathcal{E}(r,\theta)\frac{A_d \cos\alpha}{4\pi L^2}\,\delta V_\Omega\,. \tag{36}$$

The factor of $\frac{A_d \cos\alpha}{4\pi L^2}$ gives the fraction of the power radiated by the element which arrives at the detector of area A_d at a distance L. The factor of $\cos\alpha$ arises from the fact the the plane of the detector is oriented at an angle of incidence α with respect to the chord $L(p,\phi)$, and hence the detector "sees" less of the emission from δV_Ω by that factor. It should be pointed out that this calculation does not take into account the attenuation or filtering of the radiation due to the beryllium window. This effect will be discussed later.

One now needs to calculate $\delta V_\Omega = \delta\xi\,\delta z\,\delta L$, where $\delta\xi$ is the element of width which the solid angle of view subtends in the poloidal plane, δz is the length subtended by the solid angle in the z direction, perpendicular to the plasma cross-section (which corresponds to the toroidal direction), and δL is the line element of length along the chord $L(p,\phi)$. Referring to Fig. 13 again, one can write, by virtue of the fact that there are similar triangles,

$$\frac{\delta\xi}{L} = \frac{w_x \cos\alpha}{d/\cos\alpha} = \frac{w_x}{d}\cos^2\alpha \tag{37}$$

where w_x is the width of the aperture in the x direction and d is the distance between the planes of the aperture and the detector. The width w_x is effectively reduced by the factor of $\cos\alpha$ because the chord is at an angle α with respect to the plane of the aperture. Similarly, one also has

$$\frac{\delta z}{L} = \frac{w_z}{d/\cos\alpha} = \frac{w_z}{d}\cos\alpha \tag{38}$$

where w_z is the width of the aperture in the z direction. Notice that in this case w_z is not effectively reduced by $\cos\alpha$ because in the z direction the chord has no component in the plane of the aperture. One thus has

$$\delta\xi = \frac{w_x L\cos^2\alpha}{d} \tag{39}$$

and

$$\delta z = \frac{w_z L\cos\alpha}{d} \tag{40}$$

from Eqn. 37 and Eqn. 38, respectively. The last two equations yield

$$\delta V_\Omega = \frac{w_x w_z L^2\cos^3\alpha}{d^2}\,\delta L\,. \tag{41}$$

Substituting the previous equation into Eqn. 36 gives

$$\delta P_i = \mathcal{E}(r,\theta)\frac{A_d}{4\pi d^2} w_x w_z\cos^4\alpha\,\delta L\,. \tag{42}$$

Notice that the expression becomes independent of L, as the factor of L^2 in δV_Ω cancels the one in the numerator of δP_i.

The total power incident on the detector is therefore the sum of δP_i over all the small δV_Ω volume elements in the given solid angle. However, one can let $\delta L \rightarrow dL$ and express the sum as an integral, because it is only along the dimension specified by the chord $L(p,\phi)$ that one must perform the sum. Thus,

$$P_i = \int_{L(p,\phi)} \frac{A_d}{4\pi d^2} w_x w_z\cos^4\alpha\,\mathcal{E}(r,\theta)dL \tag{43}$$

gives the total signal in watts on the detector. Notice that $\frac{A_d}{4\pi d^2} w_x w_z\cos^4\alpha$ is a constant with respect to the integration along a given chord, as A_d, w_x, w_z, and d are all pre-specified parameters, and $\cos\alpha$ can be calculated from the known coordinates of each detector and its aperture. Furthermore, as can be seen in Fig. 13, $\cos\alpha = -\cos\phi$, so that $\cos^4\alpha = \cos^4\phi$. Hence, letting $K \equiv \frac{A_d}{4\pi d^2} w_x w_z$, one has

$$P_i = K\cos^4\phi \int_{L(p,\phi)} \mathcal{E}(r,\theta)dL\,. \tag{44}$$

Dividing this equation by $K\cos^4\phi$ yields

$$\frac{P_i}{K\cos^4\phi} = \int_{L(p,\phi)} \mathcal{E}(r,\theta)dL\,. \tag{45}$$

This quantity is a brightness and has units of watts/cm^2/steradians; it is exactly the expression for $f(p,\phi)$ given in Eqn. 18. Thus, one does indeed have the problem posed in Sec. II.2.2. The line integral of the emissivity gives a function of p and ϕ which can be inverted according the the techniques described in Sec. II.2.2; one need only adjust the measured quantity, P_i, by the factor $K\cos^4\phi$ for each detector in order to obtain a brightness which can be related to the emissivity via Cormack's reconstruction method.

To conclude this section, a brief discussion of how the detectors actually work and what their features are is presented here. Although the photodiodes are intended for use with visible light, the characteristics described herein also hold true in the case for which the incident radiation consists of soft x-rays. The photodiodes employed are commercially manufactured silicon PIN planar-diffused devices. A PIN photodiode is a diode in which a heavily doped p region and a heavily doped n region are separated by a nearly intrinsic and highly resistive i region. In its usual form of operation, the diode is reversed biased to such an extent that the intrinsic region is depleted of mobile charge carriers and the applied voltage produces a large electric field which extends across the entire region. Hole-electron pairs which are generated by photons absorbed in the i region can then be swept out of it by drifting in the electric field. These charge carriers produce a current in the external circuit to which the diode is connected. Under the appropriate operating conditions, the amount of current produced is directly proportional to the power incident on the diode; for the detectors used in this project, 3.3 μW of incident power yields 1 μA of diode current (according to the manufacturer's specifications).

The advantage of a PIN structure over an ordinary PN structure for photodetection is that the former has better response time, responsivity (sensitivity to incident light), and linearity. The diode is made in such a way that the i region is much longer than either the p or n region. The depletion region depth is thus

much larger in a PIN device that in a PN device, and it is this feature which leads to the better performance of PIN photodiodes, as incident photons are absorbed in the *i* region, and the optically generated charge carriers are then swept out by the applied electric field. In practice, however, it is found that the diodes work well even when zero bias voltage is applied to them, and for reasons which will be discussed in Sec. III.3, it was decided to operate them in this manner.

Typical dimensions for the devices used in this experiment are a 0.5 μm thick *p* region on top (where the radiation is incident), about 300 μm of intrinsic silicon, and a 1 μm thick *n* region at the bottom. There is also a 0.1 μm thick protective or "dead" layer of SiO_2 on top of the *p* region. Knowing the dimensions of the different layers in the device and thethickness of the beryllium window, one can calculate how efficiently a detector can absorb photons (*i.e.*, what fraction of the incident photons at a given energy is actually absorbed in the given thickness of silicon). The efficiency of detection can be found using the mass attenuation coefficients of beryllium and silicon as a function of the energy of the incident radiation (these numbers are tabulated). Fig. 14 shows a plot of the detector efficiency as a function of incident photon energy.

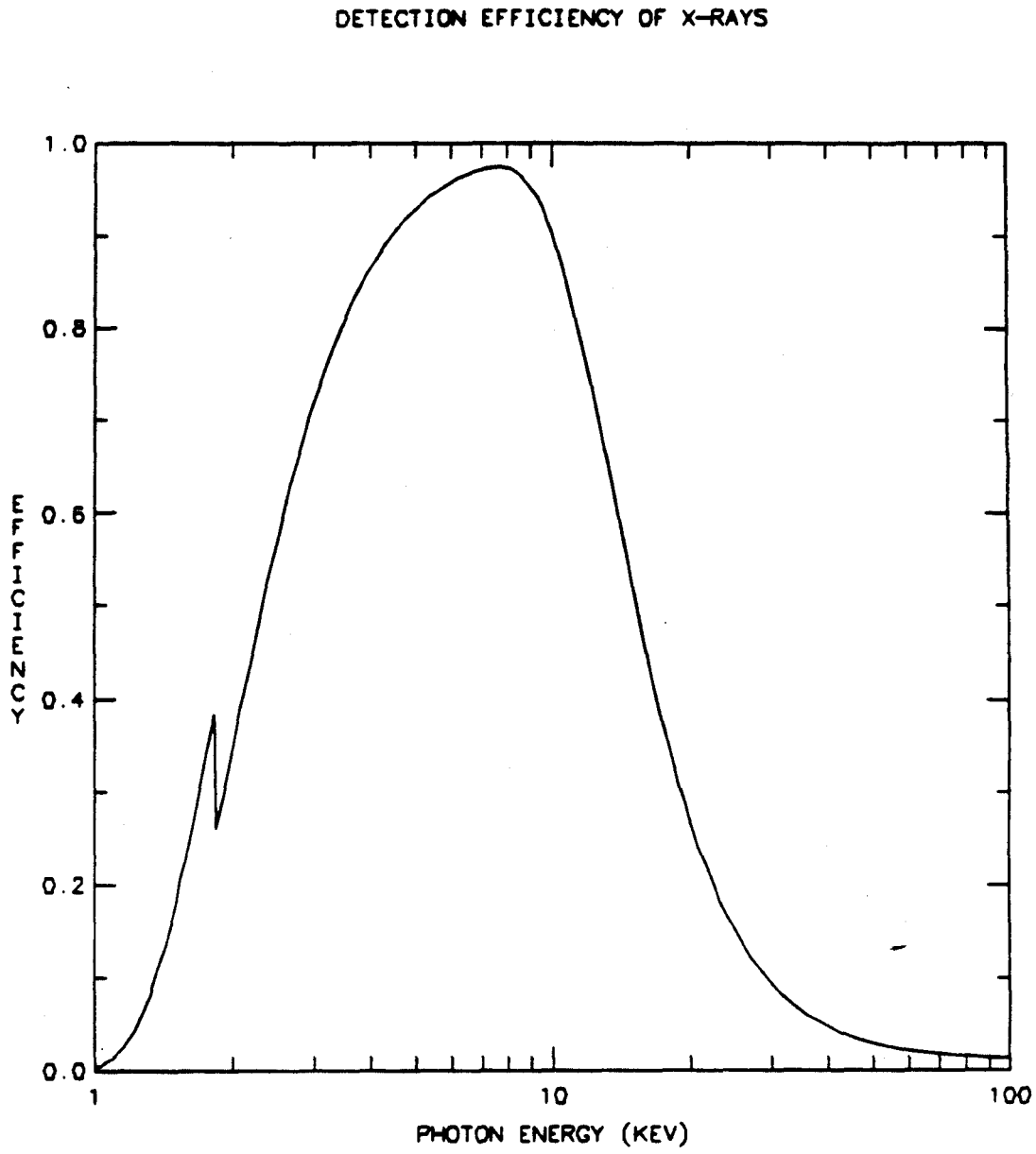

Figure 14 — Plot of detector efficiency (from Ref. 21). The sudden drop which occurs around 2 keV is the K-shell electron absorption edge in the silicon of the photodiode detector.

III.2 Vacuum System

If the ultra-high vacuum in Alcator C is to be maintained (which is on the order of 10^{-8} torr partial pressure of N_2; *i.e.*, air), it is necessary to isolate the components described in the previous section (detectors, G-10 blocks, cables, *etc.*) from the evacuated volume in the machine's vacuum chamber. Therefore, each chip/mounting block/aluminum tubing assembly (with eight detectors each) is slid down a stainless steel tube of rectangular cross-section ($\frac{3}{4}$ in $\times$ 1 in). At the detector end of the tube, 2 cm away from the plane of the detectors, the tube is sealed off by welding a stainless steel endpiece onto it. The $\frac{1}{16}$ in thick tube wall keeps the detector set-up isolated from the Alcator vacuum once the array is installed on the machine, and it also has the aperture which defines each detector's field of view. The beryllium windows are sealed onto each aperture by means of a high-vacuum epoxy in order to insure a good separation between the volume inside each tube and the Alcator C vacuum chamber. The thickness of the beryllium windows is determined by the need to have them be strong enough to withstand up to one atmosphere of pressure while still maintaining a good seal with the Alcator vacuum, and thin enough to allow soft x-ray radiation to pass through without unacceptably high attenuation. It is found that windows of 0.002 in (50 μm) thickness work well in this respect, as extensive vacuum tests were performed before actually installing the apparatus on the machine.

The other end of each tube is welded onto a small rectangular flange with an opening where the cables come out; these flanges are then bolted (vacuum tight) onto a 16-inch diameter rotatable flange. The 16-inch flange is in turn bolted onto the entrance of the port (which is a stainless steel "can") at the top or bottom of the machine in order to seal the Alcator vacuum off from the atmosphere. The volume inside the tubes can thus be maintained at atmosphere (or some other desired pressure), while outside the tubes is the Alcator vacuum. The final assembly is such that the tubes come down (or go up) from the 16-inch flange at the entrance to the port and enter the slots which lead to the edge of the vacuum vessel, where

the detectors are located. Fig. 15 and Fig. 16 show photographs of the stainless steel tubing assembly attached to the 16-inch flange.

On the outside of the 16-inch flange, a rectangular stainless steel enclosure (about 4 in $\times$ 4 in $\times$ 13 in) is bolted on so as to isolate a volume over the small flanges from which the detector coaxial cables exit. There is a $\frac{3}{4}$ in thick piece of plexiglas bolted on the top, with forty coaxial vacuum feedthroughs epoxied into holes which are drilled in the plexiglas.. The detector cables are connected on the inside of the enclosure to these feedthroughs, and cables connected on the outside then take the detector signals to the electronics and data acquisition systems. The enclosure has an outlet and valve so that it can be evacuated by an external vacuum pump. In this manner, the volume inside the tubes where the detectors are can be pumped down to some pressure less than that of atmosphere (a "rough" vacuum). The extent to which the pressure can be lowered is limited by the outgassing rate of the coaxial cable insulation and the plexiglas cover on the box. This part of the hardware is shown in the photograph of Fig. 17.

Having this external rough vacuum feature is desirable for two reasons. First, the beryllium windows are very thin and fragile and must withstand very high pressures, and if there should be a failure in one of them and a vacuum leak develops, one would not want to have the Alcator vacuum directly contaminated by the atmosphere. Having an intermediate vacuum system would mitigate the harmful effects of such a leak, and one could conceivably still keep the diagnostic operating on the machine, if the leak were small enough, by pumping continuously and maintaining the inside volume of the tubes reasonably well evacuated. The second consideration stems from the fact that Alcator's Bitter magnet is cooled by liquid nitrogen, and thus the temperature at the viewing end of the tubes can be quite low, as it is very near the magnet structure (the temperature in this area inside a tube has been measured to be about -95° C during the operation of the tokamak). If there were an atmosphere of air pressure inside the tubes, water vapor present could condense on the surface of the detector arrays, and the frost might lead to electrical short

circuits, cause damage to the beryllium windows, and attenuate the soft x-ray signals. An atmosphere of pressure in the 2 cm gap between the windows and the detector viewing surface would not attenuate the signal noticeably, but having that volume evacuated eliminates that loss as well. In practice, it is found that pumping down the detector assembly before each day's experimental run is sufficient to avoid the aforementioned problems. However, one of the beryllium windows did in fact develop a minor leak, which eventually required that the assembly on which it was be pumped continuously in order to avoid contamination of the Alcator vacuum and the formation of frost on the detectors.

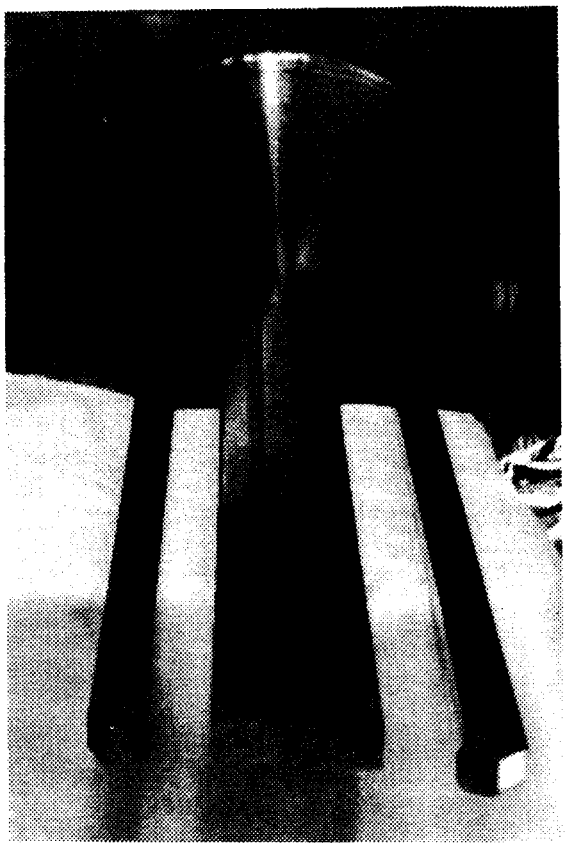

Figure 15 — Photograph of stainless steel tubing assembly attached to 16-inch flange (Alcator vacuum side). The beryllium windows can be seen at the end of each tube. The tubes are about 1 m long.

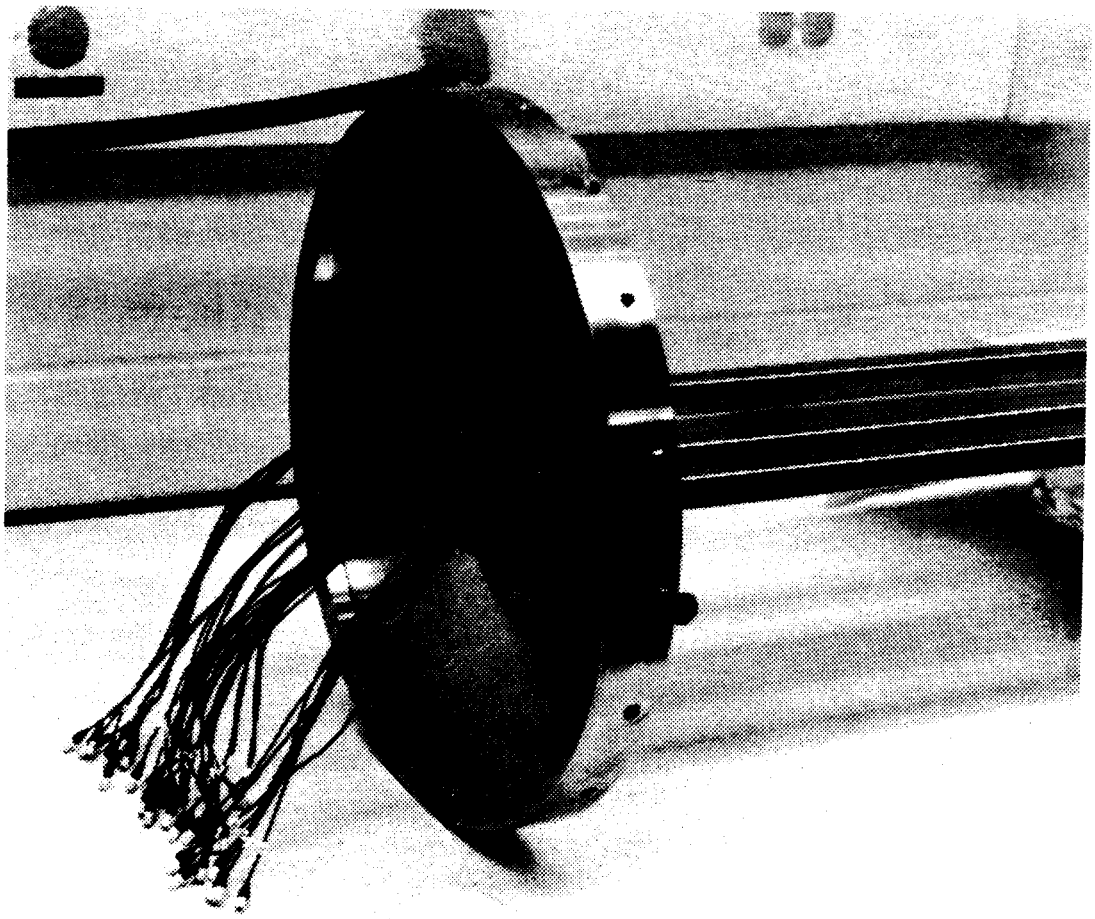

Figure 16 — Photograph of stainless steel tubing assembly (atmosphere side). The forty miniature coaxial cables from the detectors come out of the opening in the small rectangular flanges which are bolted onto the larger 16-inch flange.

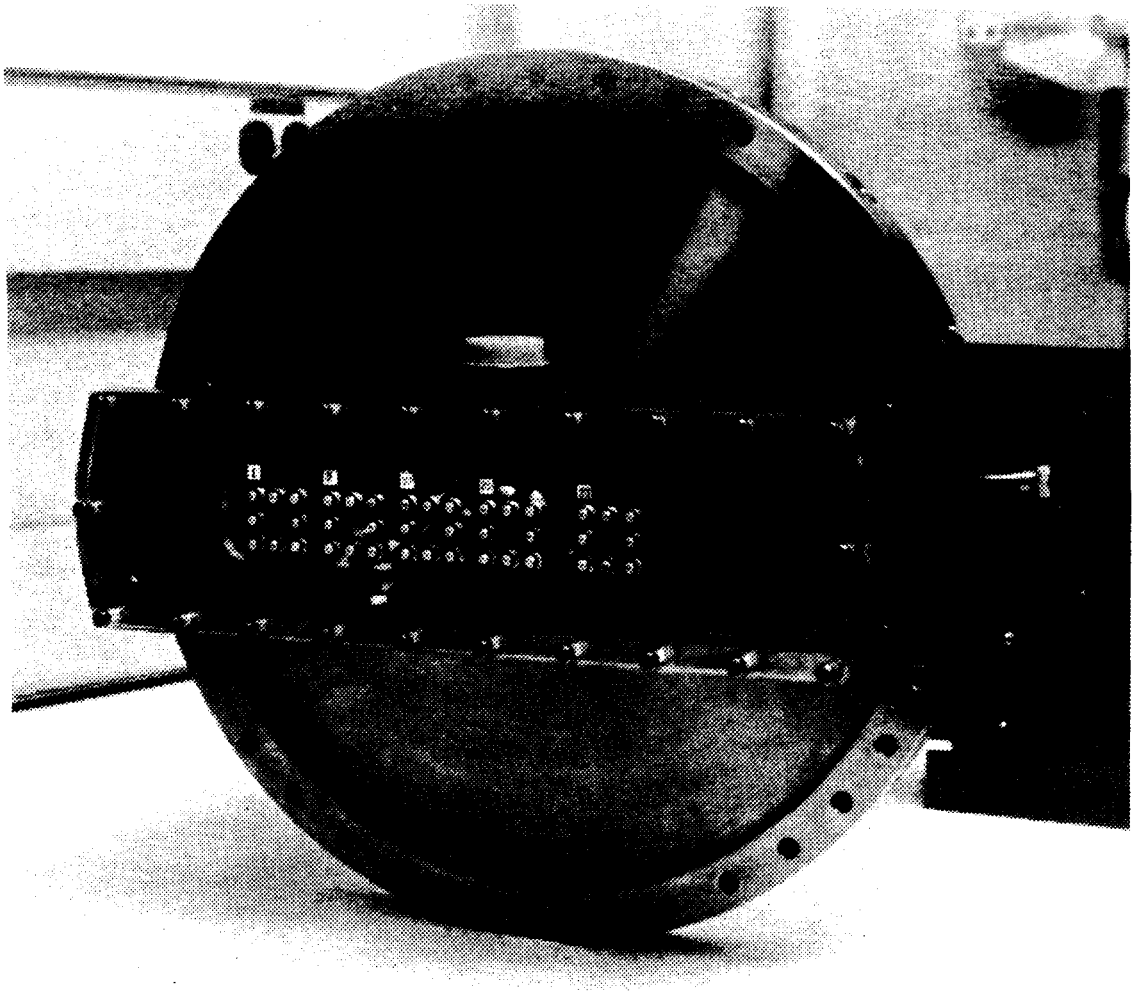

Figure 17 — Photograph of external rough vacuum enclosure, bolted onto the 16-inch flange. There are forty coaxial vacuum feedthrough connectors epoxied in the plexiglas cover which seals the enclosure. From there, cables go to the electronics.

III.3 Electronics, Data Acquisition, and Calibration

Once the power incident on each photodiode has produced a current, this signal must be measured and recorded so that it can be used for tomography. The first step in this process involves the use of miniature coaxial cables to transmit the signals from the detectors through the rough vacuum housing to the electronic circuitry which amplifies them. The rest of the process involves equipment designed to sample and record the data into a form which is compatible with the computer that will ultimately be used to perform the calculations which yield tomographic reconstructions. In order to obtain more understandable and reliable reconstructions, one must consider how the various components of the system affect or change what is being measured (soft x-ray power emitted by the plasma). Before any radiation at all is incident on the detectors, the beryllium windows alter the emission from the plasma, so one must understand the filtering effects of the beryllium windows. Furthermore, the detectors and electronics in this system must be calibrated somehow in order to account for the non-uniformity which exists among detectors and circuits and to have a more accurate representation of the relative magnitudes of the signals involved.

The first stage of the electronics is, of course, the photodiode detectors. As discussed in the previous section, PIN photodiodes are usually operated in a reversed biased mode in order to facilitate the efficient collection of the charge carriers generated by incident photons. In this experiment, however, it is found that a non-zero bias voltage produces an unacceptably high "dark" current (the current from the photodiode when no radiation is incident upon it). Also, no noticeable improvement in photodiode response is observed when the bias voltage is increased, as one would expect. Thus, in order to minimize the dark current, which produces an unwanted background signal, the photodiodes are operated in an unbiased mode. The I-V characteristics supplied by the manufacturer (shown in Fig. 18) indicate that a photodiode is still in the linear region of operation (for signals of interest) when the bias voltage is zero and a nearly zero load resistance is connected to it.

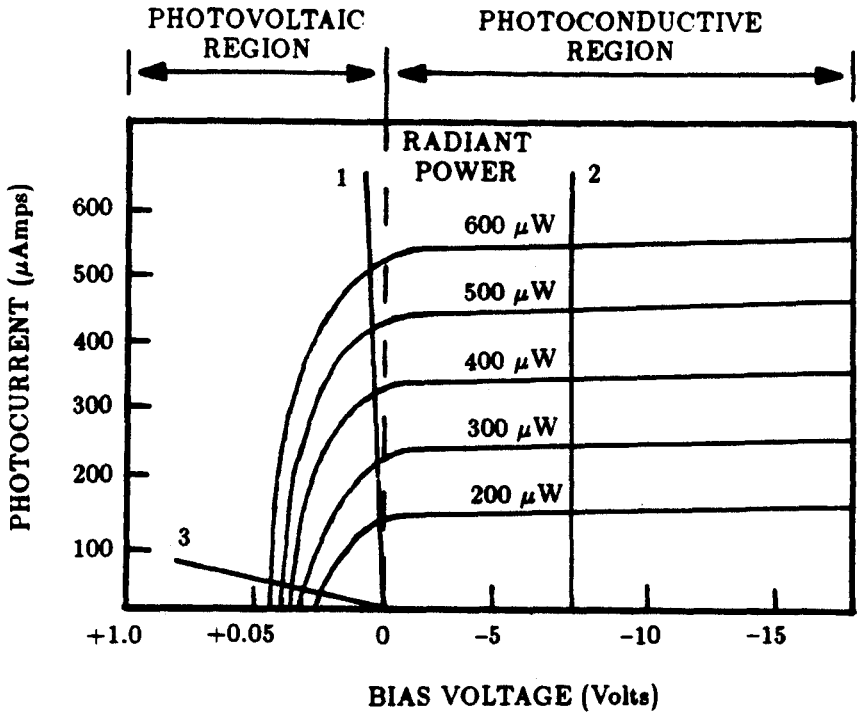

Figure 18 — I-V characteristics of PIN photodiodes. The signals measured in this experiment rarely exceed 100 μA, so the photodiodes are in the linear region of operation for load line #1, the one on which they were operated.

Such is the case in this experiment, as the amplifiers to which the photodiodes send their currents have a very low effective input impedance.

The amplifiers used in this experiment are commercially available logarithmic amplifiers (each one contained in an encapsulated package) which take the current signal from a photodiode as the input and produce an output voltage which is proportional to the logarithm of the input current. These amplifiers offer a good combination of fast response (200 kHz bandwidth at signal levels on the order of 1 μA), wide dynamic range (six decades: 1 nA to 1 mA), high precision (on the order of one percent maximum error), and relatively low cost. The transfer function for

these amplifiers is shown in Fig. 19. Using logarithmic amplifiers is found to be very convenient in this application. Because of the wide range of plasma parameters over which Alcator C can operate, the amplitude of the peak soft x-ray signal can vary considerably (the range of observed signals covers four orders of magnitude). If linear amplifiers were used, it would be necessary to incorporate some kind of "gain knob" into the system, and one would have to adjust it accordingly, depending on the signal levels expected. These levels can vary from discharge to discharge and from detector to detector. The measurement would therefore become somewhat problematic, because if the gain were not properly set, the recorded signals might be too small (not enough gain) or too large (saturation) in amplitude to yield useful results. However, logarithmic amplifiers enable one to follow the wide variation in signals without recourse to any gain adjustment. Fig. 20 is a schematic of the photodiode/amplifier circuitry.

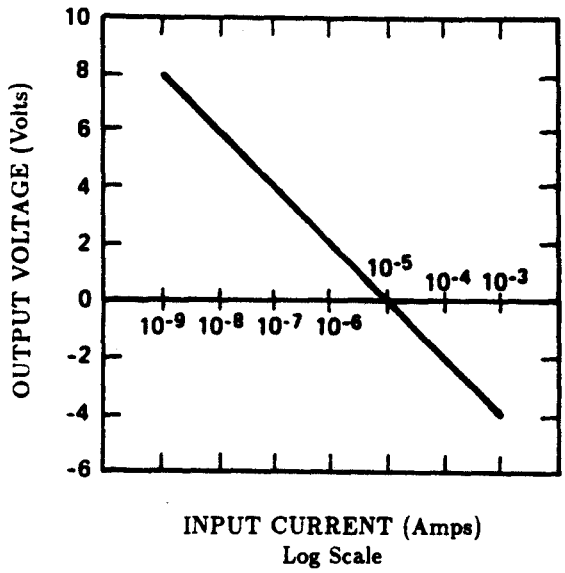

Figure 19 — Transfer function of the model 759N logarithmic amplifiers.

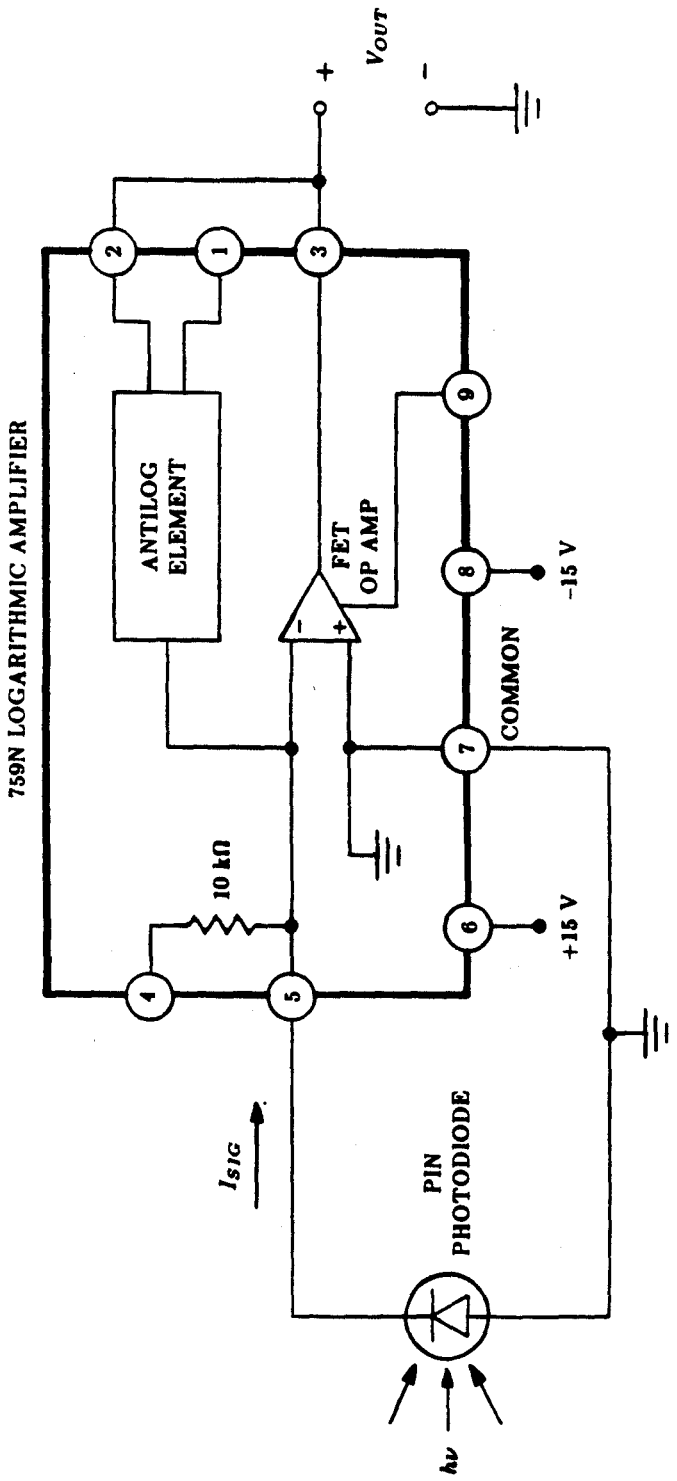

Figure 20 — Schematic of photodiode/amplifier circuitry, as used in this experiment. Pin #4 is used if the input signal is a voltage instead of a current. Pin #1 and/or pin #2 are used to set the scale factor for the output signal. Pin #9 can be used for an external trimming resistor.

Once the signals have been amplified logarithmically, a data acquisition system records them and eventually transfers them to a computer for subsequent data processing. The voltage signal outputs from the amplifier units are sampled in real time at 10 kHz by analog-to-digital converter CAMAC modules. Each sample has a resolution of twelve bits, which corresponds to about 2.5 mV resolution on a digitizer's -5 V to $+5$ V scale. The data are then temporarily stored in several CAMAC memory modules. In the time between plasma discharges ("shots"), which is usually about five minutes long, the data are read out from the memory modules via a CAMAC serial highway network which is interfaced to a VAX 11/780 computer. A data compression program structures the digitized data into a more compact format; they are then stored in a disk file and ultimately recorded on magnetic tape, from which one can retrieve the information later for analysis. The "raw" data (current signal from each detector) can be displayed almost immediately on a computer terminal CRT in order to determine whether or not the system is operating properly and for the purposes of premliminary examination. A block diagram of the electronics and data acquisition system is shown in Fig. 21.

As a result of the fact that there are so many channels of data (eighty) to be recorded and that data acquisition and memory units are expensive, and in the interest of not occupying too much disk space in the computer to which the data are eventually sent, one is limited in terms of how much information can actually be recorded and stored for a given plasma shot. Hence, data are usually taken only for a 200 ms time frame within a shot which, in these experiments, typically lasts for almost 600 ms (the time during which the plasma current is non-zero). The location of this time frame within the duration of the shot can be set beforehand by appropriate adjustments to the data system time sequencer which triggers the CAMAC digitizer modules. One must therefore anticipate which segment of the shot will yield the most interesting data; typically, this is during the time when the plasma current is constant ("flattop," which lasts roughly about 250 ms).

Once the data for each shot are finally recorded and stored in some suitable form, they can then be processed by the appropriate computer software in order

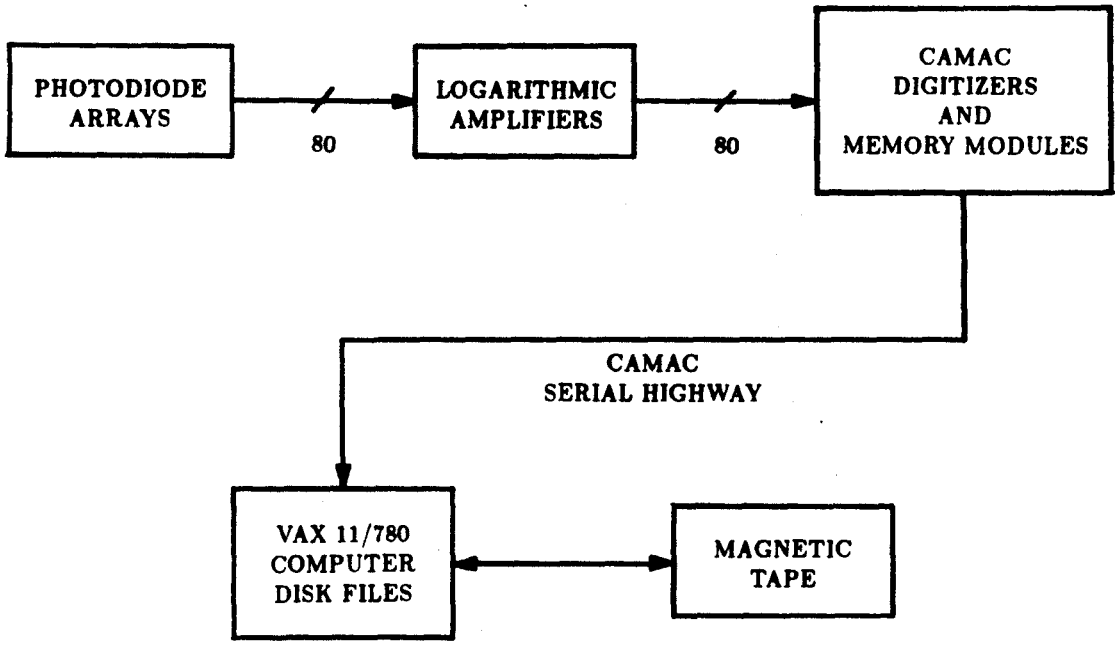

Figure 21 — Block diagram of electronics and data acquisition system.

to produce tomographic reconstructions of the emissivity. The computation should include those factors which account for the ways in which the quantity which one seeks to measure is modified by the components in the system. Specifically, one has to contend with the effects of the beryllium windows, which act as soft x-ray filters, the variation in performance from photodiode to photodiode and chip to chip, and any non-uniformities which might exist in the logarithmic amplifier circuits. One must therefore perform some sort of calibration measurement or have some other way of incorporating these effects into the reconstructions.

An absolute calibration measurement is of no interest in this situation, as the effect of the beryllium filtering, which cannot be fully accounted for unless one knows the complete spectrum of the radiation from the plasma, precludes the determination of an absolute emissivity level. Although the windows do allow soft x-rays of various energies to pass through at acceptable levels of attenuation, it still alters the radiation from the plasma in such a way that the actual numerical values of the emissivity cannot be determined unless one knows or makes assumptions about the energy distribution of the radiation emitted. What is actually measured can be described by considering how the beryllium windows affect the distribution of energies which characterize the radiation incident upon the detectors. If the frequency (or equivalently, energy) distribution of the radiated power density in the plasma is given by $dP_\nu/d\nu$, then the total "filtered" emissivity is

$$\mathcal{E}(r,\theta) = \int_\nu \frac{dP_\nu}{d\nu}\tau(\nu)\,d\nu \tag{46}$$

where $\tau(\nu)$ is the transmission function which indicates what fraction of the energy at a given frequency makes it through the 50 μm thickness of beryllium. The values of $\tau(\nu)$ range from zero to unity and can be readily obtained from the tabulated mass attenuation coefficients for beryllium. It is this emissivity in Eqn. 46 which appears in the expression for the brightness, $f(p,\phi)$, which is the line integral of $\mathcal{E}(r,\theta)$ along a chord $L(p,\phi)$. Notice that $dP_\nu/d\nu$ depends on various parameters in addition to frequency, such as density and temperature, but these quantities can be expressed as functions of position, and thus $\mathcal{E}$ is written in terms of r and θ. In order

to obtain the actual emissivity of the plasma, one has to determine what $dP_\nu/d\nu$ is and integrate it over all frequencies. This information is virtually impossible to unfold from the data under the present circumstances, as the actual spectrum of the radiated power can vary significantly (depending on the conditions of the discharge) and is very difficult to ascertain in its entirety. Thus, the reconstructions obtained in this experiment *do not* have the magnitude of the emissivity corrected for the effects of the beryllium windows.

One can obtain an estimate, however, of how much the calculated emissivities would have to be modified by considering the case in which $Z_{eff} = 1$. At the temperatures of interest in Alcator C, this situation will lead to a spectrum which is dominated by bremsstrahlung radiation. One could then use the expression for $dP_\nu/d\nu$ in Eqn. 13 and evaluate the integral in Eqn. 46 to find that the correction factor is approximately four. The degree to which the correction factor is greater than this number is a measure of the extent to which impurity radiation contributes to the soft x-ray emission and is essentially the emissivity enhancement factor discussed in Sec. II.1.2. It is clear, therefore, that this experiment can yield useful information, even if the beryllium filtering is not accounted for. The general shape and qualitative features of the emissivity function will still be reflected in the uncorrected measurement, and any fluctuations which may be indicative of MHD or other interesting phenomena should still be observable.

Another useful piece of information is the relative calibration factor of each detector. These numbers can be obtained by measuring the signal from each detector when they are all exposed to the same source of x-rays. By computing an average signal based on those measurements and then calculating how much each detector signal differs from that average, one has a notion of how much the detectors deviate from being uniform in their response to incident power. These measurements were conducted over a range of energies (a few keV to about 30 keV) by using a laboratory x-ray source in order to observe how the detector response varies as a function of the incident energy over the range of interest. It is found that the response is

essentially independent of the energy of the incoming radiation, and that the variation from photodiode to photodiode and chip to chip is quite small. The detectors all have relative calibration factors close to unity, exhibiting a standard deviation of about four percent around the mean signal. These measurements were made with each detector connected to the same amplifier used when taking actual data on Alcator C. The relative calibration factor thus also includes any possible effects arising from variations in the amplifier electronics. In addition, voltage calibration factors were determined for each channel of the CAMAC modules which digitize the data. By incorporating these factors into the computations which yield the reconstructed emissivities, one can compensate for the relative variations which are present among the eighty channels of data by simply applying a constant multiplicative correction to each signal.

Chapter IV

EXPERIMENTAL RESULTS

IV.1 Testing the Reconstruction Algorithm

As discussed in Sec. II.2.2, the tomographic reconstruction method developed by Cormack was chosen for the purposes of this experiment, and it is implemented in a computer code. The program takes the voltage signals recorded by the CAMAC data acquisition system, converts them to current signals via the transfer function of the logarithmic amplifiers, converts these signals to their equivalent in watts and then brightness, and then calculates the emissivity based on the algorithm described in Sec. II.2.2. The emissivity is computed at a single point in time during a given plasma shot. The code produces plots of the emissivity and other calculated quantities, as well as plots of the raw signals. The calculations involved in performing a reconstruction based on eighty channels of data typically take about three seconds of CPU time on a VAX 11/780 computer; the total amount of CPU time is somewhat longer due to the several plots which are generated.

In order to test the algorithm, another code is used to generate the signals that should appear on each detector for any specified emissivity function, based on the given viewing geometry. These test signals are then given as inputs to the reconstruction code. The emissivity function produced by the code is compared with the originally specified function. A useful means of comparison is to plot the Fourier components of the input and reconstructed emissivities as a function of radius for each poloidal mode number m. Based on this comparison, one can assess how faithful a reproduction of the prescribed emissivity function the reconstructed one is. One can also introduce random or systematic errors into the simulation and observe how sensitive the algorithm is to them. It is on the basis of such tests, by a process of trial and error, that it was determined that believable reconstructions are obtainable for the given coverage of (p, ϕ) space if one restricts the range of the m and l mode numbers (poloidal and radial, respectively) to be $m = 0, 1$ and

$l = 0, 1, \ldots, 6$. This range of mode numbers satisfies the constraint that the number of unknown $a_{ml}^{c,s}$ coefficients not exceed the number of known brightnesses (recall the discussion in Sec. II.2.2 regarding the solution for the $a_{ml}^{c,s}$ coefficients). It is also possible to satisfy this constraint by extending the maximum poloidal mode number to $m = 2$ and reducing the maximum radial mode number to $l = 4$, for example, and thereby increase the ability to resolve the poloidal mode structure. In this situation, one has to sacrifice some of the radial resolution in exchange for the increased poloidal resolution. For the case of functions without much radial variation, this set of mode numbers may yield an adequate reconstruction, and the trade-off in resolution may be acceptable. However, simulations show that functions whose poloidal components do possess appreciable radial variation cannot be reliably reconstructed because of the decreased ability to resolve the radial structure. The primary interest of this work is in being able to reconstruct, with a reasonable degree of confidence, the $m = 1$ component present in the emissivity, so it is preferable to limit the maximum poloidal mode number to $m = 1$ and opt for the best radial resolution which can be obtained in that situation. Tests show that, in this case, optimal reconstructions are performed when the maximum radial mode number is $l = 6$ (beyond that, and with the introduction of noise, the reconstructions begin to exhibit oscillations in radius which are not present in the input functions).

In Alcator C, it is observed that the measureable soft x-ray emission goes to zero around $r \approx 10$–11 cm ($a = 16.5$ cm is the minor radius of the plasma) because of the decreased temperature and density beyond that radius and the filtering effects of the beryllium windows. Thus, for the purposes of the reconstruction algorithm used here, one seeks to force the emission to zero for $r > 10$ cm. By artificially introducing data points for $f(p, \phi)$ of zero value at various angles ϕ in the range $10 < p \leq 12$ cm, the least squares fitting routine which computes the $a_{ml}^{c,s}$ coefficients in Eqn. 35 can more readily produce fits to the data which go to zero smoothly at $r \approx 10$ cm and remain zero thereafter. Computer tests show that the introduction of ninety-six such data points of zero value does not alter the fits which one obtains for the $m = 0$ component, and it makes it possible to obtain realistic fits which go

to zero smoothly and without undue oscillations for the $m = 1$ component. As there is never any signal beyond $p = 12$ cm, the normalization radius r_0 which appears in the definition of $g(r,\theta)$ in Eqn. 19 is taken to be $r_0 = 12$ cm.

Using these assumptions, various emissivity test functions are used to establish the performance of the reconstruction algorithm and its sensitivity to errors and noise in the data. As an extreme case, one can attempt to reconstruct an emissivity function which is hard to reproduce exactly using only low-order mode numbers. One such function is an emissivity which is constant out to a certain radius and then drops instantaneously to zero and stays there beyond that radius (a "step" function in radius). An infinite number of radial harmonics is required in order to generate an exact fit, and the discontinuity in the function at the radius where it goes to zero makes it difficult to obtain a good reconstruction because of the rather sparse coverage of (p,ϕ) space and the limited number of m and l values. Fig. 22 shows the result of a reconstruction in which the input function is $\mathcal{E}(r,\theta) = 0.2$ watts/cm^3 for $r \leq 10$ cm, and $\mathcal{E}(r,\theta) = 0$ for $r > 10$ cm (0.2 watts/cm^3 is a typical uncorrected emissivity level). Notice that the simulation is performed under the assumption that no beryllium windows are present in the apertures; hence, there is no attenuation or filtering factor included in the calculation of the detector signals when the simulation code computes the line integrals of $\mathcal{E}(r,\theta)$ along each chord $L(p,\phi)$. One can see that even with the low harmonic numbers used, the reconstructed function does not deviate too badly from the input function, except for the "overshoot" (Gibbs phenomenon) which is expected in a situation such as this one. The reconstruction in this case is made particularly difficult because of the fact that $\mathcal{E}$ is non-zero out to $r = 10$ cm, whereas the data are available only out to $p = 6.2$ cm. The residual "ripple" noise in the reconstruction is about five percent.

It is also important that no spurious harmonic content be introduced when attempting to reconstruct functions which do not possess certain poloidal mode numbers. Ideally, in the case of a constant emissivity test function, there should be no Fourier component for $m = 1$, as a uniform emissivity function has no poloidal variation (no effort is made to recover higher order poloidal mode components).

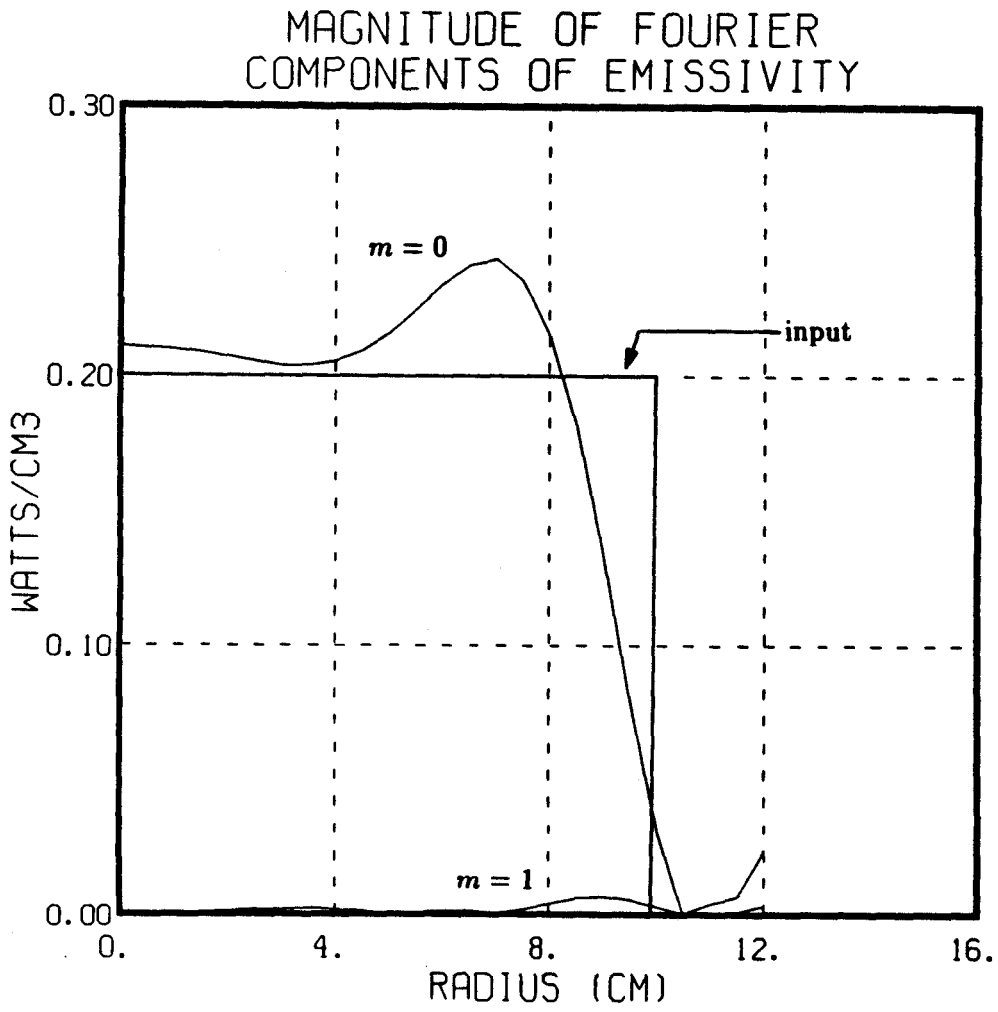

Figure 22 — Test reconstruction of uniform emissivity function (Fourier components).

That the introduction of non-existent harmonics does not happen is evident, as there is no appreciable $m = 1$ component in the reconstruction of the constant emissivity function. One can thus be confident that the numerical calculations performed yield good fits even when the input function has stringent conditions for matching it. Furthermore, the process does not produce artifacts in the reconstruction when the mode numbers are suitably restricted.

Another case which is simulated is that of a peaked emissivity function. A convenient function to use is a Gaussian, as many equilibrium ($m = 0$) emissivities exhibit Gaussian-like shapes. The plasma equilibrium is also usually shifted about a centimeter toward the outside (due to the Shafranov shift). In order to incorporate this feature into the test, the Gaussian emissivity input function has its peak shifted both vertically upward and horizontally outward by one centimeter with respect to the center of the vacuum vessel, which is taken to be the origin of the coordinate system (a vertical shift is also included in order to test the algorithm's ability to reconstruct up-down shifts, if there are any). In order to illustrate the intermediate steps in the reconstruction process, the computer code generates a plot of the brightness measured on each detector channel, which can be seen in Fig. 23. The code also produces a plot of the brightness data in (p, ϕ) space and of the surface which is fitted to that data from the least squares fitting routine that computes the $a_{ml}^{c,s}$ coefficients. Such a plot is given in Fig. 24. As one can see in Fig. 25, the reconstructed functions match the input functions rather well. Fig. 26 shows a plot in the poloidal cross-section of the contours of constant emissivity values for the reconstructed emissivity; from it, one can see that the peak of the emissivity is horizontally and vertically displaced by about +1 cm from the origin, as it should be. A three-dimensional plot of the reconstructed emissivity is shown in Fig. 27.

One of the goals of this experiment is to observe the magnetic island structure associated with the $m = 1$ resistive tearing mode, which is believed to occur during sawtooth oscillations. Thus, another useful test is to reconstruct an emissivity input function which simulates an $m = 1$ island structure. Fig. 28 shows such a reconstruction, and Fig. 29 is a contour plot of the reconstructed emissivity. Again,

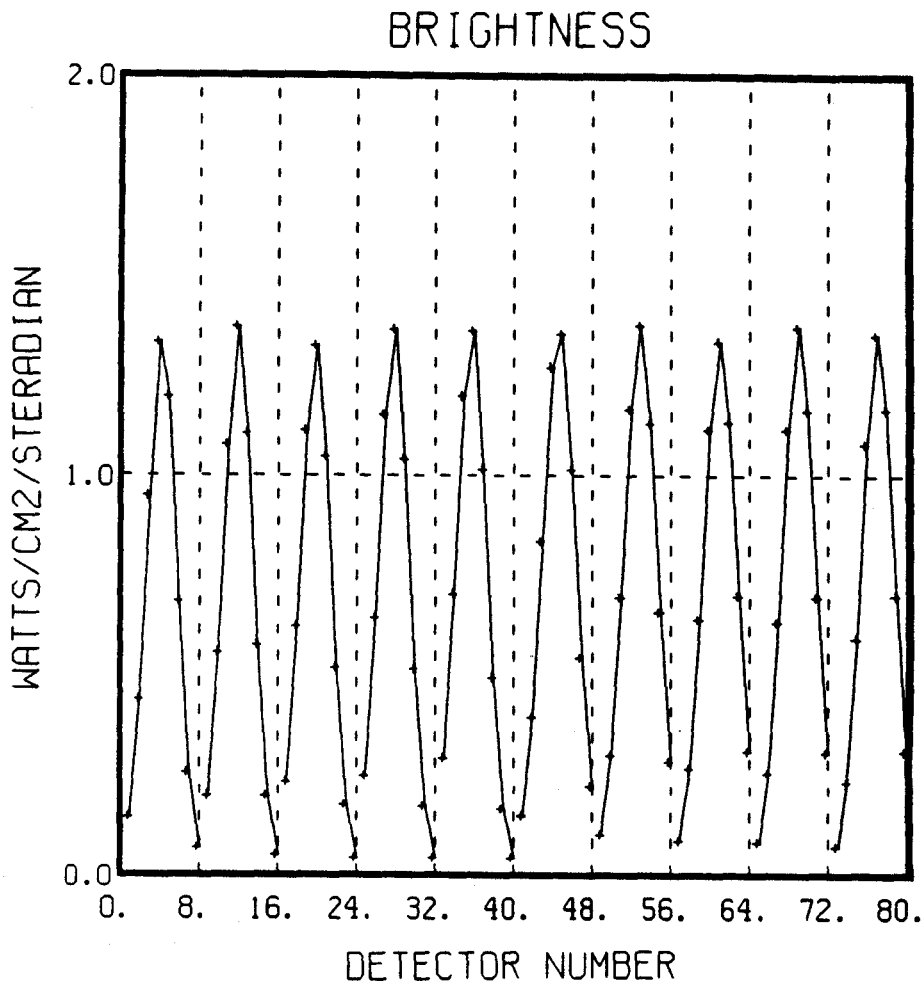

Figure 23 — Brightness test data from a shifted Gaussian emissivity function. The detectors are numbered 1-80, starting at the lower inside of the vacuum vessel and proceeding counter-clockwise from there (see Fig. 11). Each set of eight detectors comprises one photodiode chip and hence one "fan" of views, yielding the profiles shown above.

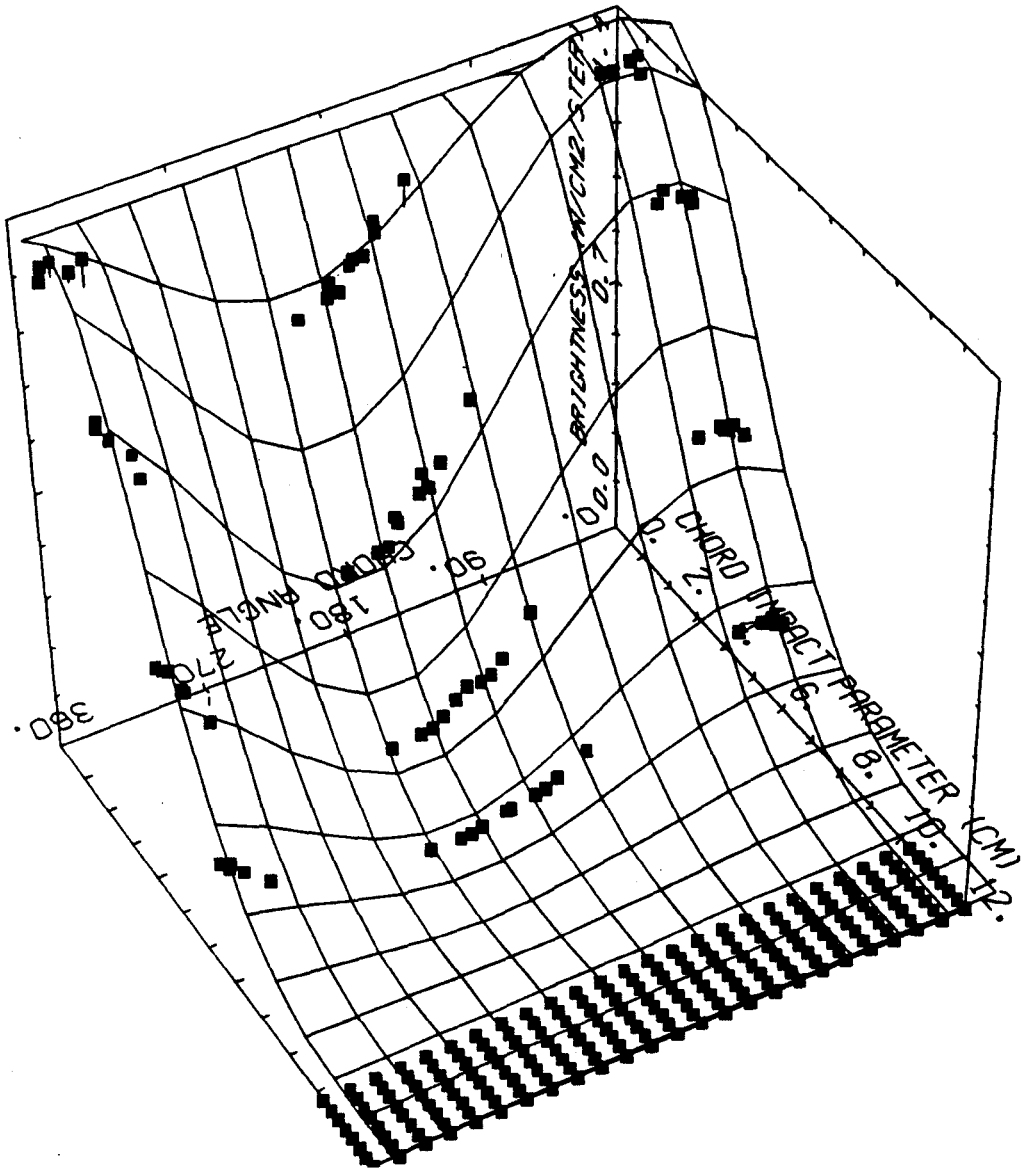

Figure 24 — Brightness test data and fitted surface in (p, ϕ) space for a shifted Gaussian emissivity function. Solid lines from a point to the surface indicate that the point is above it, whereas dashed lines from the point to the surface indicate the opposite. The artificially introduced zero values for $f(p, \phi)$ can be seen at the largest values of the chord impact parameter p. It can be seen that the fit of the surface to the $f(p, \phi)$ data points is a good one.

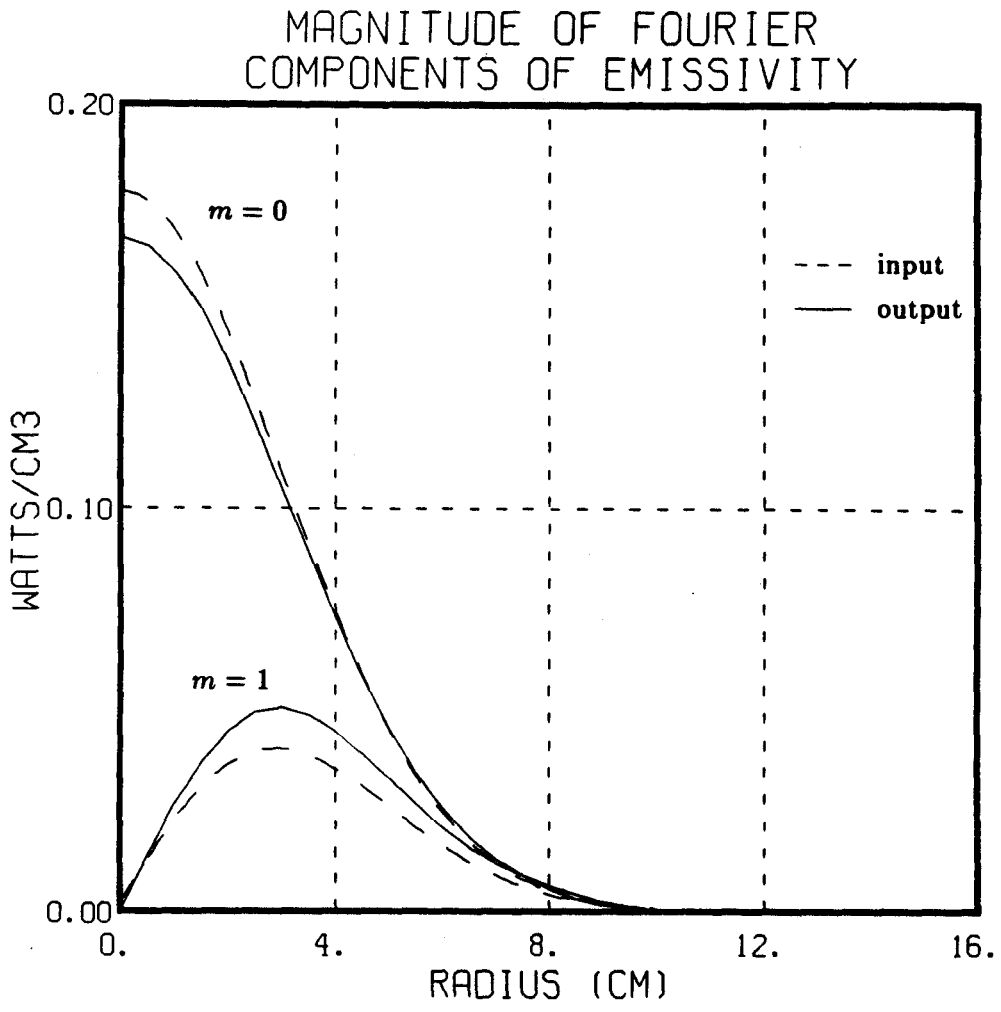

Figure 25 — Test reconstruction of shifted Gaussian emissivity function (Fourier components).

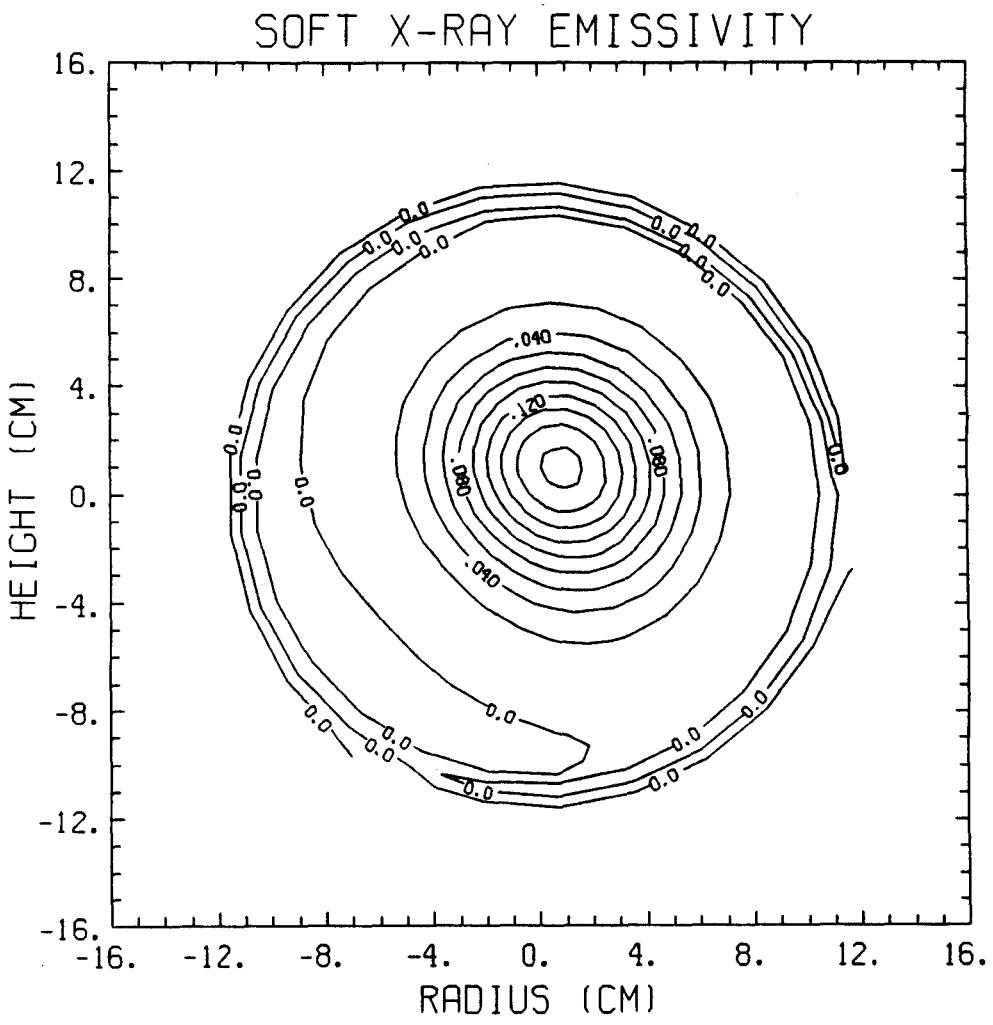

Figure 26 — Test reconstruction of shifted Gaussian emissivity function (contour plot).

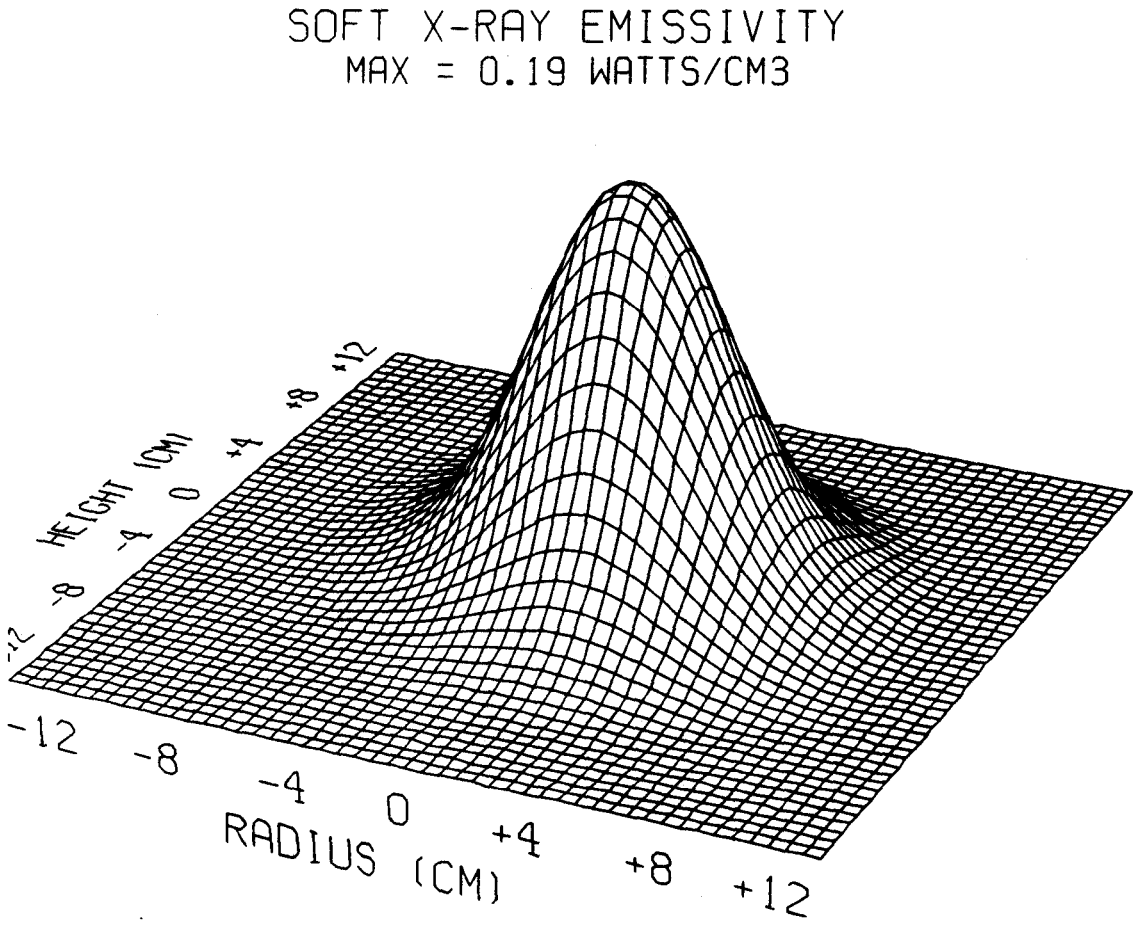

Figure 27 — Test reconstruction of shifted Gaussian emissivity function (3-D plot).

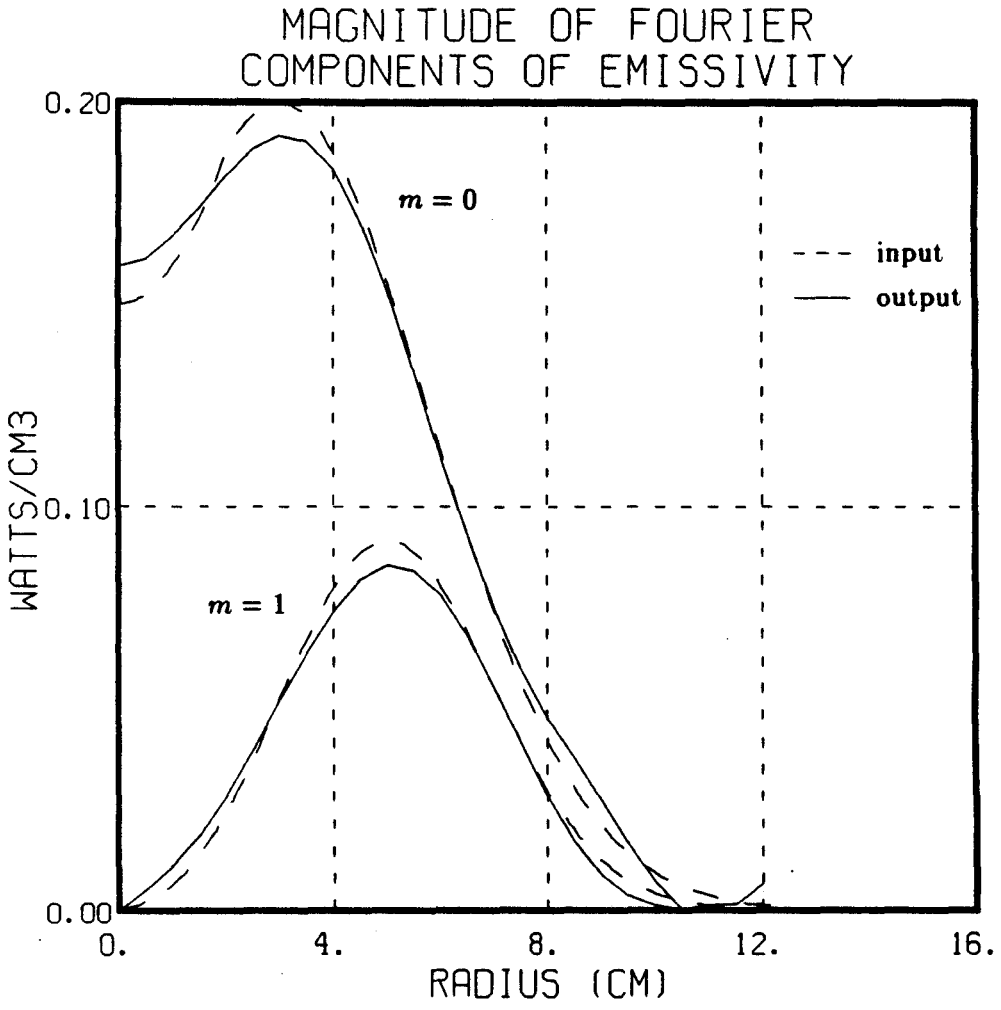

Figure 28 — Test reconstruction of an $m = 1$ island structure (Fourier components). A "hollow" $m = 0$ profile is required in order to obtain an island structure.

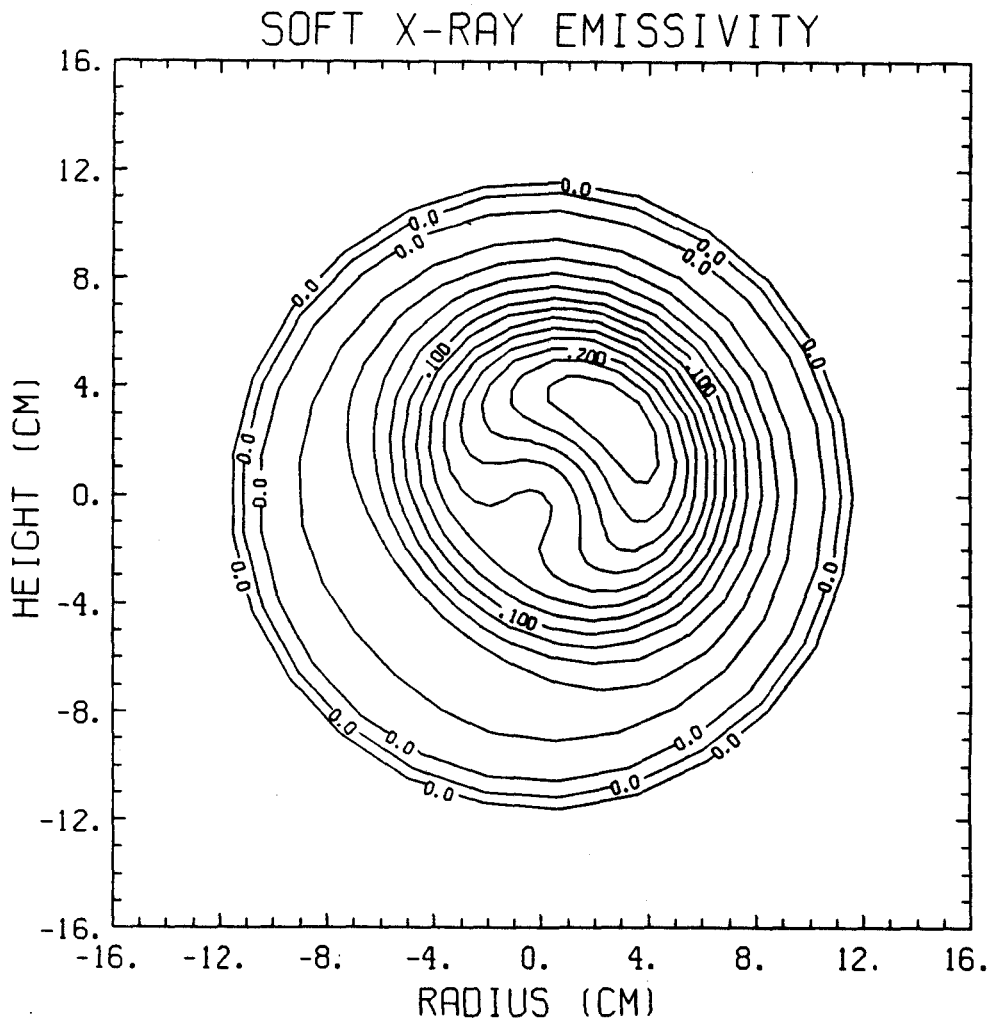

Figure 29 — Test reconstruction of an $m = 1$ island structure (contour plot). The position of the island is reproduced well, as it was specified to be at $\theta = 45°$ in the input function.

the reconstruction matches the input reasonably well, and the plot of contours of constant emissivity shows that the island is clearly discernible. The position and extent of the perturbation are resolved quite satisfactorily. In this simulation, the peak amplitude of the $m = 1$ perturbation is chosen to be about one-half of the peak amplitude of the equilibrium emissivity. A perturbation of this magnitude is required if an island structure is to be observed with the given detector configuration; as will be shown, perturbations of this relative amplitude are observed in pellet-fueled discharges after the pellet injection, when large scale $m = 1$ oscillations are induced.

The restrictions placed on the maximum values of m and l which can be used in order to obtain believable reconstructions are determined by the limited coverage of (p, ϕ) space and by means of an error analysis which attempts to accounts for those deviations in the viewing geometry and detector measurements that degrade the accuracy of the reconstructions. Noise is introduced into the system via random and systematic errors in the simulated data. Random errors, which can represent calibration inaccuracies or some other unpredictable fluctuations in the measurement, are incorporated into the calculations of a reconstruction by simply increasing or decreasing the magnitude of each detector signal. The amount by which the signal is changed is generated from a Gaussian distribution of numbers; one specifies the standard deviation in the errors which are added to or subtracted from each detector signal. The systematic errors are most likely due to the uncertainty in detector positioning. Great care was taken in the machining of the apparatus and in the installation of the arrays on the machine so that all the detectors and their respective apertures would be where the design calls for them to be with respect to the center of the vacuum vessel.

Test cases were thus run for emissivities whose signals had five percent (standard deviation) random error and for which the shift in detector positions is given by a randomly generated offset whose standard deviation is estimated to be 1 mm. It was found that, at these prescribed error levels, using $m = 1$ and $l = 6$ as the maximum values of m and l, one can still obtain believable reconstructions with the

given coverage of (p, ϕ) space. Fig. 30 and Fig. 31 show the result of a reconstruction under these conditions. The input function is the same shifted Gaussian used above and reconstructed in Fig. 25 and Fig. 26. Note that the corrections for the relative calibration factors are already included in the reconstruction. The shift in the detector positions accounts for most of the deviation from the input function, and so the greatest uncertainty in this experiment arises from the differences between the actual detector coordinates and their design values. The errors incurred in this simulation are not found to be too excessive, as the information regarding the position of the emissivity peak and the general shape of the function is still well-preserved (see Fig. 31). In fact, the plot in Fig. 30 does not differ very much at all from the reconstruction in Fig. 25 of the same input function without the inclusion of errors, indicating that error levels comparable to the ones tested here should not introduce significant deviations between the actual emissivities and the reconstructed ones.

More detailed numerical analysis and testing indicate that this diagnostic can resolve features and perturbations in the emissivity (fairly near the central region of the plasma) which have a spatial extent as small as 1 cm, and that it can detect changes in plasma position of a few millimeters. The resolution degrades somewhat as one goes further out in radius.

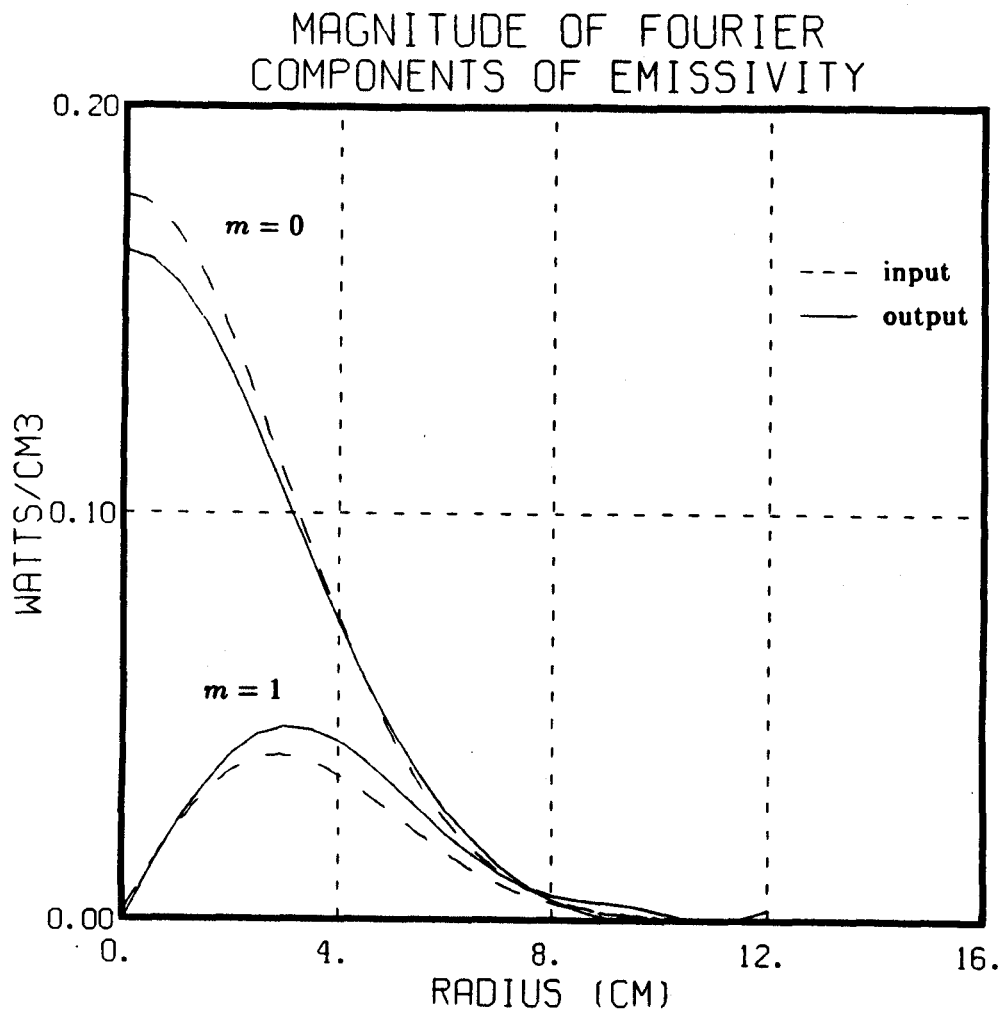

Figure 30 — Test reconstruction of a shifted Gaussian emissivity with errors (Fourier components).

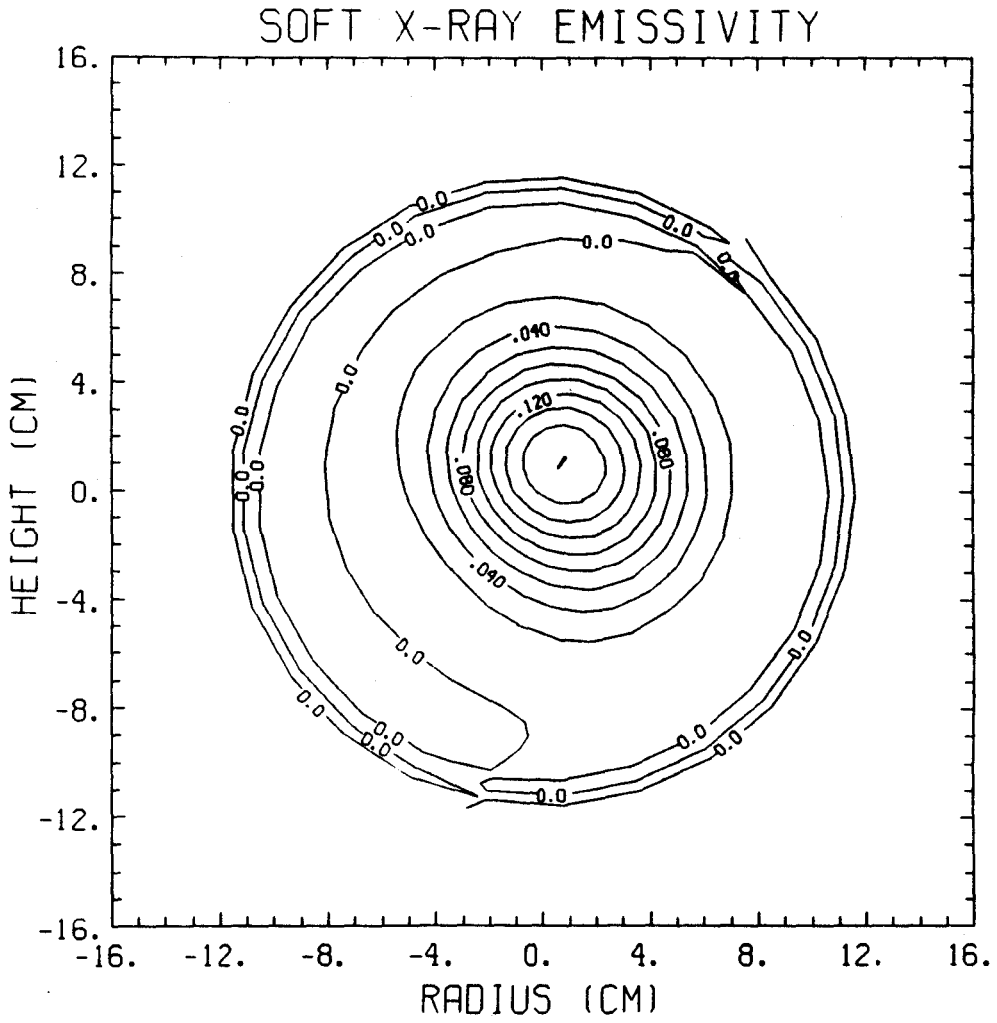

Figure 31 — Test reconstruction of a shifted Gaussian emissivity with errors (contour plot).

IV.2 Reconstruction of an Equilibrium Emissivity

The first example of actual data to be presented is from a typical sawtoothing discharge under equilibrium conditions. Fig. 32 shows the plasma current and line-average electron density traces as a function of time during the shot. Fig. 33 presents a trace of the current signal from one of the photodiodes which views the plasma along a chord that passes near the center of the plasma. This sawtoothing soft x-ray emission is typical of those observed in the hot, central core of the plasma under these discharge parameters. The rising part of each sawtooth corresponds to the fact that the plasma's central temperature is increasing as a result of the ohmic heating input power. The plasma current in the center is also increasing, because plasma resistivity drops with rising temperature. When the current reaches the point at which it makes $q(r = 0) < 1$, an MHD instability sets in and very rapidly "flattens" the temperature, current density, and particle density profiles in the central region. The instability which leads to the flattened profiles is believed to be the $m = 1/n = 1$ resistive tearing mode, in which a magnetic island forms and grows until an internal disruption occurs via magnetic reconnection or turbulence.[36,37] It is this flattening which leads to the sudden drop or "crash" in the sawtooth signals.[22,24]

Obtaining reconstructions of the soft x-ray emissivity just before and just after a sawtooth crash is therefore a case of interest. The trace of the current signal in Fig. 33 is shown on an expanded time scale in Fig. 34, with two points labelled, indicating the times at which reconstructions were made. Fig. 35 has the brightness data obtained from the raw signals (arising from the pre-crash emission) on each detector channel. Fig. 36 shows the brightness data and fitted surface in (p, ϕ) space for the pre-crash reconstruction as an example of a fit which is calculated for real data. A contour plot of the plasma cross-section showing the surfaces of constant emissivity is given in Fig. 37 for the same time. The peak of the emissivity is seen to have both an in-out and up-down displacement relative to the origin (the center of the vacuum vessel; recall that the reconstruction algorithm makes no *a priori* assumption about the position of the plasma center). The in-out shift is about 0.5 cm, whereas the up-down shift is about 1.5 cm (both are in the positive

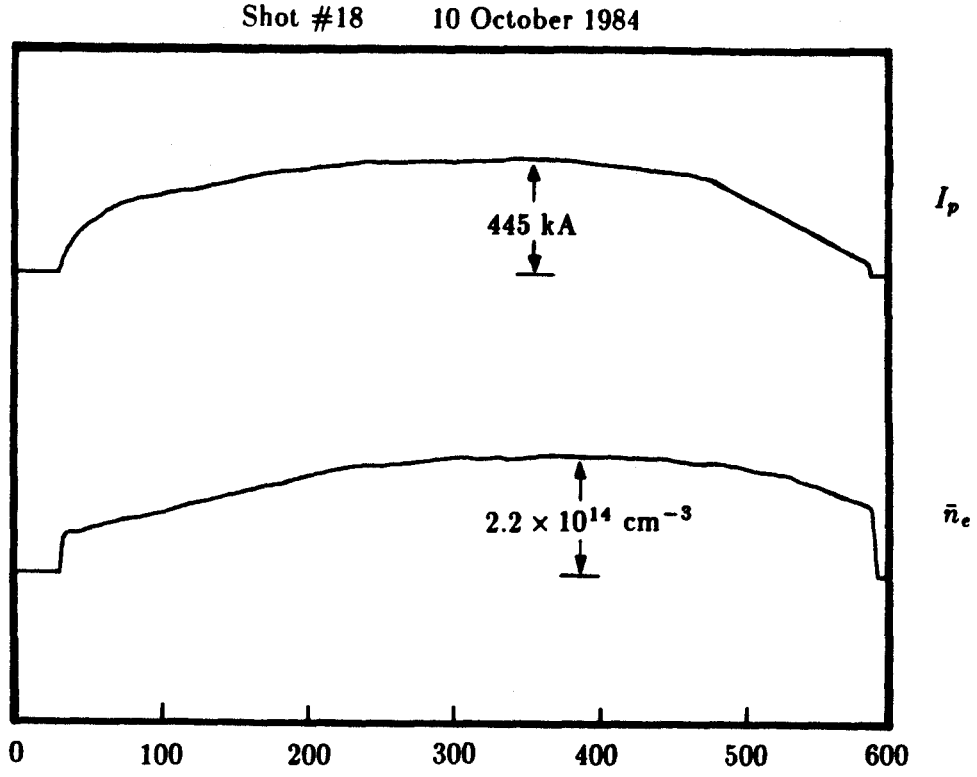

Figure 32 — Plasma current and line-average electron density of discharge under equilibrium conditions.

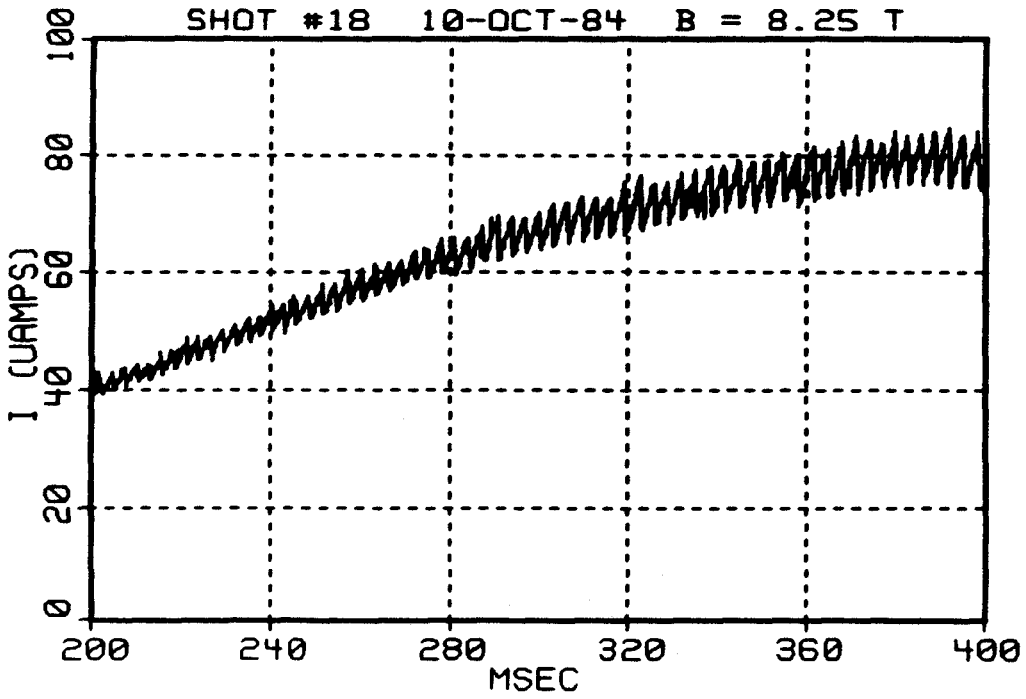

Figure 33 — One of the eighty detector signals from an equilibrium sawtoothing discharge. The impact parameter of this detector's chord of view is $p = 0.9$ cm, so it is viewing almost directly through the center of the plasma.

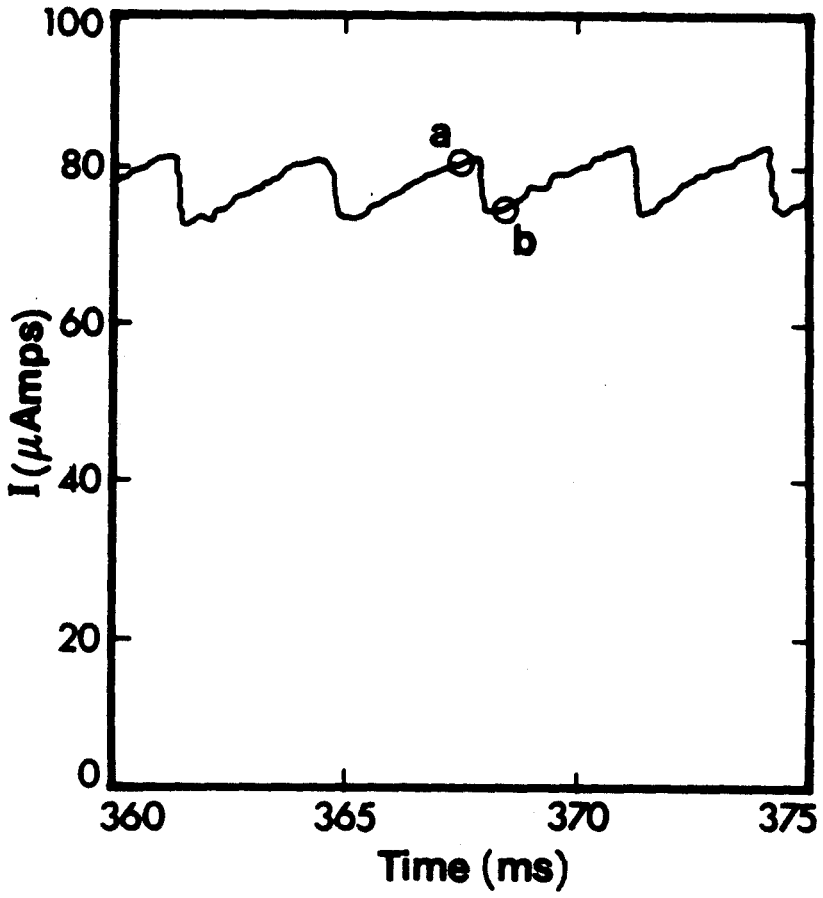

Figure 34 — Detector signal from equilibrium sawtoothing discharge (expanded time scale). Points (a) and (b) indicate the times chosen for the tomographic reconstruction.

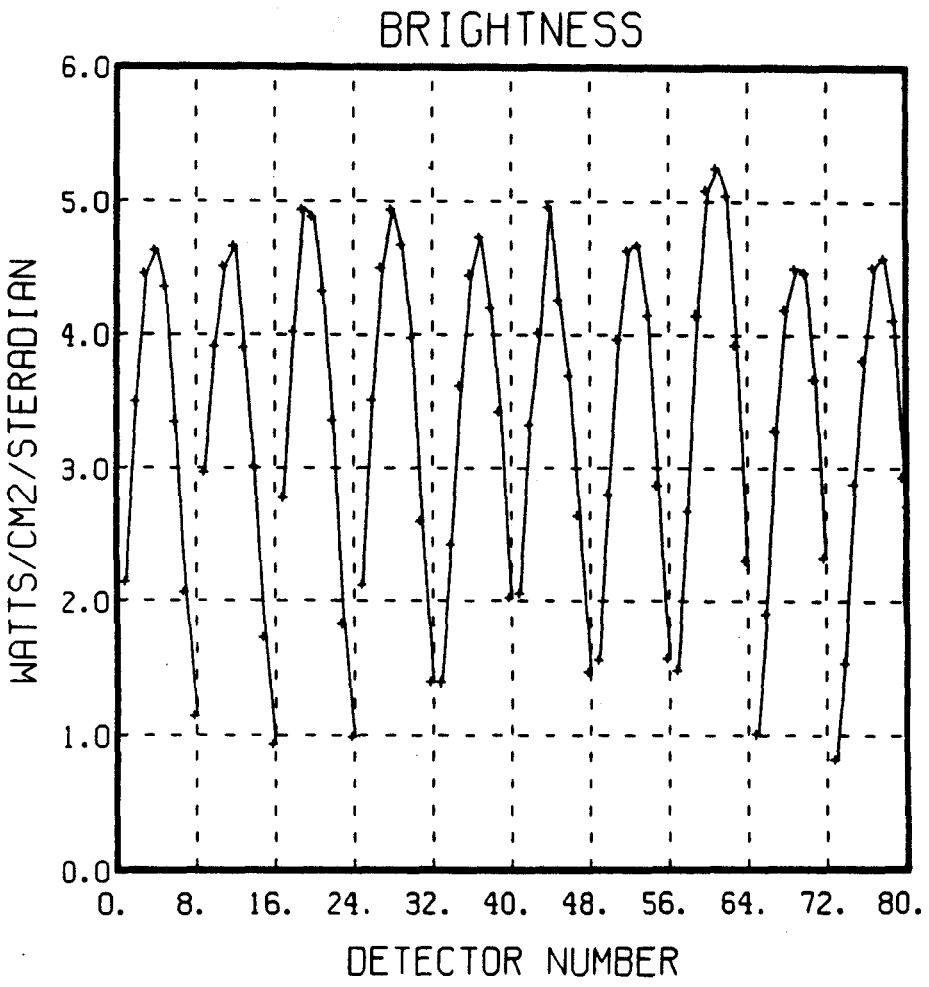

Figure 35 — Brightness data from equilibrium discharge taken at point (a).

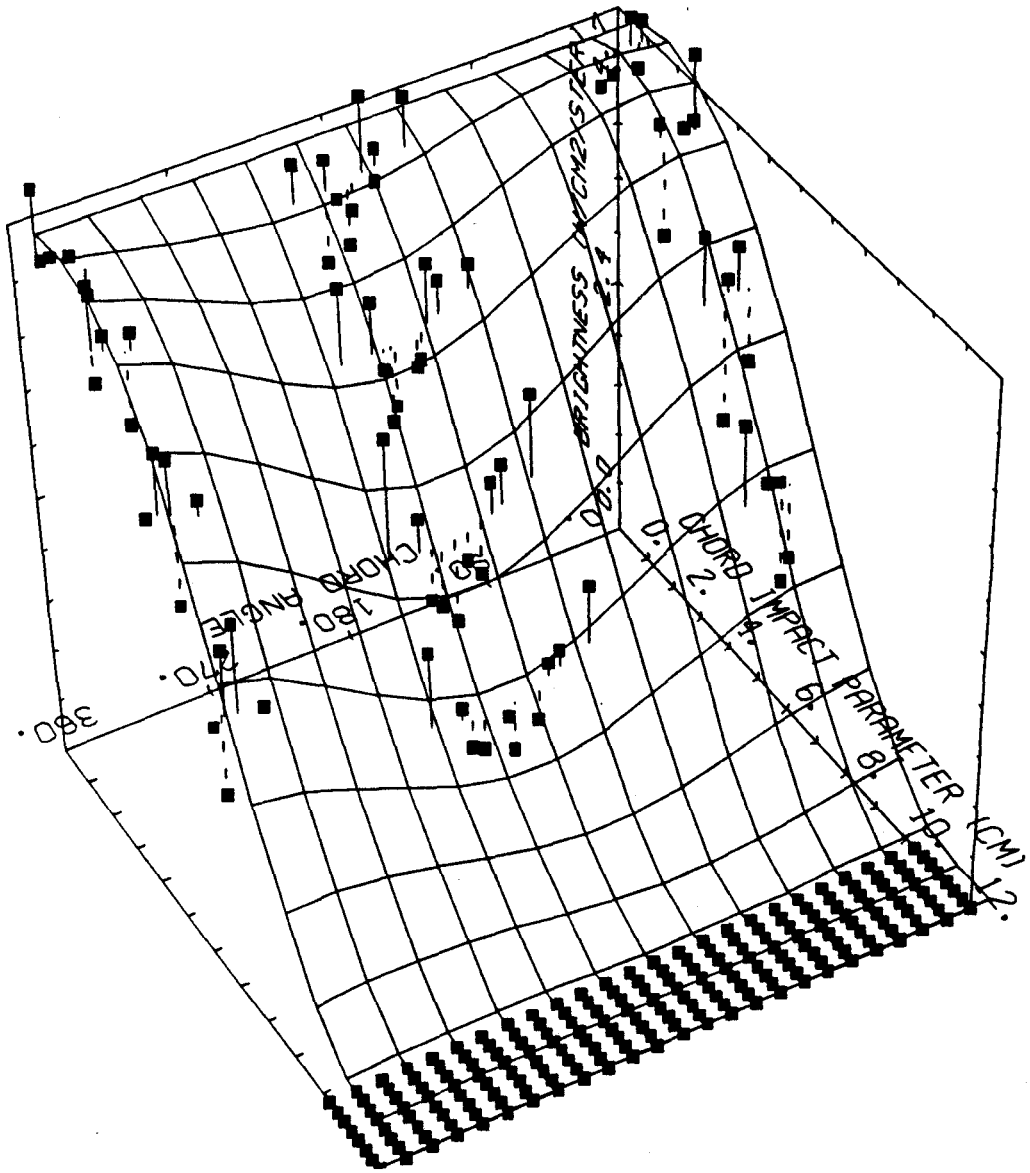

Figure 36 — Brightness data and fitted surface in (p, ϕ) space for equilibrium sawtoothing discharge at point (a). Solid lines from a point to the surface indicate that the point is located above the surface; dashed lines indicate that the point is below the surface.

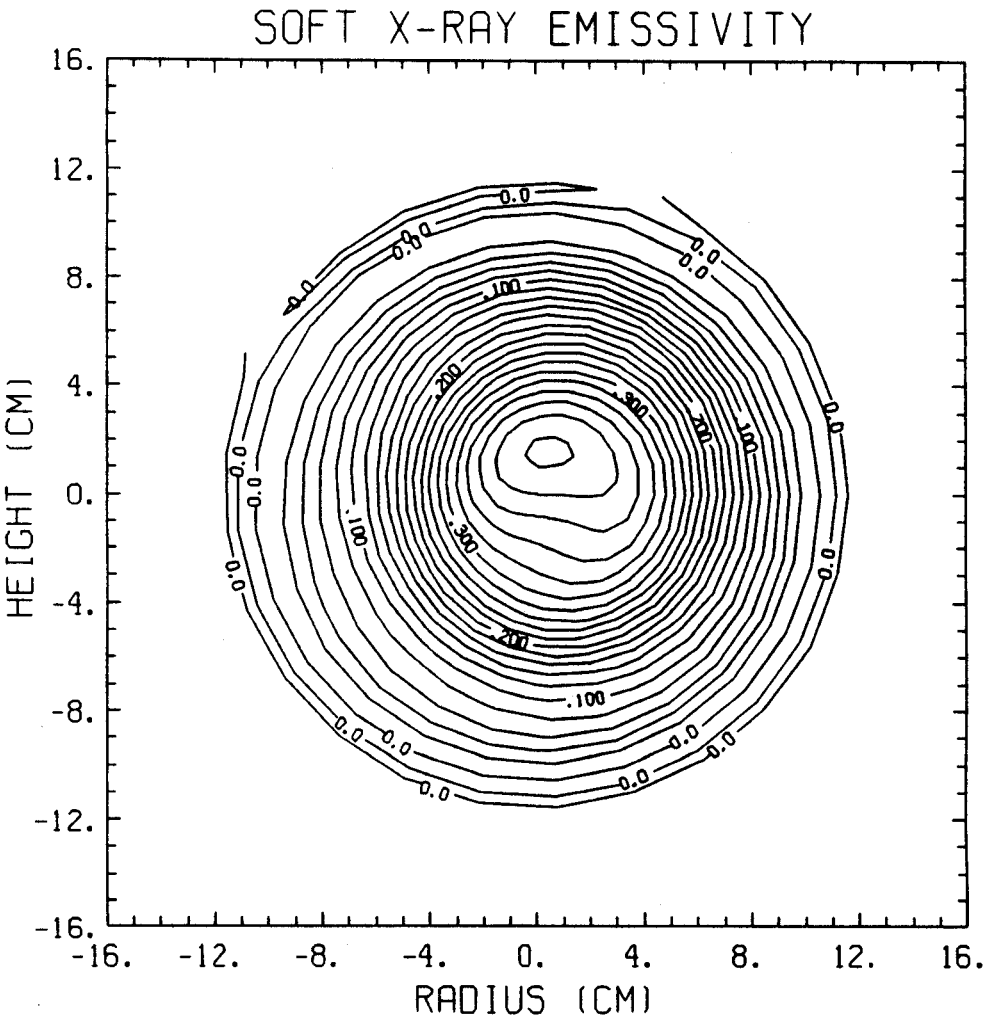

Figure 37 — Reconstruction of equilibrium emissivity (contour plot) at point (a).

direction). The horizontal displacement can be attributed to the Shafranov shift which is expected for the MHD equilibrium in a tokamak. The vertical displacement, however, is a bit more mysterious, especially because it is rather large and therefore within the spatial resolution of the viewing system. Hence, it is not immediately attributable to the uncertainties or limitations of the experimental apparatus.

It might appear that this feature reflects a real property of the emissivity or perhaps an actual physical phenomenon. However, if one computes the centroid of the emissivity (the emissivity's "center of mass") and examines its location rather than the location of the emissivity's maximum value, one finds that the outward shift remains about the same (0.5 to 1 cm), but that the upward shift becomes about 1 or 2 mm, which is quite small and less than the uncertainty of the measurement arising from systematic or random errors. Furthermore, the central portion of the emissivity is fairly flat (much like a Gaussian function) and the exact location of the peak is quite sensitive to any small variations or errors in the signals. The centroid, however, is not so dependent on the variations or errors in the signals and therefore is not shifted by such large amounts. Thus, it is not clear how meaningful the vertical displacement of the peak is.

One explanation as to why the peak of the emissivity is shifted vertically by a fairly large amount is related to the possibility of upward-drifting impurities. These species can contribute significantly to the emission and perhaps even dominate the background bremsstrahlung emission, leading to a biasing of the emissivity values in the direction of the impurity drift. One can only speculate, however, about what mechanism(s) would bring about such an upward drift in the impurity distribution. Another possible explanation is that the absence of views from the side results in a lack of information about up-down motion which, because of any unduly large errors or uncertainties in detector positioning, might cause the reconstruction algorithm to produce emissivities whose peak values are shifted vertically by an inordinate amount. However, a considerable effort was made to insure that the detectors were correctly positioned and to minimize the uncertainties in their location, so it is not likely that this explanation accounts for the observed shift.

The next set of figures illustrate the change with takes place in the emissivity after the sawtooth crash. Fig. 38 is a plot of the magnitude of the $m = 0$ and $m = 1$ Fourier components as a function of radius for the pre-crash and post-crash reconstructions. The flattening of the $m = 0$ profile in the central region and its broadening in the outer regions is readily resolvable and provides a nice picture of what happens to the plasma at a sawtooth crash. The $m = 1$ components, which also change somewhat because of the crash, are present due to the fact that the plasma equilibrium has a Shafranov shift and not because there is an $m = 1/n = 1$ instability.

Fig. 39 shows three-dimensional plots of the emissivity before and after the sawtooth crash. One can observe a slight hollowing in the central portion of the post-crash emissivity; however, it should be recalled that only a finite number of harmonics are used in the reconstruction, and thus there is a residual ripple noise which is of the order of five percent (as discussed in the previous section). Because the hollowing is so small, then, it may not be real. The last figure in the sequence for this shot is Fig. 40. In it, the two three-dimensional plots are superimposed. The portions of the graphs which intersect are seen as a white "ring" in the top half of the plot; this feature physically represents the inversion radius of the sawtooth crash, which should be indicative of where the $q = 1$ surface is.

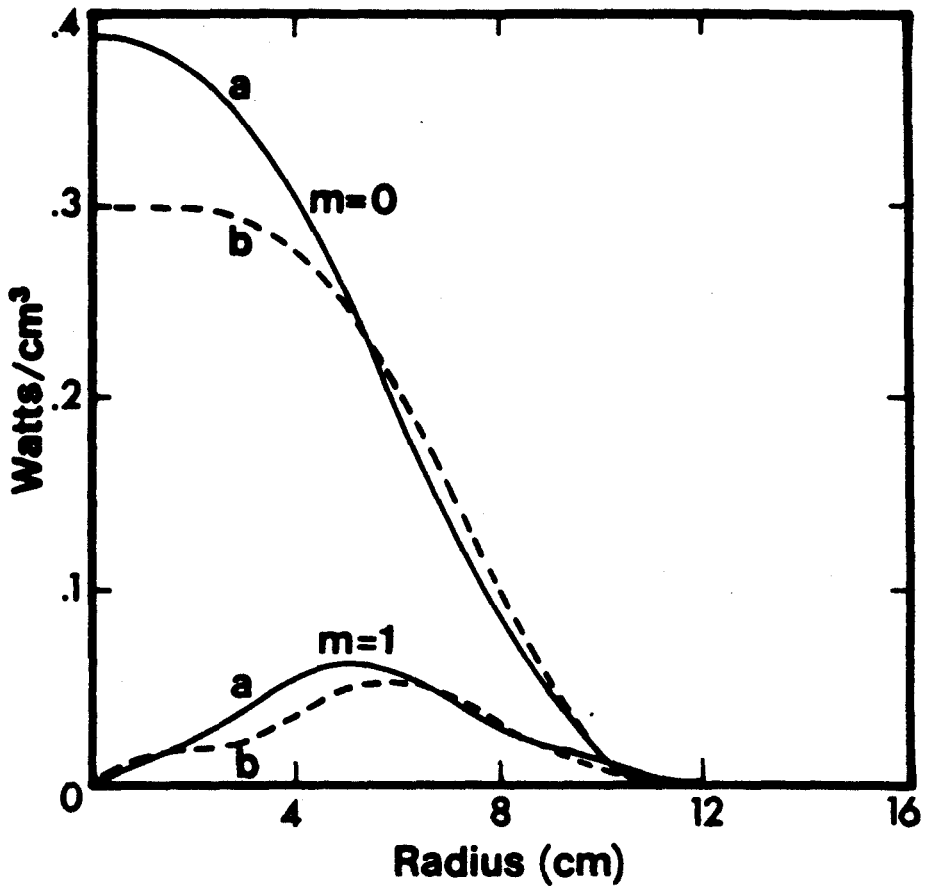

Figure 38 — Reconstruction of equilibrium emissivity before (point (a)) and after (point (b)) the sawtooth crash (Fourier components).

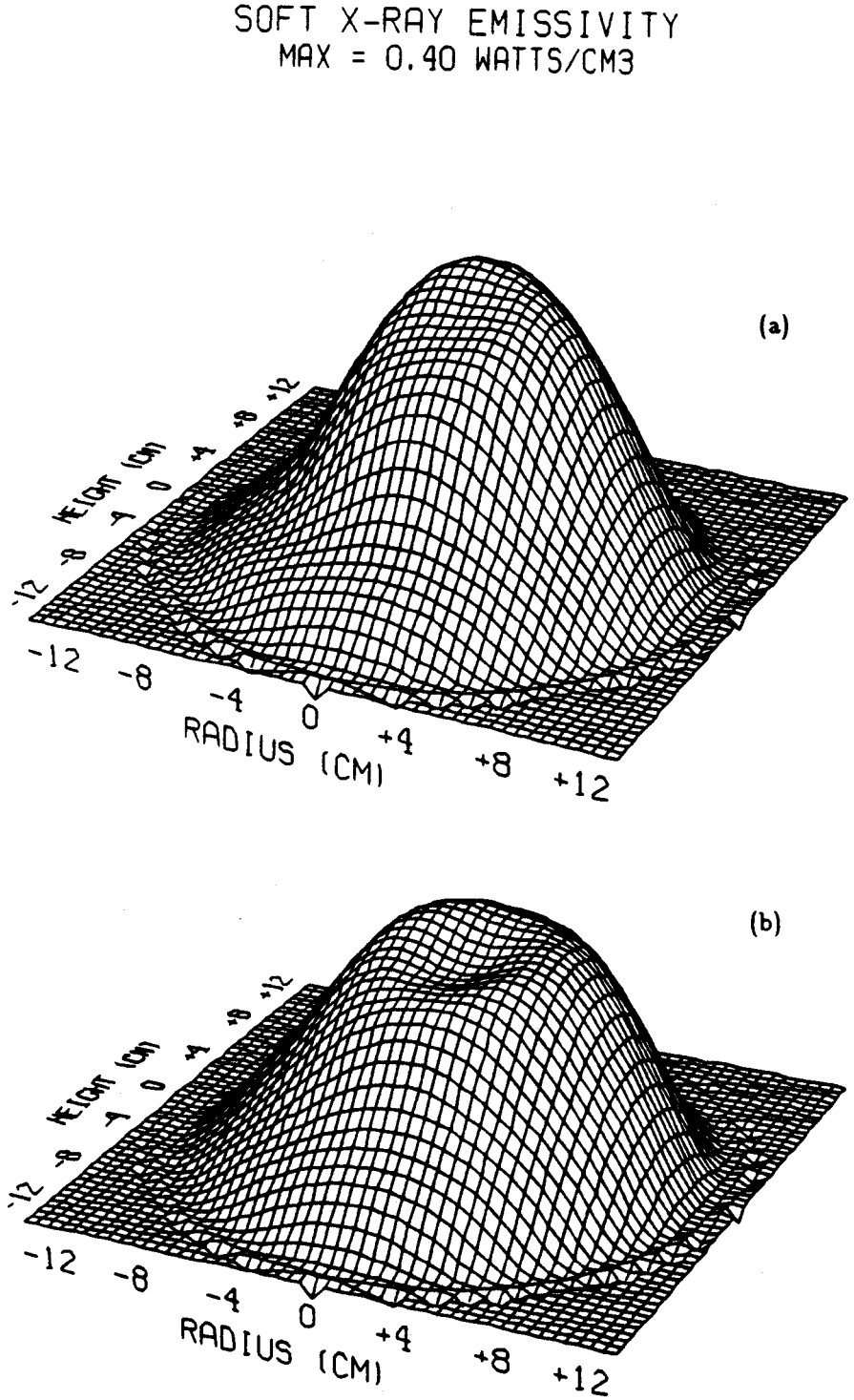

Figure 39 — Reconstruction of equilibrium emissivity before (point (a)) and after (point (b)) the sawtooth crash (3-D plots).

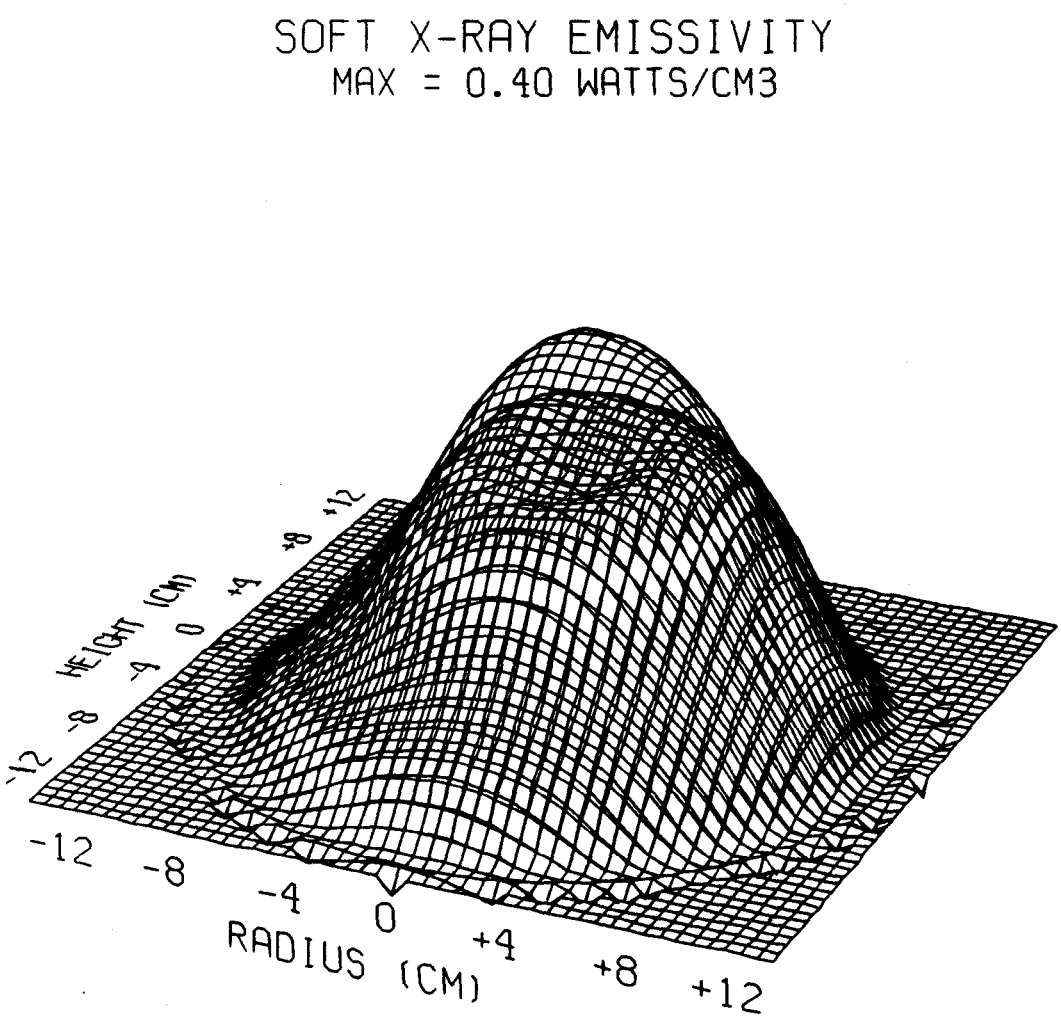

Figure 40 — Overlay of pre-crash and post-crash 3-D plots of equilibrium emissivity.

IV.3 "Giant Sawteeth" after Pellet Injection

Experiments have been performed on Alcator C in which pellets of frozen hydrogen or deuterium are injected into the plasma at high velocities (almost 10^5 cm/sec).[4] The purpose of these efforts is to study pellet injection as an alternative to the standard method of fueling fusion plasmas, which is by the gas puffing of neutral atoms at the plasma edge. Because of the considerable perturbation in the plasma density and temperature caused by pellet injection, interesting MHD activity is induced. One phenomenon which is observed is the occurrence of "giant sawteeth," which are similar to ordinary sawteeth, such as those analyzed in the previous section, but larger in amplitude and exhibiting a longer period of oscillation. Their longer period and larger amplitude enable one to resolve the precursor oscillations which take place just before a sawtooth crash. These oscillations are not readily observable in the case of ordinary sawteeth because they are varying too rapidly compared to the data digitization rate and their amplitude is too small. However, the data digitization rate (10 kHz) is fast enough to sample adequately the larger-amplitude precursor oscillations which take place after pellet injection. Because the oscillations are believed to be caused by the $m = 1/n = 1$ resistive tearing mode, it is desirable to study them with tomography. The fact that they can be clearly measured should facilitate the effort to resolve the magnetic island structure which is theoretically present.

Fig. 41 shows traces of the plasma current and line-average density for a shot in which pellet injection took place. The sudden increase in the line-average density as a result of the ionization of the atoms in the pellet is clearly visible. Fig. 42 is a trace of one of the central-viewing detector signals. The sudden drop in soft x-ray emission which takes place at the time of the injection is brought about by the sudden drop in plasma temperature (the pellet particles are initially quite cold). After recovering to a level which is greater than the pre-pellet one, the post-pellet signal exhibits the larger sawteeth, with the precursor oscillations occurring before each crash. An expanded time scale view of two such sawtooth crashes is given in Fig. 43, and the time frame during which six tomographic reconstructions of one

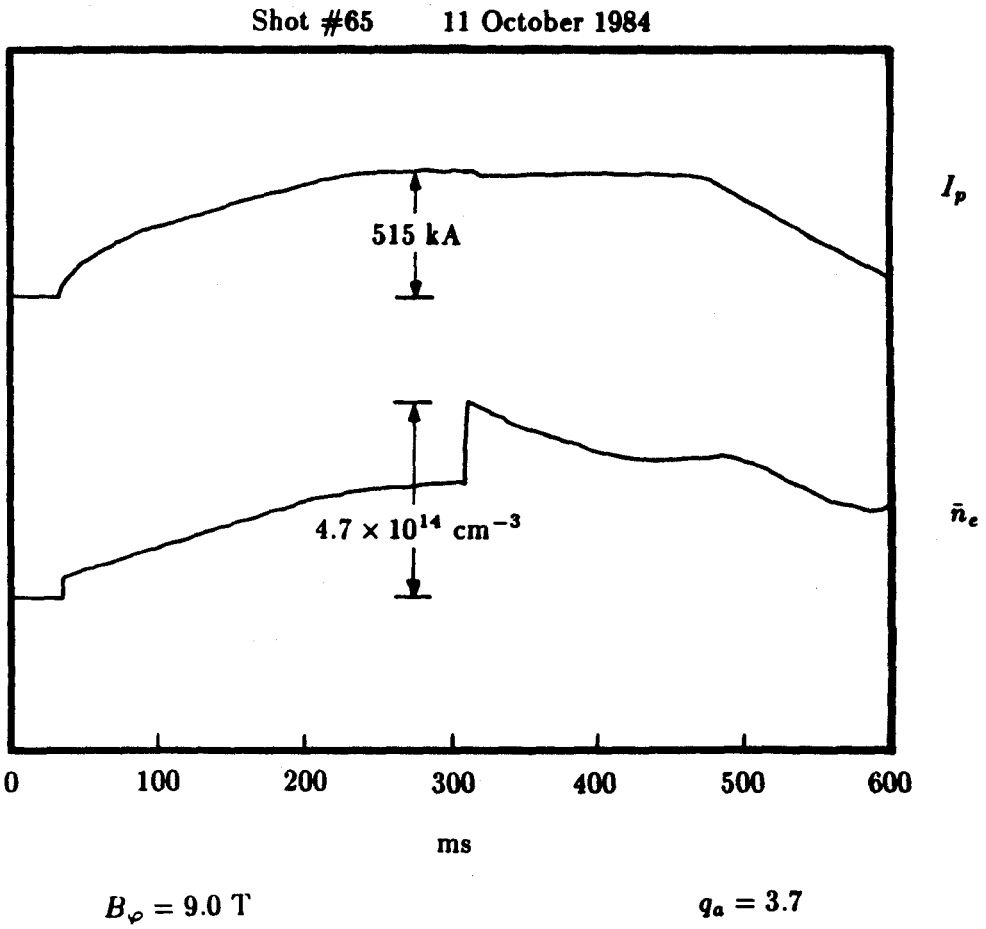

Figure 41 — Plasma current and line-average electron density of pellet-fueled discharge with giant sawteeth.

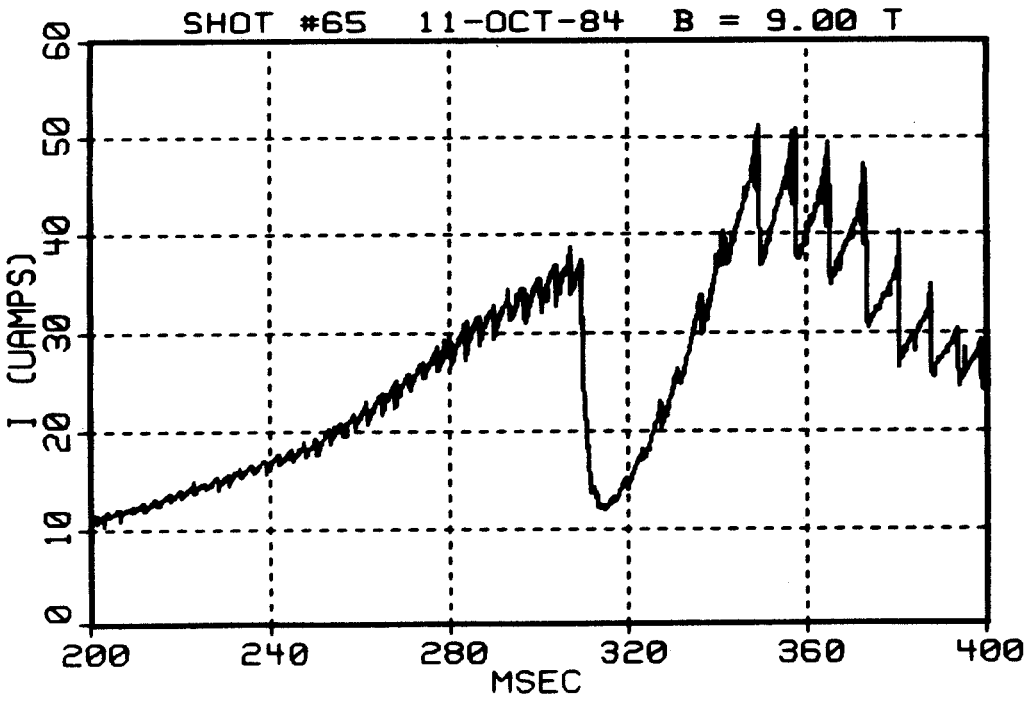

Figure 42 — Detector signal from giant-sawtoothing discharge. The impact parameter of this detector's chord of view is $p = 2.8$ cm.

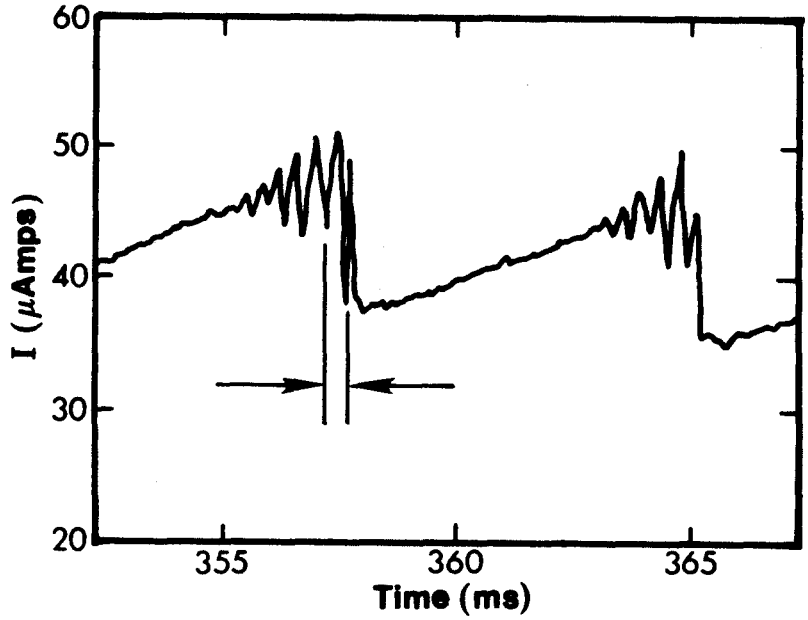

Figure 43 — Detector signal from giant-sawtoothing discharge (expanded time scale). The cycle during which the tomographic reconstructions are performed is indicated.

cycle of the oscillating emissivity were performed is indicated. Contour plots of the six reconstructions from that cycle are shown in Fig. 44; each successive one is separated by a time interval of 100 μs. A perturbation to the nearly circular equilibrium can be observed as one follows the peak of the emissivity from frame to frame. In frames (c) and (e) of Fig. 44, a flattened region near the $q = 1$ surface can be seen. It could conceivably be the center of a magnetic island. However, this feature is not present in the other frames, and the reason for this is not apparent. It is possible that the perturbation changes shape as it rotates from the high magnetic field region to the low magnetic field region. These reconstructions represent the best example, in all the data which were taken, of what appears to be an $m = 1$ island structure.

The spatial viewing resolution of the system is such that it can easily image perturbations of the extent of the one observed in this case (refer to the discussion in Sec. III.1 regarding the coverage of each detector's solid viewing angle, and the discussion in Sec. IV.1 in which the simulation of an $m = 1$ island perturbation is described). Hence, the reconstruction of the island in this sequence of frames is a believable one.

The perturbation is rotating in the electron diamagnetic direction, but this rotation is not exactly sinusoidal, as the motion of the peak in the emissivity is not uniform from one frame to the next. The rotation of the perturbation accounts for the precursor oscillations in the soft x-ray signals, as the detectors see alternatively hotter and colder parts of the plasma pass through their respective fields of view. If the perturbation is indeed a magnetic island, then its rotation is believed to be brought about either by ω_* diamagnetic effects (the so-called drift tearing mode[38]), or by radial electric fields which give rise to an $\mathbf{E} \times \mathbf{B}$ drift,[39] or by a combination of the two.

In Fig. 45, plots of the magnitude of the $m = 0$ and $m = 1$ Fourier components are given for the six reconstructions. One can see a rather dramatic change in the shape of the $m = 0$ profile in going from frame (b) to frame (c). The peak value drops noticeably, and the profile becomes hollow. Because the location of the

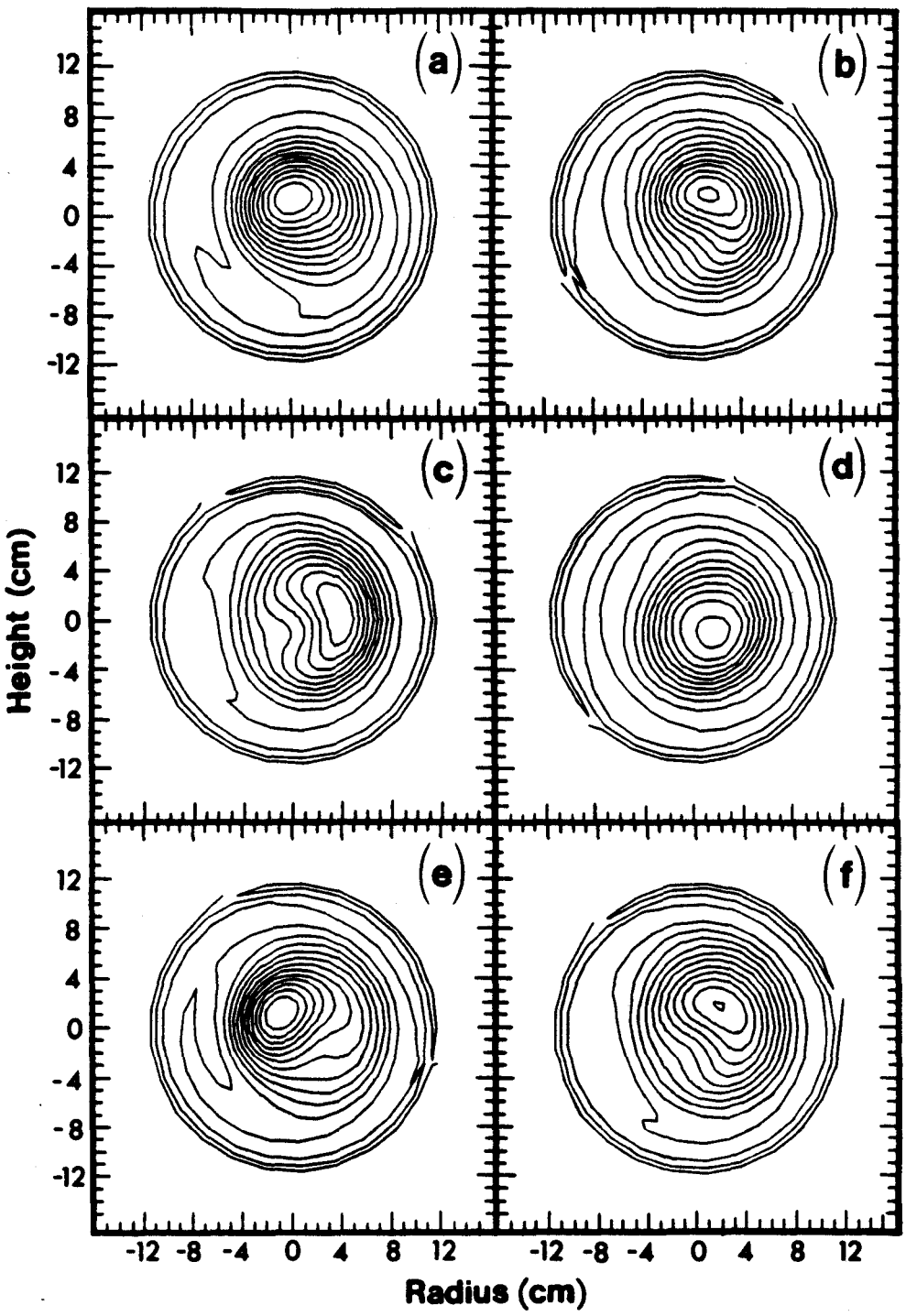

Figure 44 — Reconstruction of a sawtooth precursor oscillation during a giant-sawtoothing discharge (contour plots). Each successive frame is 100 μs apart in time (t = 357.2 ms to t = 357.7 ms).

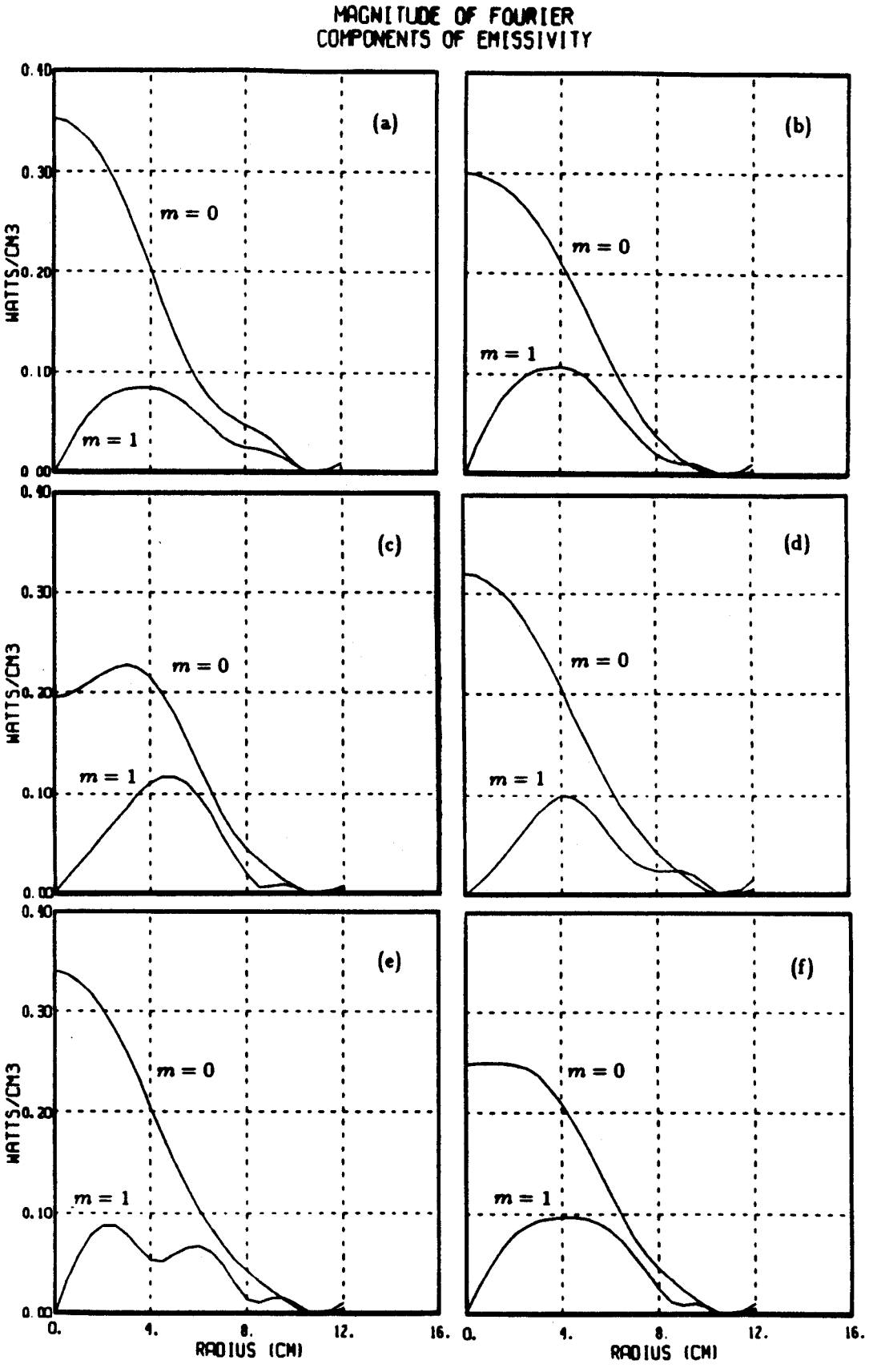

Figure 45 — Reconstruction of giant-sawtoothing emissivity (Fourier components).

$m = 0$ peak is shifted outward and moves closer to the location of the peak of the $m = 1$ component, the sum of the two leads to the structure which is suggestive of a magnetic island. The peak value of the $m = 0$ profile then increases again in the span of 100 μs, as can be seen in frames (d) and (e), with another noticeable drop taking place in the last frame at the end of the oscillation cycle. After that frame, the sawtooth crash occurs, and the cycle begins to repeat itself again with the sawtooth rise. Three-dimensional plots of the emissivities for this cycle are displayed in Fig. 46.

Another point of interest in the study of a discharge such as this one is the analysis of the soft x-ray emissivity enhancement factor. As discussed in Sec. II.1.2, one can obtain a measure of the extent to which impurities contribute to the overall emissivity by comparing the reconstructed emissivity to the absolute minimum emissivity which one would measure if there were no impurities in the plasma. In other words, one can take the ratio of the measured emissivity to the absolute minimum emissivity which would be observed at the given density and temperature. The radiation in the case of the minimum emissivity is all from hydrogen bremsstrahlung and recombination. The enhancement factor is thus defined as

$$R(r,\theta,t) \equiv \frac{\mathcal{E}(r,\theta,t)}{n_e^2(r,t)\, F_H\left[T_e(r,t)\right]} \tag{47}$$

where $\mathcal{E}(r,\theta,t)$ is the reconstructed emissivity, $n_e(r,t)$ is the plasma electron density, and $F_H\left[T_e(r,t)\right]$ is the so-called filtered power density for a hydrogen plasma (normalized to n_e^2) which describes how much of the bremsstrahlung and recombination radiation from a pure hydrogen plasma ($Z_{eff} = 1$) makes it through a given filter (in this case, the beryllium aperture windows and the layer of silicon on the detectors). This function can be computed by combining the spectral distribution of the power radiated via bremsstrahlung and recombination at a given temperature (see Fig. 3 for the bremsstrahlung power spectral distribution), with the filtering/transmitting properties (mass attenuation coefficients) of the beryllium windows and the silicon in the detectors (this information is available in tabulated form as a function of wavelength). Knowing the actual density and temperature

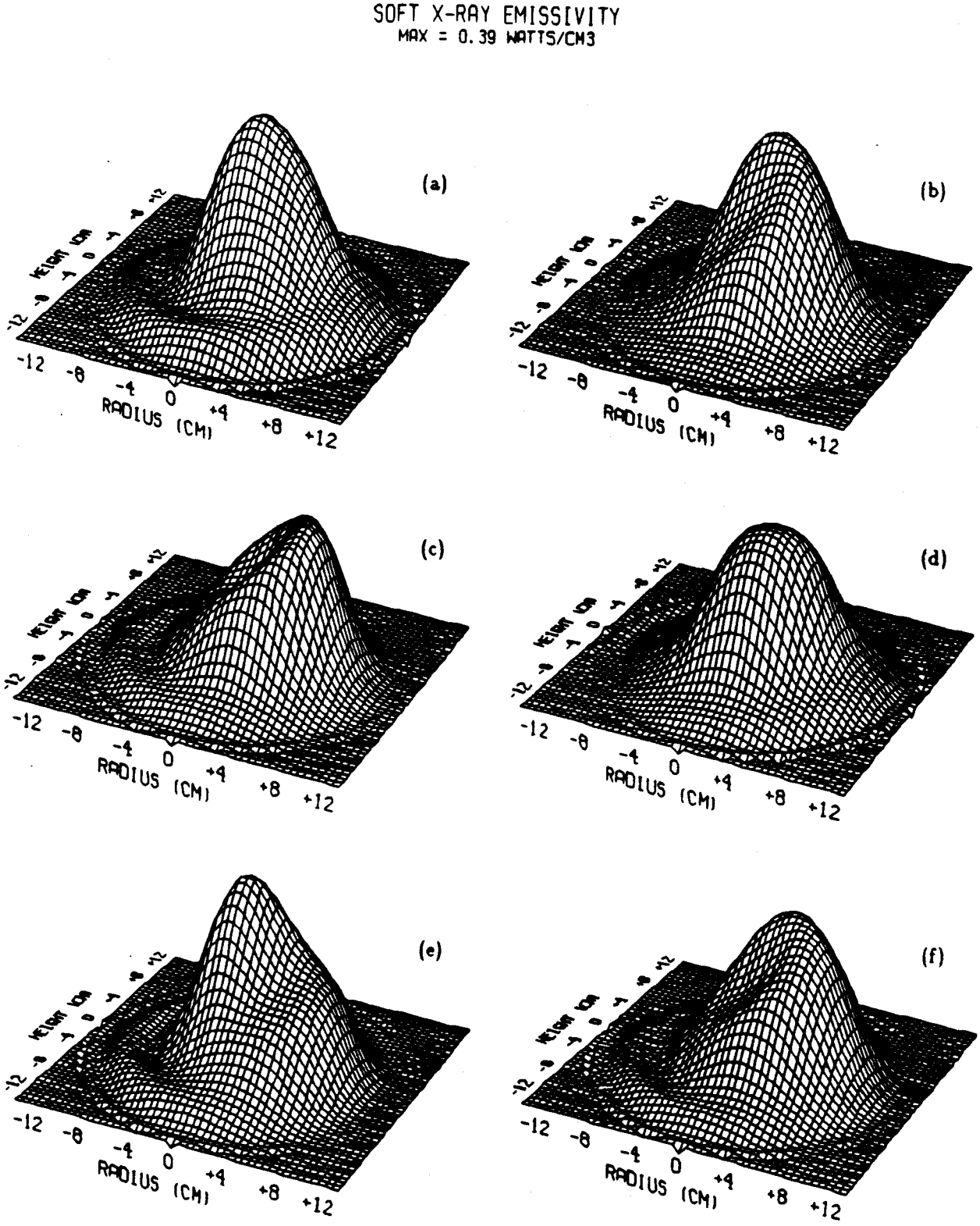

Figure 46 — Reconstruction of giant-sawtoothing emissivity (3-D plots).

distribution in the plasma (these are measured), one can then calculate what the emissivity would be if $Z_{eff} = 1$, in which case $R \rightarrow 1$.

The enhancement factor analysis presented here is rather cursory and primarily intended to show the potential utility of this diagnostic in terms of studying the behavior and effects of impurities in Alcator C plasmas. Fig. 47 is a plot of the enhancement factor at the point of maximum emissivity (which is usually the point of maximum density and temperature and at or near the center of the plasma chamber) for several points in time during the same shot studied above. Of particular interest is what happens just after pellet injection and just before and after a giant sawtooth crash. The enhancement factor increases by about a factor of three quite rapidly as a result of the pellet injection because of the sudden drop in T_e, which lowers F_H, and the fact that impurity radiation becomes the dominant radiation mechanism at these lowered temperatures. However, as the density begins to build up and the plasma reheats, the enhancement factor drops to levels which are lower than those observed before pellet injection. Then, when the giant sawteeth occur, one finds that the enhancement factor undergoes noticeable and rather sudden drops after each sawtooth crash, coming back up to a level comparable to the pre-crash value. This behavior is in qualitative agreement with the one observed in other Alcator C experiments[40] in which the central enhancement factor was studied as a function of time for pellet-fueled discharges with giant sawteeth. The values of R found here, however, are somewhat larger than the ones encountered in the previous study described in Ref. 40. For example, the maximum central enhancement factor observed in this shot is $R = 29.11$ (at $t = 315$ ms, just after pellet injection) *vs.* $R = 8.25$ in the other experiment. The minimum values obtained are $R = 3.35$ (at $t = 374$ ms, just after a giant sawtooth crash) in this experiment *vs.* $R = 1.30$ in the previous one.

The fact that R decreases after each giant sawtooth crash may be indicative of a reduction or expulsion of impurities from the central core of the plasma. In order to investigate this point further, one can take the measured density and temperature profiles and determine, from the reconstructed emissivities, what the radial profile of

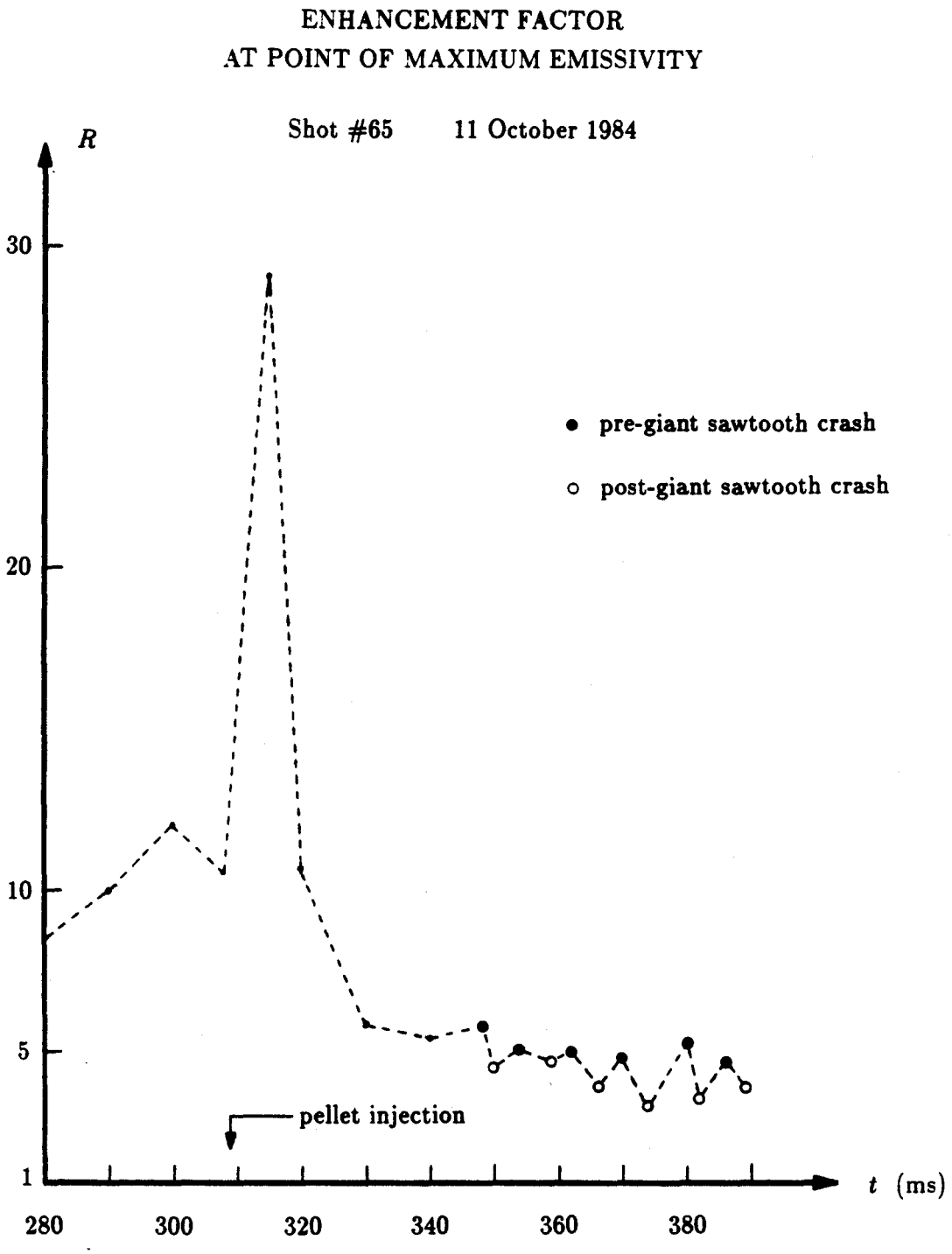

Figure 47 — Enhancement factor at point of maximum emissivity, density, and temperature as a function of time. The giant sawtoothing activity starts at about $t = 345$ ms.

the enhancement factor is along the toroidal midplane, for instance. Plotting these at different times may indicate what happens to the distribution of impurities. In Fig. 48, four such profiles are shown. The first two (at $t = 308$ ms and $t = 315$ ms) show the difference between the pre- and post-pellet injection profiles. The other two are taken before and after a giant sawtooth crash. The rather large increase in the values of R which occurs after pellet injection is consistent with the observations made in previous experiments.[40]

In general, it is not entirely obvious why the enhancement factor at a given time is usually greater on the outer major radius side than on the corresponding inner one. Of course, there is an $m = 1$ component present due to the Shafranov shift, and it is reflected in the location of the point of maximum emissivity and in the temperature and density profiles, both of which are symmetric about that point. It is not clear, however, that the Shafranov shift by itself can account for the rather large asymmetry observed in the enhancement factor profiles.

After a giant sawtooth crash (the profile at $t = 374$ ms), one can see that the enhancement factor profile becomes rather flat and that its magnitude drops in the central region of the plasma. As one goes beyond the $q = 1$ surface ($r \approx \pm 5$ cm), however, it is found that the values of the enhancement factor are greater after the giant sawtooth crash than before it. Previous work[40] done to model the impurity distribution in the plasma indicates that, before the giant sawtooth crash, there is a highly peaked impurity density profile (consisting of either carbon and/or molybdenum, the dominant light and heavy impurities in Alcator C). After the crash, a significant absolute reduction in the central impurity density (by a factor of about five) is believed to take place. This reduction of impurities may account for the decrease observed in the central values of R, whereas the increase in its outer values may confirm the suspicion that these impurities are expelled from the central region and deposited in the outer region by the redistribution of density which occurs at the giant sawtooth crash.

One can extend the study of the enhancement factor by investigating its behavior across the entire two-dimensional poloidal cross-section of the plasma (with

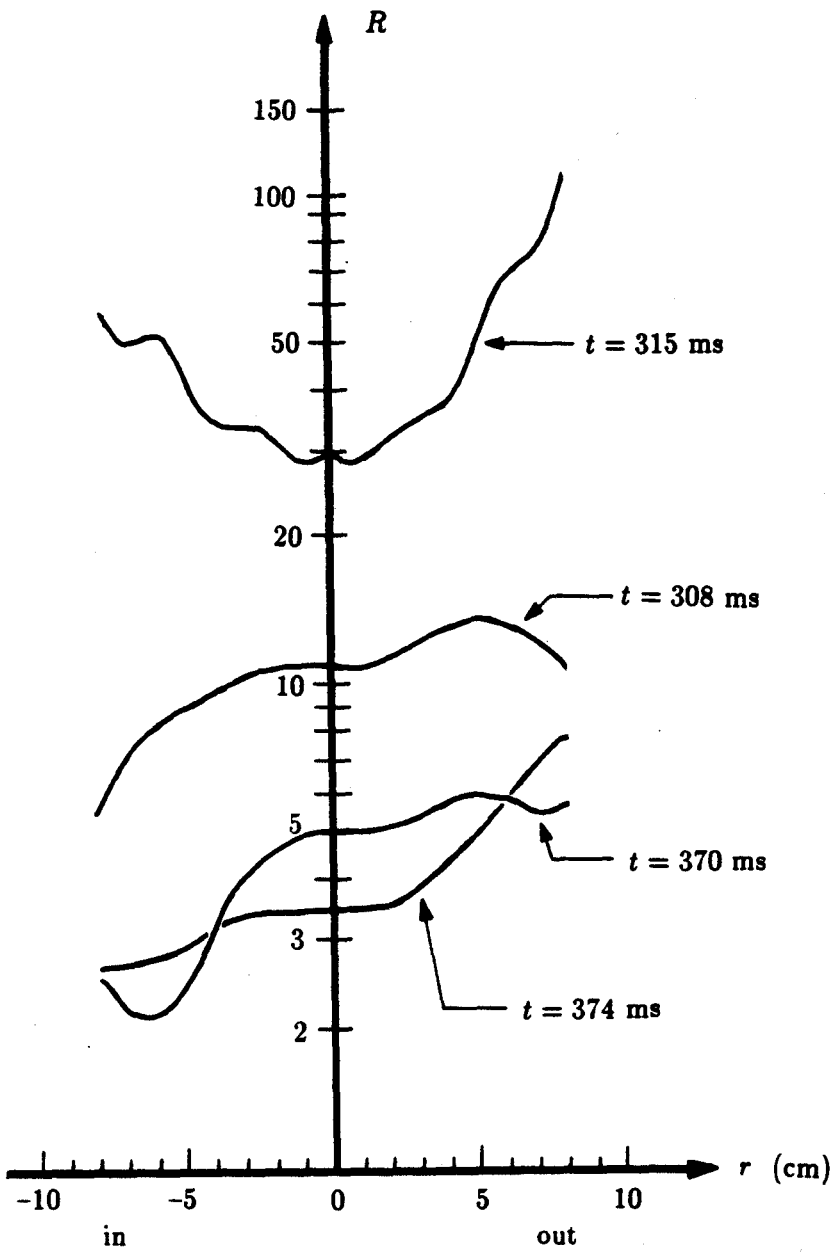

Figure 48 — Radial profiles of the enhancement factor along the toroidal midplane at four different times: 1) Pre-pellet injection (t = 308 ms), 2) Post-pellet injection (t = 315 ms), 3) Pre-giant sawtooth crash (t = 370 ms), and 4) Post-giant sawtooth crash (t = 374 ms).

contour plots similar to the those used in the tomographic reconstructions) and determining how it correlates with overall plasma behavior. In this manner, one may be able to develop models for the impurity distribution and how it changes with or affects the state of the plasma.

IV.4 Non-Sawtoothing Oscillations after Pellet Injection

The last discharge to be shown is from pellet-fueled plasmas which have lower current than the previously studied discharges and do not exhibit sawtoothing behavior. Instead, the plasma simply undergoes large $m = 1$ oscillations after pellet injection, the onset of which takes place well after the plasma has equilibrated. The plasma current and line-average electron density for the shot under investigation are shown in Fig. 49. Fig. 50 is a trace of one of the detector signals, with an expanded time scale view displayed in Fig. 51, indicating the oscillation cycle during which six reconstructions of the soft x-ray emissivity were computed. Analysis of the analog signals before digitization indicates that the 10 kHz sampling rate is sufficiently fast to prevent aliasing, so the signals used here are accurate representations of the actual variation in the soft x-ray emission.

At first glance, it appears that the observed oscillations indicate mode rotation. However, the reconstructions clearly show that this mode *does not* rotate, in contrast to the perturbation analyzed in the last section. In this situation, the instability seems to grow and compress the plasma on the inner major radius side, as can be seen in the contour plots of Fig. 52. Note that the lower current leads to a "skinnier" emissivity, as the size of the hot central region of the plasma is smaller than that of a higher current discharge, which has a larger current channel. The plasma starts out with its normal circular shape and then undergoes the compression on one side. Then, within 100 μs (from frame (e) to frame (f) of Fig. 52), the instability disappears and the plasma returns to the state in which it was at the beginning of the oscillation cycle. The mode reappears afterward as the process repeats itself over and over again, resulting in the oscillations measured in the individual soft x-ray signals from each detector. In Fig. 53, the $m = 0$ and $m = 1$ Fourier components are plotted, and one can see the growth in the amplitude of the $m = 1$ component, accompanied by a decrease in the amplitude of the $m = 0$ component, as the instability develops. The sudden return to the initial state can also be seen quite clearly by noticing the change which occurs in going from frame (e) to frame (f) in the same figure. The last sequence of plots, in Fig. 54, shows the three-dimensional

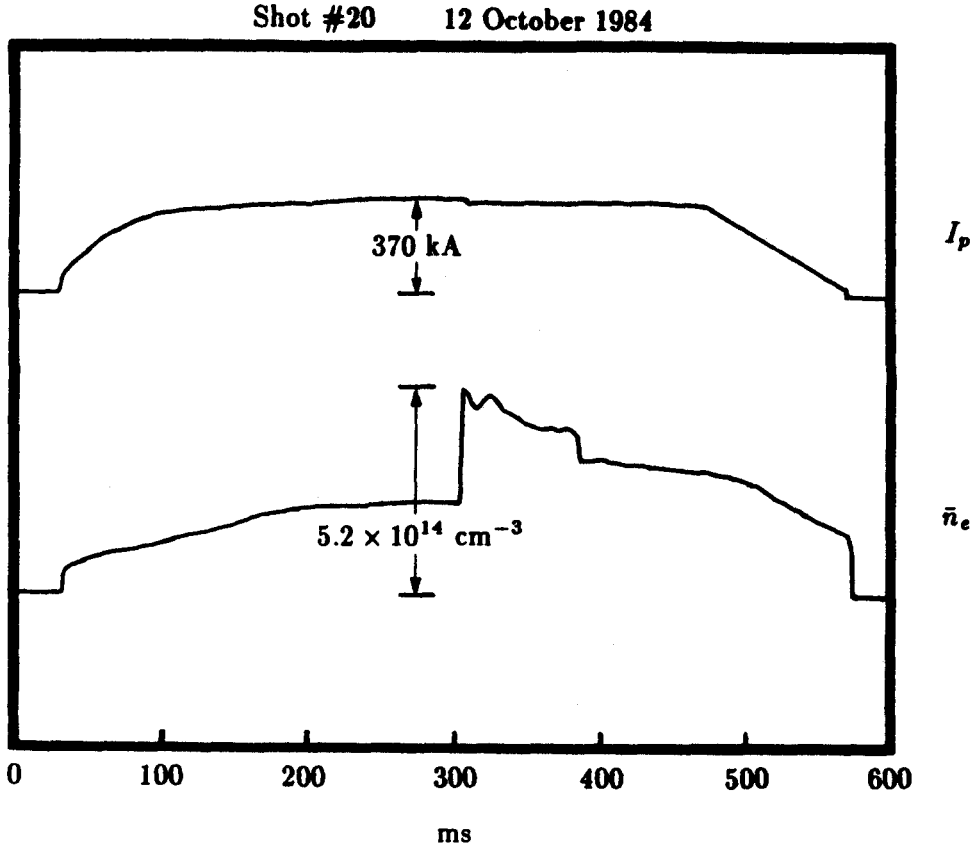

Figure 49 — Plasma current and line-average electron density of a pellet-fueled discharge with non-sawtoothing oscillations.

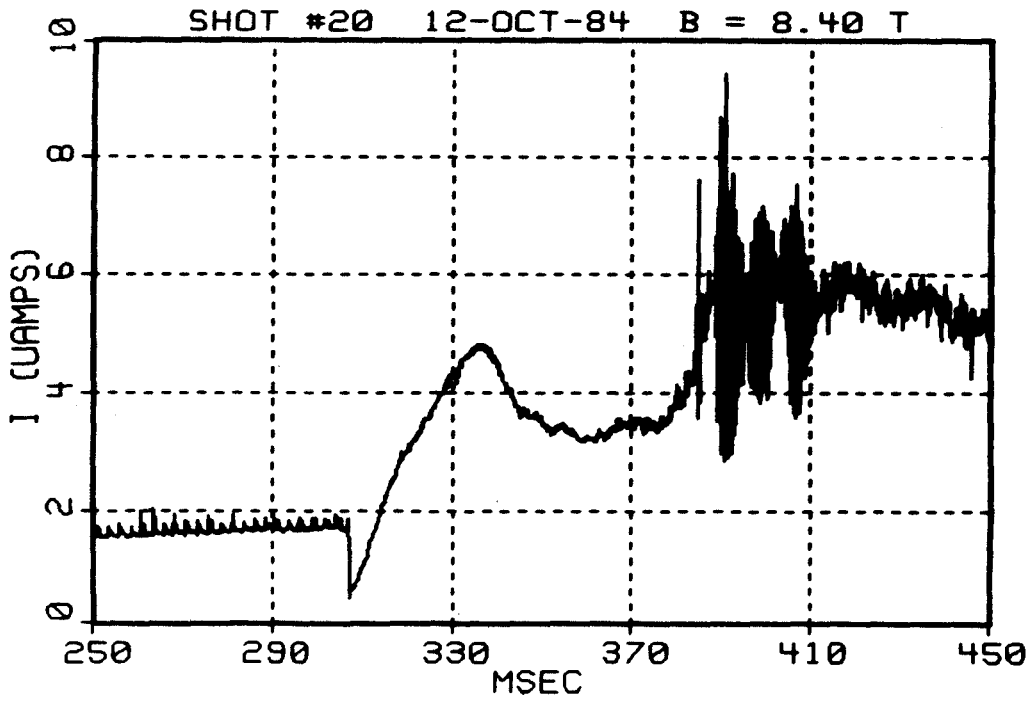

Figure 50 — Detector signal from non-sawtoothing oscillating discharge. The impact parameter of this detector's chord of view is $p = 4.6$ cm.

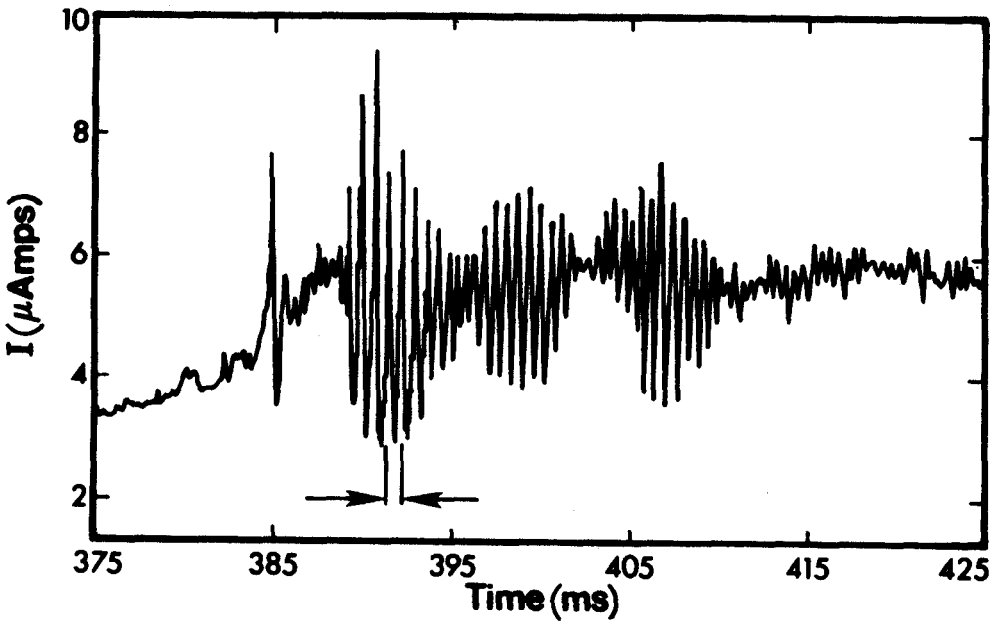

Figure 51 — Detector signal from non-sawtoothing oscillating discharge (expanded time scale). The cycle during which the tomographic reconstructions are performed is indicated.

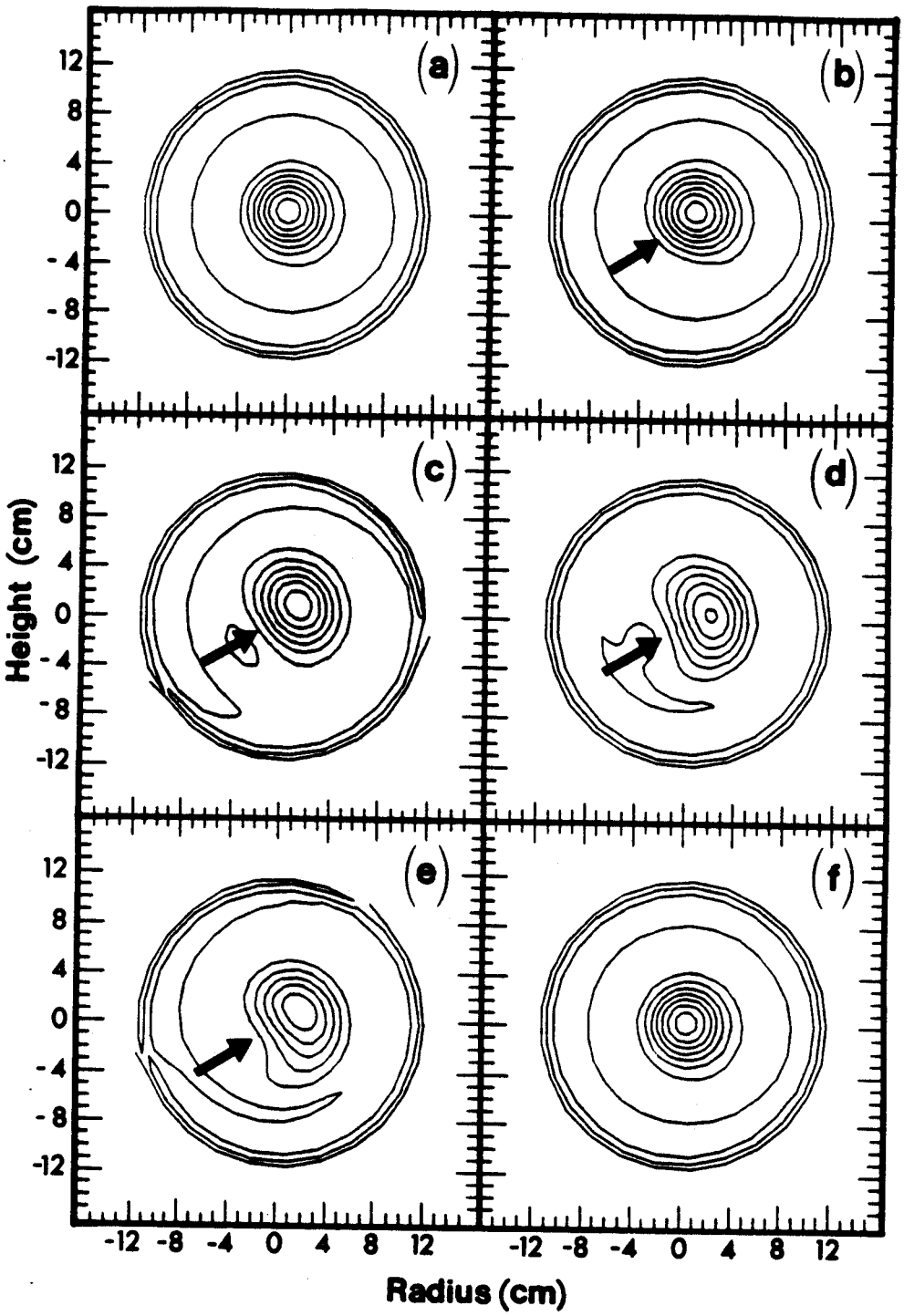

Figure 52 — Reconstruction of non-sawtoothing oscillating emissivity (contour plots). Frames (a), (b), and (c) are at t = 391.7 ms, 391.9 ms, and 392.1 ms, respectively; frames (d), (e), and (f) are at t = 392.2 ms, 392.3 ms, and 392.4 ms, respectively. The arrows indicate the direction in which the plasma is compressed during the non-sawtoothing oscillation.

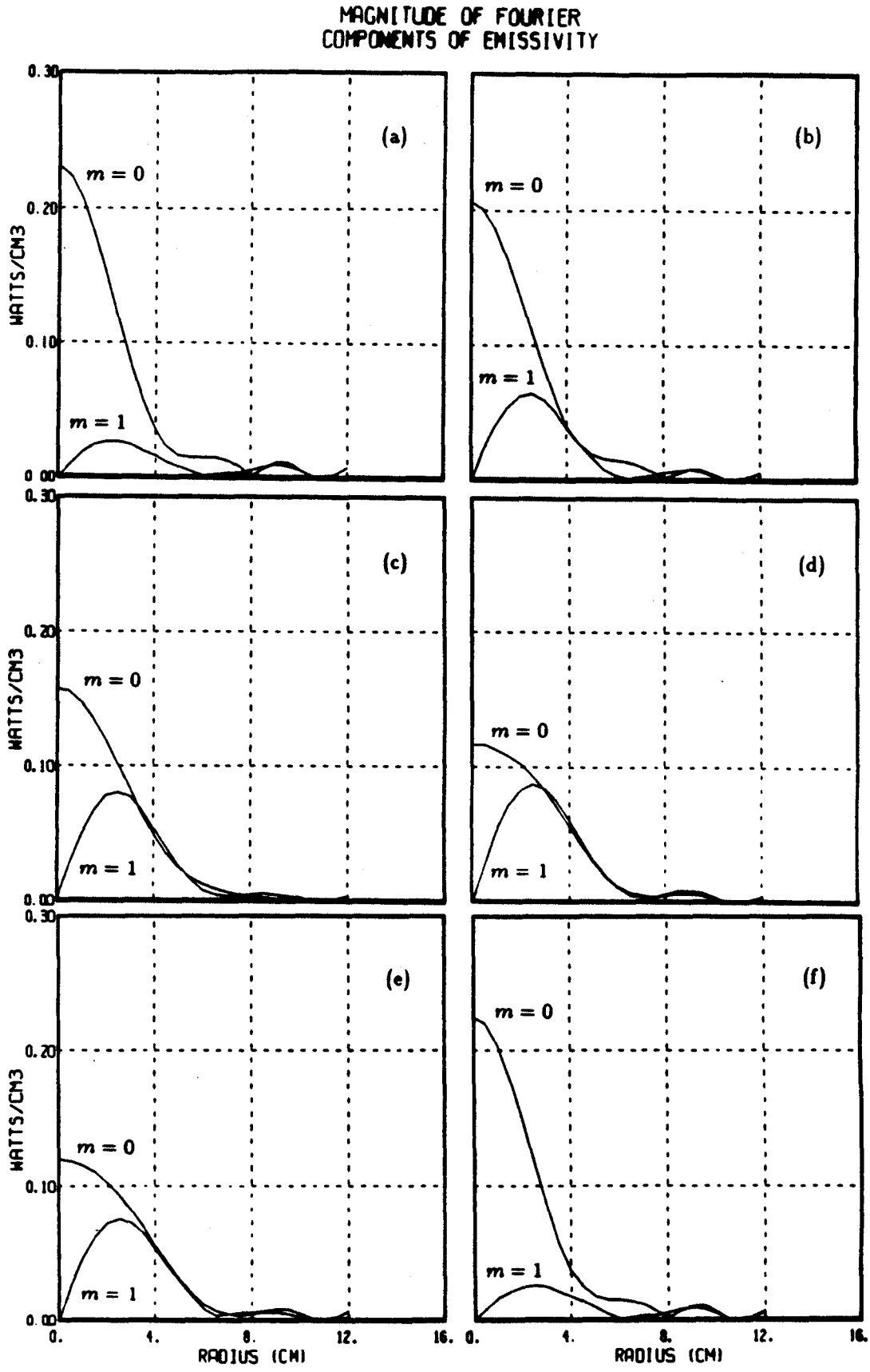

Figure 53 — Reconstruction of non-sawtoothing oscillating emissivity (Fourier components).

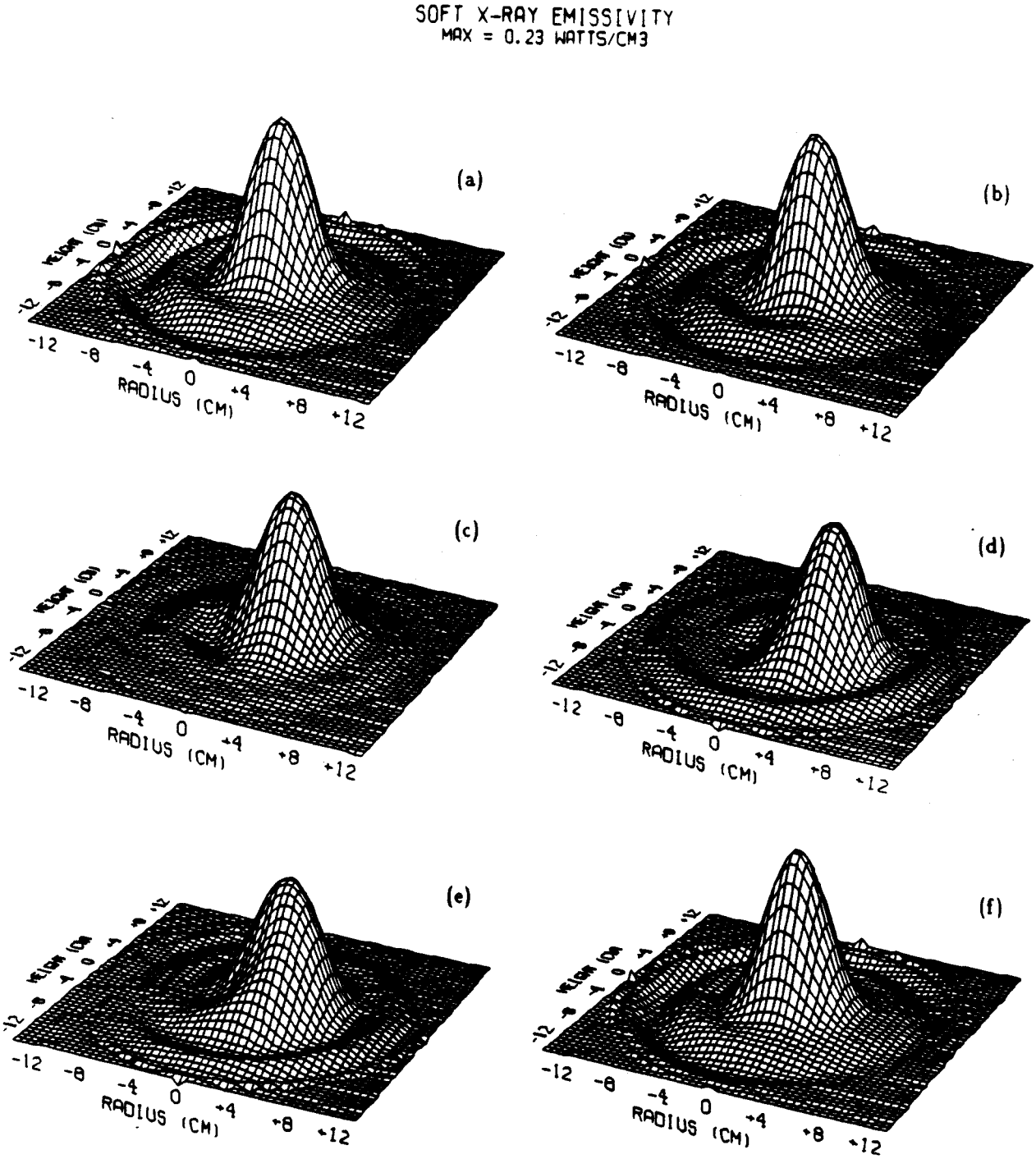

Figure 54 — Reconstruction of non-sawtoothing oscillating emissivity (3-D plots).

representations of the reconstructed emissivities for this cycle. The indentation which takes place in the plasma can be seen in these plots as well (frames (c)-(e)).

Thus, it is obvious that there is a major difference between the type of discharge described above and those which exhibit sawteeth (giant or otherwise). One should keep in mind that it is possible to observe this non-rotating instability because of the fact that the reconstruction algorithm makes no assumption about plasma rotation, position, or symmetry, given the large number of views available. Hence, one is able to reconstruct soft x-ray emissivities which indicate that, in one class of plasma discharges, $m = 1$ oscillations which had previously been ascribed to the rotation of an MHD instability are actually not rotating at all.

There is no immediately apparent explanation for the difference in the discharge analyzed here and the one presented in the previous section. Both involve pellet injection, but in the latter case, no sawtoothing activity occurs after the injection. As can be seen in the raw signal trace in Fig. 50, the post-pellet signal goes to a level which is about a factor of three greater the the pre-pellet level; the soft x-ray emission then breaks into the peculiar oscillations in a rather sudden and spontaneous fashion for no clear reason. In the two types of discharges under consideration, there is no major difference in the pressure gradient. Thus, one would expect that any rotation due to ω_* diamagnetic effects would remain approximately unchanged. It was also suggested in the previous section that a radial electric field may be causing the mode rotation observed in the discharge with giant sawteeth. Substantial differences in E_r, therefore, may lead to the different rotation behavior. This change in electric field would be expected to affect the radial impurity transport (among other things), and, in fact, this is indeed the case. In Alcator C, non-sawtoothing plasmas have soft x-ray fluxes which are larger than those from sawtoothing plasmas, and this feature is presumably due to enhanced impurity radiation. Furthermore, there are indications that the impurity confinement time in Alcator C, which is usually finite, becomes essentially infinite in non-sawtoothing discharges.[41] In other words, impurities may accumulate on axis.

Chapter V

CONCLUSION

V.1 Summary of Present Work

The feasibility of soft x-ray tomography on Alcator C has been demonstrated. An apparatus for performing tomography was successfully designed, built, and implemented on the tokamak. The experiment has yielded reconstructions of the soft x-ray emissivity which have provided good information about plasma equilibrium and behavior during sawtooth oscillations and other instabilities. Unlike many other tomography experiments, the reconstruction method employed here involves *no assumption whatsoever* about plasma rotation, position, or symmetry, and thus allows one to obtain a more realistic representation of the soft x-ray emissivity and the features which influence it. The major findings of this thesis are:

- Reconstructions of emissivities which show the effects of an ordinary sawtooth crash on the plasma equilibrium. The equilibrium reconstructions reveal information about the Shafranov shift and the circularity of the magnetic flux surfaces. The $m = 0$ profile may be slightly hollow after the sawtooth crash.

- Evidence which indicates that a rotating $m = 1$ magnetic island structure is present during the giant sawtooth precursor oscillations that occur after pellet injection. Mode rotation is in the ω_* electron diamagnetic direction.

- Analysis of the emissivity enhancement factor, in the pellet-fueled discharge with giant sawteeth, which serves as an example of how this diagnostic can be used to study the behavior and effects of impurities in the plasma. The results are in qualitative agreement with observations from previous experiments on Alcator C.

- The occurrence, in another type of pellet-fueled discharge, of an $m = 1$ instability (not as yet explained) which is not associated with sawteeth and does not exhibit rotation but rather a compression of the plasma.

Another highlight of this experiment is that a new technology in fusion plasma soft x-ray detection, involving the use of miniature PIN photodiode arrays, has been demonstrated. This development was motivated by the need to have the many detectors required by the reconstruction algorithm placed in a highly confined area. These detectors performed successfully in conjunction with logarithmic amplifiers, which made it possible and convenient to obtain measurements over a wide range of plasma parameters and operating conditions. The small size of the detectors permitted good viewing access to the plasma, even in a machine with very constrained port space such as Alcator C. They are also relatively inexpensive. Both of these facts allowed for many views, which eliminated the need of assumptions such as rotation and led to reconstructions of the emissivity function that have reasonably good resolution.

V.2 Recommendations for Future Work

Given the success of this experiment in terms of being able to obtain good reconstructions with eighty detectors and the questions raised by some of the findings, there is a definite incentive to pursue further work along these lines. The obvious next step in this research would be to increase the number of views by adding arrays of detectors on the side port. Such work is presently underway. This added number of views will improve the coverage of (p, ϕ) space, especially in those regions for which there are no chords in Fig. 12. One should therefore be able to include higher order poloidal harmonics (and possibly radial harmonics as well) in the reconstructions.

As an example of what one could do with more detectors, computer simulations were conducted in which a total of 200 detectors were involved (eight chips on each of the top and bottom ports, and nine chips on the side port, with each chip containing eight detectors as in the real experiment). The design made use of all the space available in each port in order to maximize the number of detectors. The coverage afforded in (p, ϕ) space by such a set-up is shown in Fig. 55. The simulation consists of attempting to reconstruct test emissivities which have $m = 0$, 1, and 2 poloidal mode numbers, using $l = 0, 1, \ldots, 6$ for the radial mode numbers. Fig. 56 shows the result of such a reconstruction; it displays good agreement between the input harmonics and the reconstructed ones. A contour plot of the reconstructed emissivity is given in Fig. 57. Reconstructions going up to $l = 8$ also yielded fairly good results, but they are more sensitive to noise in the data introduced by small random or systematic errors.

It thus appears that one should be able to resolve up to and including the $m = 2$ poloidal component (at least) in the emissivity with the design under consideration here. However, it should be pointed out that, in a typical Alcator C discharge, the $q = 2$ surface is located at $r \approx 10$ cm or beyond, whereas the simulation presented above has the $m = 2$ perturbation peaking at $r = 8$ cm and is thus performed under optimistic circumstances (no noise or errors have been included either). In practice, therefore, it may still be very difficult to resolve the $m = 2$ structure because it is

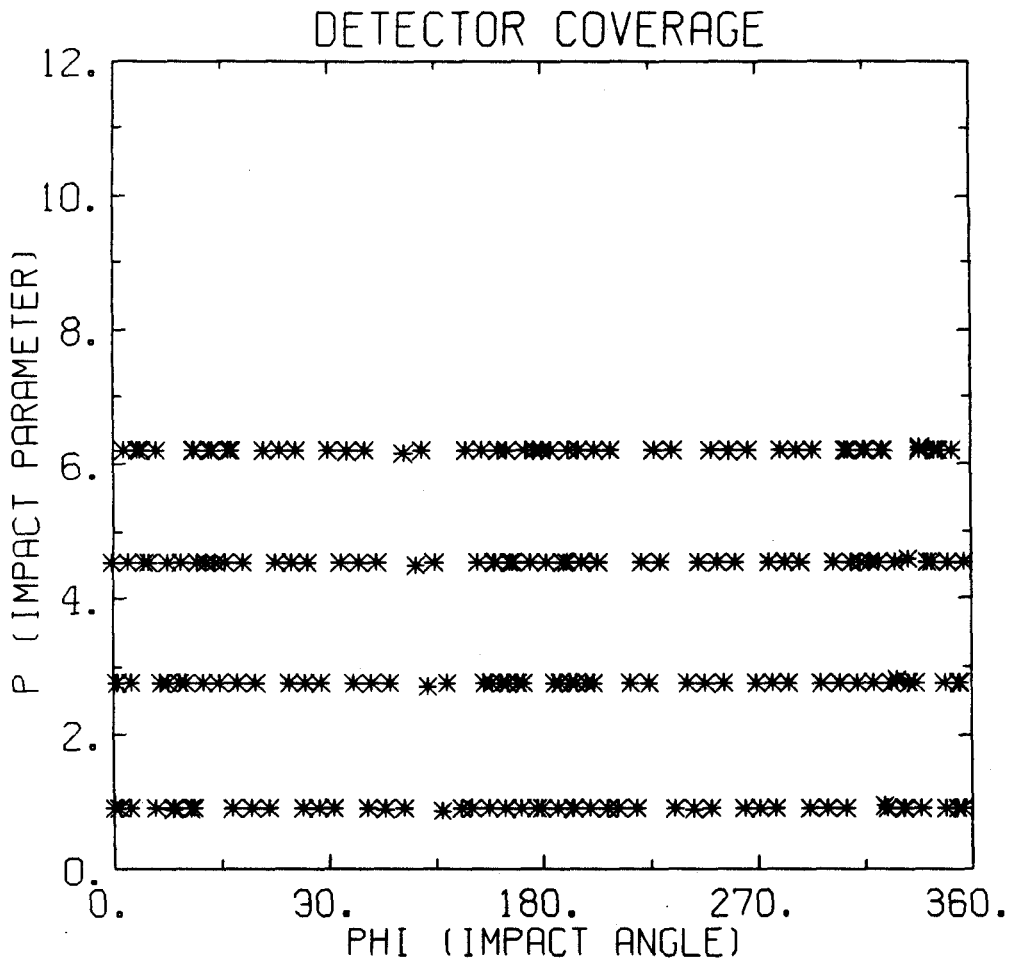

Figure 55 — Detector coverage of (p, ϕ) space for a 200-chord system.

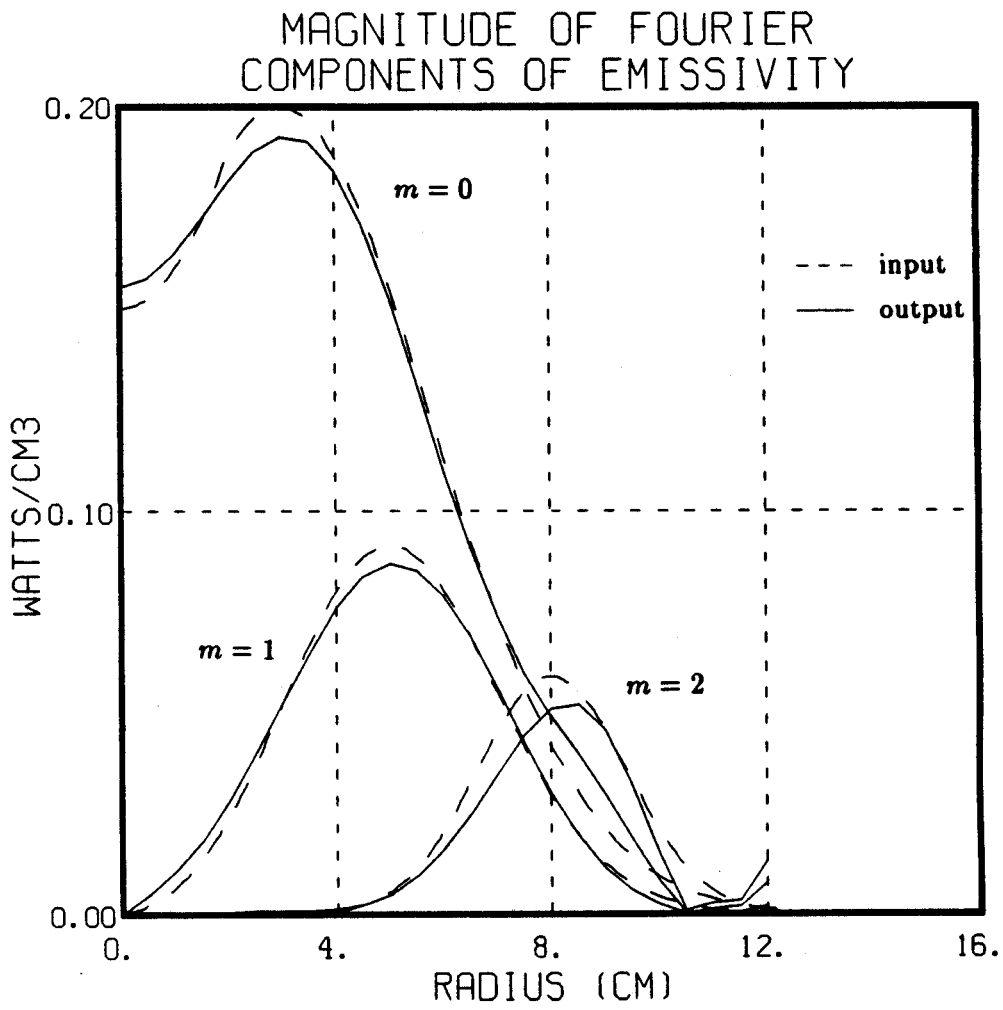

Figure 56 — Test reconstruction with 200 detectors (Fourier components).

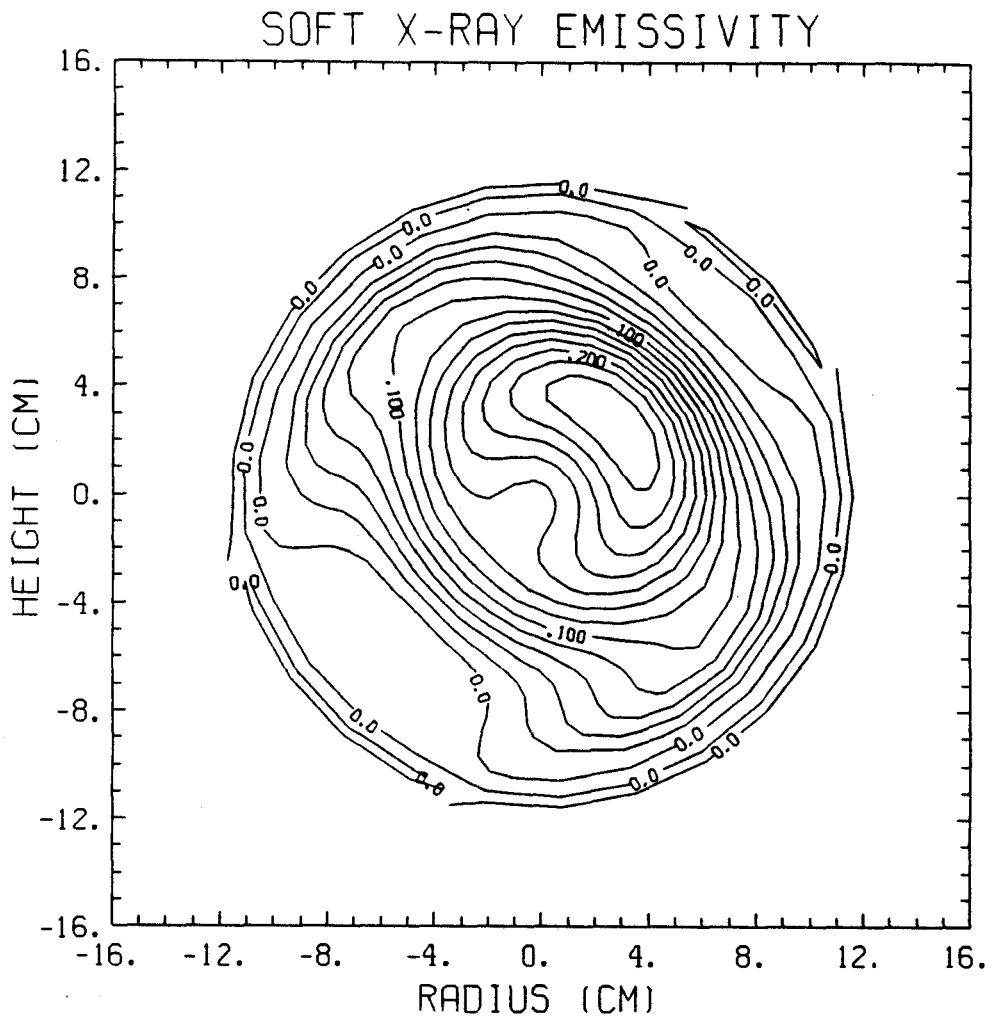

Figure 57 — Test reconstruction with 200 detectors (contour plot). The $m = 1$ island structure is clearly visible, as is the elongation of the contours along the diagonal from the upper left corner to the lower right corner. This elongation is due to the $m = 2$ component present there.

usually located at radii from which there is still no information available in the design in question. Furthermore, one should keep in mind that a 200-detector system is probably too ambitious given the limitations on the amount of data acquisition and storage equipment available. Thus, a more modest 128-detector system is currently being built. It will use four chips with twelve detectors each for the side array, so that the coverage of (p, ϕ) space will be extended to include up to $p = 10$ cm. This feature may facilitate the reconstruction of $m = 2$ poloidal harmonics.

With this array of detectors, one may be able to explain the rather large upward shift observed in the peak of the emissivity discussed in Sec. IV.2. The addition of side views should provide better information about plasma shape and its position in the vertical direction. Furthermore, studies of pellet-fueled discharges with giant sawteeth may provide a more detailed picture of how the $m = 1$ magnetic island evolves and changes shape as it rotates around in the plasma. Finally, the nature of the non-sawtoothing oscillating instability presented in Sec. IV.4 may be understood better by investigating it with the expanded tomography system. In particular, the issue of how impurities are related to the different rotation behaviors can be addressed by using this diagnostic to conduct a more extensive analysis of the enhancement factor than the one presented in Sec. IV.3.; *e.g.*, one could study its dependence on position in the poloidal cross-section and attempt to derive models for the impurity distribution in the plasma. Also, by intentionally injecting minute quantities of impurities into the plasma, one can measure accurately the difference in impurity confinement between rotating and non-rotating discharges, which is another issue raised by the two types of discharges studied in Sec. IV.3 and Sec. IV.4. Work in this direction has already begun.[42]

REFERENCES

1. Tamm, I. E., and Sakharov, A. D., in *Plasma Physics and the Problem of Controlled Thermonuclear Reactions, Vol. 1*, edited by M. A. Leontovich (Pergamon Press, New York, 1961).
2. Chen, F. F., *Introduction to Plasma Physics* (Plenum Press, New York, 1974).
3. Lawson, J. D., *Proc. Phys. Soc.*, Sect. B **70**, 6 (1957).
4. Greenwald, M., *et al.*, *Phys. Rev. Lett.*, **53**, 352 (1984).
5. Luhmann, Jr., N. C., and Peebles, W. A., *Rev. Sci. Instrum.*, **55**, 279 (1984).
6. von Goeler, S., Stodiek, W., and Sauthoff, N., *Phys. Rev. Lett.*, **33**, 1201 (1974).
7. Equipe TFR, *Nucl. Fusion*, **18**, 647 (1978).
8. Petrasso, R., *et al.*, *Rev. Sci. Instrum.*, **51**, 585 (1980).
9. Petrasso, R., *et al.*, *Phys. Rev. Lett.*, **49**, 1826 (1982).
10. Brooks, R. A., and Di Chiro, G., *Phys. Med. Biol.*, **21**, 689 (1976).
11. Sauthoff, N. R., *et al.*, *Nucl. Fusion*, **18**, 1445 (1978).
12. Chase, R. C., *et al.*, *Opt. Eng.*, **20**, 486 (1981).
13. Nagayama, Y., *et al.*, *Jpn. J. Appl. Phys.*, **20**, L779 (1981).
14. Smeulders, P., *Nucl. Fusion*, **23**, 529 (1983).
15. Paré, V. K., *et al.*, *Bull. Am. Phys. Soc.*, **28**, 1254 (1983).
16. Jahns, G., *et al.*, *Bull. Am. Phys. Soc.*, **29**, 1363 (1984).
17. Granetz, R. S., MIT Plasma Fusion Center Report PFC/RR-82-13 (1982).
18. Granetz, R. S., *Bull. Am. Phys. Soc.*, **27**, 1037 (1982).
19. Jackson, J. D., *Classical Electrodynamics* (John Wiley & Sons, Inc., New York, 1975).
20. Glasstone, S., and Lovberg, R. H., *Controlled Thermonuclear Reactions* (D. Van Nostrand Co., Inc., Princeton, 1960).
21. Petrasso, R., MIT Plasma Fusion Center, private communication (1984).
22. Bateman, G., *MHD Instabilities* (The MIT Press, Cambridge, 1978).
23. Freidberg, J. P., *Rev. Mod. Phys.*, **54**, 801 (1982).
24. Jahns, G. L., *et al.*, *Nucl. Fusion*, **18**, 609 (1978).
25. Waddell, B. V., *et al.*, *Phys. Rev. Lett.*, **41**, 1386 (1978).
26. Bracewell, R. N., *Aust. J. Phys.*, **9**, 198 (1956).

27. Gilbert, P. F. C., *J. Theor. Biol.*, **36**, 105 (1972).

28. Hounsfield, G. N., *Br. J. Radiol.*, **46**, 1016 (1973).

29. Strang, G., *Linear Algebra and its Applications* (Academic Press, Inc., New York, 1976).

30. Cormack, A. M., *J. Appl. Phys.*, **9**, 2722 (1963).

31. Cormack, A. M., *J. Appl. Phys.*, **10**, 2908 (1964).

32. Zernicke, F., *Physica*, **1**, 689 (1934).

33. Born, M., and Wolf, E., *Principles of Optics* (Pergamon Press, Ltd., London, 1959).

34. Granetz, R. S., and Camacho, J. F., *Bull. Am. Phys. Soc.*, **28**, 1249 (1983).

35. Camacho, J. F., and Granetz, R. S., *Bull. Am. Phys. Soc.*, **29**, 1224 (1984).

36. Kadomtsev, B. B., *Sov. J. Plasma Phys.*, **1**, 389 (1975).

37. Dubois, M. A., Pecquet, A. L., and Reverdin, C., *Nucl. Fusion*, **23**, 147 (1983).

38. Biskamp, D., *Nucl. Fusion*, **19**, 777 (1979).

39. Granetz, R. S., and Camacho, J. F., MIT Plasma Fusion Center Report PFC/JA-85-5 (1985). To be published in *Nucl. Fusion*.

40. Petrasso, R., *et al.*, *Bull. Am. Phys. Soc.*, **28**, 1249 (1983).

41. Terry, J. L., *et al.*, *Bull. Am. Phys. Soc.*, **28**, 1164 (1983).

42. Terry, J. L., MIT Plasma Fusion Center, private communication (1985).